FATIGUE PERFORMANCE OF MACRO-FIBER PIEZOELECTRIC COMPOSITE ACTUATOR WITH RESPECT TO VARIABLE BEAM GEOMETRY

by

Lyric Michael Rosatti

A thesis submitted in partial fulfillment
of the requirements for the degree

of

Master of Science

in

Mechanical Engineering

MONTANA STATE UNIVERSITY
Bozeman, Montana

August 2012

©COPYRIGHT

by

Lyric Michael Rosatti

2012

All Rights Reserved

APPROVAL

of a thesis submitted by

Lyric Michael Rosatti

This thesis has been read by each member of the thesis committee and has been found to be satisfactory regarding content, English usage, format, citation, bibliographic style, and consistency and is ready for submission to The Graduate School.

Dr. David A. Miller

Approved for the Department of Mechanical and Industrial Engineering

Dr. Christopher H.M. Jenkins

Approved for The Graduate School

Dr. Ronald W. Larsen

STATEMENT OF PERMISSION TO USE

In presenting this thesis in partial fulfillment of the requirements for a master's degree at Montana State University, I agree that the Library shall make it available to borrowers under rules of the Library.

If I have indicated my intention to copyright this thesis by including a copyright notice page, copying is allowable only for scholarly purposes, consistent with "fair use" as prescribed in the U.S. Copyright Law. Requests for permission for extended quotation from or reproduction of this thesis in whole or in parts may be granted only by the copyright holder.

Lyric Michael Rosatti

August 2012

ACKNOWLEDGEMENTS

To begin with, I would like to thank my parents, my sister, and my family, who gave me the confidence and inspiration to dream big. Without them I would not have achieved half of the things I have throughout my academic career. I also owe a great debt of gratitude to Dr. David Miller, my thesis advisor, whose guidance has been a paramount on the journey through graduate school.

Thank you also to my committee for making the time to support my work, and to all of the faculty that have had a hand in my development here at Montana State, especially those whom I have worked for. The learning experiences provided for me have been invaluable. I would also like to thank everyone in the Mechanical and Industrial Engineering Department for their support. To my fellow graduate students, it has been a pleasure to be on the road with you all.

TABLE OF CONTENTS

1. INTRODUCTION 1

Piezoelectricity 1
Historical Development 1
Fiber Composites 5
Reliability of Macro Fiber Composite Piezoelectrics 6

2. TECHNICAL BACKGROUND 9

Piezoelectricity Overview 9
Dipoles in Piezoelectric Materials 9
Directionality and Boundary Conditions in Piezoelectric Materials 12
Governing Equations for the Direct Effect 14
Governing Equations for the Converse Effect 16
General Governing Equation 18
Application of Boundary Conditions 21
Three-Dimensional Constitutive Model 23
Blocked Stress and Free Strain Boundary Conditions 25
Types of Piezoelectric Actuators 28
Monolithic 28
Stack Actuators 32
Developments leading to Piezocomposites 33
Interdigitated Electrodes 33
Piezoceramic Fiber Composites 34
Langley Research Center Macro-Fiber Composite 36
MFC Manufacturing Process 37
MFC Actuation Modeling 44

3. EXPERIMENTAL PROCEDURE 47

Experiment Overview 47
Experimental Specimen 51
Instrumentation and Test Fixture 58
Data Acquisition 58
Keyence Laser Displacement Sensor 58
High Voltage Amplification 59
Setup of Equipment 62

TABLE OF CONTENTS - CONTINUED

Microstructure Imaging 65
Vibration Analysis and Verification 66
Data Aliasing Verification 73

4. EXPERIMENTAL RESULTS AND DISCUSSION 76

Cyclical Actuation Testing 76
System Failure via Electrical Shorting 85
Microscopic Imaging of Specimens 87
Damage Tolerant Design 91
Improving Design 92
Future Work 93

WORKS CITED 94

LIST OF TABLES

Table Page

1. Electromechanical Boundary Conditions 14

2. Results of the analytical solutions to natural frequencies in the transverse direction. The shaded rows are the frequencies that bracket the driving frequency of 3750 Hz. 68

3. Results from ANSYS finite element solutions to the natural frequency of the beams. The shaded rows are the frequencies that bracket the driving frequency of 3750 Hz. The green shaded rows are transverse mode shapes and the yellow shaded rows are torsional modes. Credit: Tyler Tempero..... 69

4. Observed, ANSYS, and analytical resonant frequencies for 1.587mm (1/16”) beam #3. 71

5. Table of Static Displacement, Weinberg Model Displacement, and percent error between the two. 81

6. Ultimate strengths for PZT-5A from Morgan Electro Ceramics (Berlincourt & Krueger, 2003). 89

LIST OF FIGURES

Figure Page

1. Pierre Curie (left) (US Library of Congress) and Jacques Curie (Right) (AIP Emilio Segre Visual Archives). Images under public domain. 2

2. Gabriel Lippmann (http://nobelprize.org/nobel_prizes/physics/laureates/1908/lippmann-bio.html) (Image under Public Domain) 2

3. Paul Langevin (http://www.physik.uni-frankfurt.de/~jr/gif/phys/langevin.jpg) (Image under Public Domain) 4

4. An illustration of a water molecule. The arrow indicates the dipole orientation. (http://en.wikipedia.org/wiki/File:Water-elpot-transparent-3D-balls.png) 9

5. a) Non-uniform orientation of raw material. b) Electric field is applied. c) Residual alignment of dipoles after the electric field is removed (Henslee, 2010). 10

6. Piezoelectric cube indicating coordinate axes in indicial notation. 12

7. Piezoelectric cube indicating coordinate axes in compact notation. 13

8. Example of a property with a boundary condition. (Inman & Cudney, 2000) 14

9. Recreated example from Inman illustrating subscript notation 14

10. A graphical representation of the relation between stress and strain. (Leo) 15

11. A graphical representation of the relation between stress and electric displacement. (Leo, 2007) 16

12. A graphical representation of the relationship between electric field and electric displacement (Leo, 2007). 17

13. A graphical representation of the relationship between electric field and strain. (Leo, 2007) 18

14. A typical frequency response when the frequency is increased to and past resonance. Image: morganelectroceramics.com 20

LIST OF FIGURES – CONTINUED

Figure Page

15. Graphical description of the dissipation factor. 21

16. The effect of boundary conditions on mechanical compliance. 22

17. Boundary conditions representing a.) Blocked Stress and b.) Free Strain 26

18. A graph of the Stress vs. Strain for a 3-3 actuator (Leo, 2007). 27

19. A monolithic piezoelectric actuator commonly used as a buzzer or speaker element. (digikey.com part number 102-1127-ND) 29

20. a.) and b.) show an ideal and not ideal placement of electrodes on a monolithic element. Assume $A_{P,a} > A_{P,b}$ and $t_{P,a} < t_{P,b}$. 30

21. A 3-3 monolithic actuator showing d33 and d31 effects. 31

22. An example of the 3-1 operating mode being utilized to create an extensional device. (Henslee 2009) 31

23. An example of the 3-1 operating mode being utilized to create a bending device, called a bimorph. (Henslee, 2010) 32

24. An example of a piezoelectric stack actuator. The green arrows indicate poling direction. 32

25. A monolithic piezoelectric device with IDE's. The cross section shows how the IDE's generate flux lines affect the dipole orientation. 34

26. A cross section of the Active Fiber Composite (W. K. Wilkie et al., 2000). 35

27. An exploded view of the constituent components that make up the MFC (Henslee, 2010) 36

28. Computer-controlled dicing saw and piezoceramic wafer assembly (W. K. Wilkie et al., 2000). 38

29. Transverse cross section of MFC fibers. 38

30. A top view of an MFC manufactured by Smart Material, Model M-2807-P1. 39

31. Part of the assembly process (W. K. Wilkie et al., 2000). 40

LIST OF FIGURES – CONTINUED

Figure Page

32. In the poling process, the opposite poles of the dipoles and electrodes are attracted to each other. 41

33. Post poling, the electrode polarity is reversed. 42

34. Example of longitudinal and transverse strains in an MFC (W. Wilkie et al., 2002). 43

35. Diagram of the bulk dipole movement during actuation. 43

36. Normalized plots of displacement, force, and work output versus beam-piezoelectric stiffness ratio. 45

37. A similar plot as shown in Figure 36, with points marking the six beam geometries of the thesis experiment. 48

38. Plot of operational lifetime of an MFC at seven different temperatures (Henslee, 2010). 50

39. Images from Henslee's study: a.) Uncycled transverse and longitudinal cross sections. b.) Failed transverse and longitudinal cross sections. 50

40. Aluminum plates used as specimen mounting presses. 53

41. Kapton tape used for thin hinges, masking, and holding the samples in place. 54

42. Removing the Kapton masking from the MFC. 56

43. Using a razor blade to separate the epoxy from the steel substrate. 57

44. Final unimorph composite. 57

45. A National Instruments USB-6221 data acquisition box. 58

46. Keyence LK-G30. The laser head unit (left) connects to the Controller (right). 59

47. Operating range for the Trek PZD700D (Trek, 2011). 60

48. Frequency generator and Trek PZD700D voltage amplifier used to drive the MFC. 61

LIST OF FIGURES – CONTINUED

Figure Page

49. Rear view of the Trek PZD700D. 62

50. An overview of the driving circuit and data logging. 63

51. The experimental test fixture. 64

52. The aluminum support block holds the unimorph and the laser rigidly. 65

53. Nikon SMZ-1500, used to examine the microstructure of the samples. 66

54. 1.587mm (1/16”) Beam, Torsional resonant mode shape at 3.158 kHz. 70

55. 1.587mm (1/16”), Transverse resonant mode shape at 4.552 kHz. 70

56. Examples contrasting appropriately sampled and under sampled signals (Instruments, 2004). 73

57. A typical graph of tip displacement of a single cycle at a data collection rate of 45000 Hz. 74

58. A typical graph of tip displacement of a single cycle at a data collection rate of 82500 Hz. 75

59. A typical bathtub curve represents failure rates over time. Failure rate, λ(t), is the dependent axis. (Nuffer et al., 2007) 77

60. Cycles to failure for all tested beams. 78

61. 12.7mm (1/2”) Sample #1. A micrograph of a crack on the fiber before cyclical testing took place. 79

62. 12.7mm (1/2”) Sample #1. This is a micrograph of the failure site influenced by the fiber crack. This is a prime example of infant mortality. 79

63. Comparison of empirical static displacement of the unimorph versus the Weinberg analytical unimorph model displacement. 80

64. 30 Minute averages of peak displacement data. 82

65. Peak Displacement normalized by Area Moment of Inertia and Elastic Modulus of the beam. 83

LIST OF FIGURES – CONTINUED

Figure Page

66. Beam 3.175mm plotted on a linear scale, with a power curve fit to the data. 84

67. Longitudinal cross-section of an uncycled MFC. 85

68. A heavily cycled MFC with crack propagation. 86

69. Amplitude chart taken directly from the front panel of LabVIEW at the point of failure. 87

70. Unimorph 0.794 mm (1/32") #1 lasted more than 10^9 cycles. The cracking visible in the piezoceramic is significant. 88

71. Failure site on unimorph 1.191mm (3/64") #1. This beam lasted more than 550E+6 cycles, and showed some evidence of crack propagation. 90

72. Failure site on beam 1.191mm (3/64") #3. There is less evidence of cracking in this beam, which had approximately 400E+6 cycles. 91

ABSTRACT

This study is an investigation into the reliability and performance over the lifetime of the piezoelectric fiber composite, macro fiber composite (MFC), with respect to variable beam geometry. MFC's are a class of smart structure utilizing the piezoelectric effect. The MFC is a thin flexible composite system that can be laminated to surfaces or embedded in classic composite structures for actuation and sensing. These piezocomposite structures are rectangular patches made of Lead-Zirconium-Titinate (PZT) piezoceramic fibers, copper-clad polyimide film, and epoxy. MFC's were originally developed at NASA Langley Research Center and are now commercially available from a single manufacturer. In this study, lifespan and performance were characterized by using the MFC as an actuator to impart deflection in a substrate. This structure is referred to as a Unimorph. The beam geometry affects the bending stiffness of the beam, and thus affects the reaction of the MFC. The only free geometrical dimension in this study was beam height. The unimorph was actuated cyclically by an electrical field of 3E+6 volts per micron at a frequency of 3750 Hz. Expected cycles to failure was 10^9 cycles. The test specimens consisted of cantilevered A2 tool steel beams, with six discrete beam heights, and an MFC patch laminated to one surface by a two-part epoxy. Beam tip displacement measurements were taken using a laser displacement sensor as an indication of cyclical performance over time. The beams were cycled until failure or 10^9 cycles for all beam geometries. The results of the experiment indicate a severe drop off in life with an increase of work energy out of the system. This is a function of the ratio of beam stiffness to MFC stiffness. After a break-in period of less than 250E+6 cycles, no significant degradation in operational performance was indicated by the recorded tip displacement despite an immense amount of crack propagation in the piezoceramic fibers. The results of this testing can be used in designing piezoelectric actuators and as a basis for further study of MFC's.

INTRODUCTION

Piezoelectricity

Historical Development

Piezoelectricity is a term that describes a class of crystalline solids that display a two-way coupled behavior, capable of converting between mechanical and electrical energies. However, since the piezoelectric effect is two-way, mechanical to electrical and electrical to mechanical, we use the modifiers direct and converse, respectively, to describe the directionality of the relationship. The direct effect was discovered first and thus took priority in the naming convention when the converse effect was discovered several years later (Leo, 2007).

The initial discovery of piezoelectric materials came in the 1880 by brothers Pierre and Jacques Curie, shown in

Figure 1. The piezoelectric discovery was the result of their study of pyroelectric and crystal symmetry. Parallels in their research led them to believe that certain crystalline structures would possess such an effect. They noted that certain crystals, such as Rochelle salt (sodium potassium tartrate tetrahydrate); quartz; tourmaline; topaz; and cane sugar, produced an electrical output when placed under a mechanical strain (Inman & Cudney, 2000). They successfully were able to demonstrate the mechanical-to-electrical coupling and it was then that they named the effect. The word piezo is Greek in origin, meaning force or press. The combination of piezo and electric

then is taken to mean electricity from pressure, and accurately describes the piezoelectric effect (Leo, 2007).

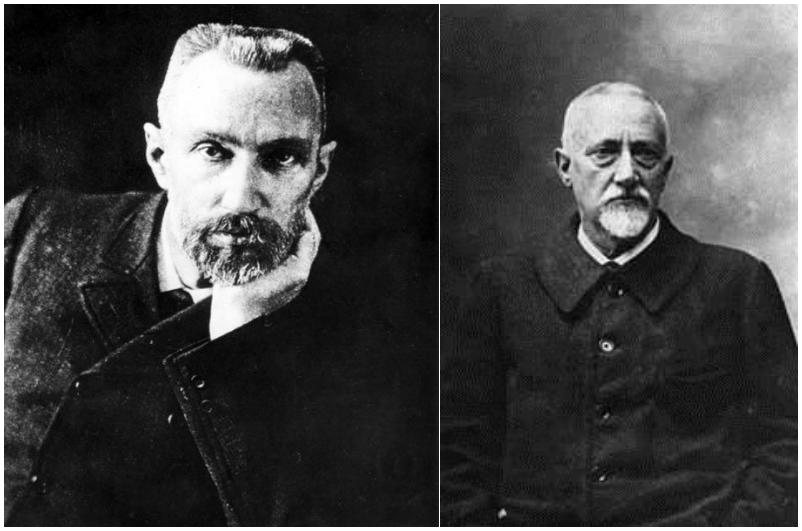

Figure 1: Pierre Curie (left) (US Library of Congress) and
Jacques Curie (Right) (AIP Emilio Segre Visual Archives). Images under public domain.

The Curie brothers failed to predict the converse piezoelectric effect, and in 1881 Gabriel Lippmann, pictured in Figure 2, used fundamental thermodynamic principals to theorize the existence of the reciprocal effect. The Curies then confirmed the converse effect, generating proof of the reversibility Lippmann had hypothesized.

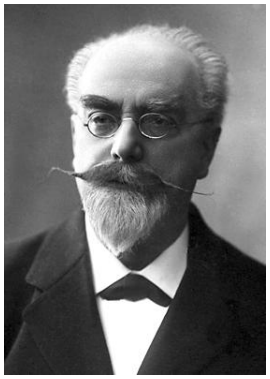

Figure 2: Gabriel Lippmann
(http://nobelprize.org/nobel_prizes/physics/laureates/1908/lippmann-bio.html)
(Image under Public Domain)

The Curie brothers were also able to theorize the crystallographic nature of piezoelectricity; however, they were unfortunate victims of circumstance and were limited by the technology of their time and thus as this point in piezoelectric history, the utility of the effect was severely limited. The amount of electrical charge produced by applied mechanical strain, and mechanical strain produced by applied electrical charge, was too small to have much applicability.

For the next few decades, interest in the piezoelectric effect was mainly academic. The mathematics describing the effect had been developed, but innovation in the field was scarce until the early twentieth century. History has proven conflict to be a constant source of innovation, and as such interest in piezoelectricity gained traction during the onset of World War I. Submarines were one of the most effective weapons platform to come to prominence during the first world war. The effectiveness of the submarine was in large part due to the lack of a system capable of detecting them. In

1916 a prominent French physicist named Paul Langevin, pictured in Figure 3, was a former doctoral student of Pierre Curie, and his colleague Canstantine Chilowski developed and patented a device, called the “Langevin type transducer.” Their device was the first ultrasonic submarine detector and stands today as the basis of SONAR, but it was also the first engineering application of piezoelectric crystals. The device used quartz crystals to actuate a thin metal membrane to generate bursts of ultrasonic sound waves. If a sound wave bounced off an object, the time it took for the echo to return could be used to calculate the distance between submarines using ultrasonic signals and measuring the time it took the signal to return (Inman & Cudney, 2000).

Figure 3: Paul Langevin
(http://www.physik.uni-frankfurt.de/~jr/gif/phys/langevin.jpg)
(Image under Public Domain)

Between World War I and World War II, research to better understand piezoelectric principals, as well as development of applications continued. During this time, a researcher named Walter G. Cady became the vanguard of piezoelectric research (Inman & Cudney, 2000). One of his most important contributions to the field

was the crystal oscillator. He noticed that quartz crystals, exhibited resonance when driven at certain frequencies. By 1921, he designed the first circuit on the idea, which has become a mainstay of modern electronics (Inman & Cudney, 2000).

By the 1930's piezoelectric materials were being used for both electronic and mechanical components in devices such as radios, microphones, and various forms of sensors and actuators. Around this time, researchers came to the realization that the limiting factor was material performance, which led to advances in synthesized piezoelectric materials. The first man-made crystal was developed in the ADP (Ammonium-dihydrogen-phosphate), which debuted in the mid-1930's, and is noted for having the piezoelectric effects of Rochelle salt, with the ruggedness of quartz (Inman & Cudney, 2000). The next notable piezoelectric material was Barium Titinate ($BaTiO_3$) developed in 1940. Barium Titinate was one of the first piezoceramics, which meant that it could be cast into many physical shapes, had a higher operating temperature, and was not-water soluble like Rochelle salt (Inman & Cudney, 2000). Barium Titinate was the principle piezoelectric material used until the development of lead-metaniobate (PMN) and lead-zirconate-titanate (PZT) during the 1950's and 1960's. Today, PZT is still the most widely used piezoelectric material (Leo, 2007).

Recent piezoelectric material research has been driven by the Restriction of Hazardous Substances Directive (RoHS) and the concern of lead-based products being a health hazard. Two piezoceramics have been developed to date that possess promising characteristics, Sodium-Potassium-Niobate and Bismuth-Ferrite. However, the majority

of research done from the 1990's on has not been focused on the development of new materials, but rather how to improve the characteristics of the piezoelectric devices themselves (Inman & Cudney, 2000).

Fiber Composites

The development of piezoelectric fiber composites came about through a desire to improve or negate the core deficiencies seen in monolithic piezoceramics. The major drawbacks to monolithic piezoceramics are brittleness, poor damage tolerance, poor conformability, lack of directional strain actuation, and low strain energy density (W. K. Wilkie et al., 2000).

To diminish the structural drawbacks, a composite approach was used that is similar to a glass fiber reinforced polymer composite. The monolithic composite is cut into thin rectangular fibers and then encapsulated in a protective epoxy matrix. The term protective in this sense is somewhat of a misnomer, as it is not necessarily intended to protect the fibers as much as it is intended to hold the broken pieces together. The composite structure allows for curvatures radii of small as 1.75 inches in the fiber direction and 1.5 inches in the transverse fiber direction (W. K. Wilkie et al., 2000).

To address performance issues, interdigitated electrodes were introduced to produce electrical fields in the plane of the actuator. "In plane electrical fields allow the piezoceramic elements to produce nearly twice the strain actuation, and four times the

strain energy density, of a through-plane poled piezoceramic device (W. K. Wilkie et al., 2000).

Reliability of Macro Fiber Composite Piezoelectrics

It is often the case that when a technology is developed to the point where it can be implemented functionally, that the research of that technology dwindles. In the case of Macro Fiber Composite (MFC) piezoelectrics, developed in 1996 by the National Aeronautics and Space Administration-Langley Research Center, NASA-LaRC, the goal was to improve the already existing monolithic piezoelectrics. This meant that performance statistics were of great interest, and thus many feasibility and design studies have been performed. Today, MFC's are fairly well classified insofar as performance data is readily found. However, reliability statistics, by comparison, are poorly classified. A literature study on the matter does not return a great number of studies.

The work done previously on this project was executed by Isaac Henslee in a co-op with NASA. The work was done partly as a feasibility study to determine how the MFC's performed outside of a nominal temperature envelope, but it was also done to contribute to the existing knowledge base about the reliability of MFC piezoelectrics. The core of the study examined lifetime as a function of temperature. The study showed the MFC's functioned, but had a severely reduced lifetime outside the nominal temperature rating. This is useful information because it helps to describe a proper envelope for future designs using MFC piezoelectrics. However, the usable lifetime of

active structures or materials can depend on many factors other than temperature; such as actuation frequency, stress, and strain levels.

In an effort to build on the knowledge base established by Henslee, the current research is focused on the relationship between useable life and substrate geometry. The working hypothesis is that in an actuation mode, the internal stress and strain experienced by the piezoelectric fibers in the MFC is linked to the geometry of the object the MFC patch is mounted to. This study hopes to show a link between stress, strain, or work energy, and usable life.

The datasheet provided by Smart-Materials Corp gives some indication as to what to expect when using MFC patches in an actuation mode, but the clues are somewhat obfuscated. Under Operational lifetime, two criteria and two life expectancies are provided. The first states that at 1000 Volts peak-to-peak (Vpp) to expect a typical lifetime of greater than “10E+09 cycles.” The second states at 2000 Vpp, 500VDC to expect greater than “10E+07 cycles.” This is less than clear in its meaning, however the working assumption is that the criteria means operating at “-500V to 1500V,” which are the minimum and maximum operational voltage, respectively. The given lifetimes are also in direct conflict with stated lifetimes elsewhere on their website. It is presumed that the meaning is not 10^{10} and 10^{8}, but rather to mean 10^{9} and 10^{7} cycles. The latter numbers correspond with the numbers given elsewhere by Smart-Materials Corp. Regardless of these reported expected lifespans, the problem remains

that these numbers are rough estimates and give very little to an engineer to use as design criteria.

TECHNICAL BACKGROUND

Piezoelectricity Overview

Dipoles in Piezoelectric Materials

Piezoelectrics belong to a class of crystalline solids in which the atoms are arranged in a single atom pattern repeated through the body. The structure of the solid produces a three-dimensional unit cell, which is the smallest repeating segment. The unit cell contains the polarity of the piezoelectric, meaning there is a net separation of positive and negative charge. This is the electric dipole. The existence of electric dipoles within the material accounts for the electromechanical coupling discussed above. One of the most basic examples of an electric dipole is a water molecule. As show in Figure 4, the separation of charges comes from the positive net charge from the two hydrogen atoms, shown in blue, and negative net charge from the oxygen atom, shown in red.

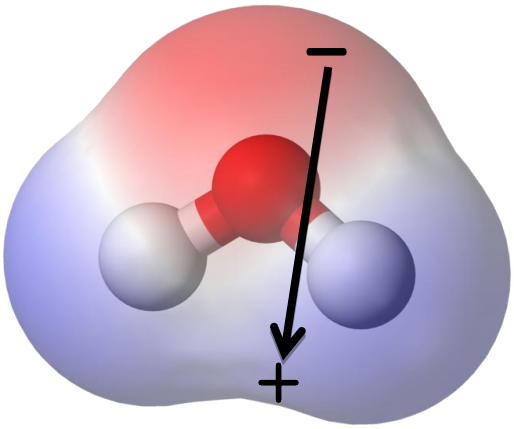

Figure 4: An illustration of a water molecule. The arrow indicates the dipole orientation. (http://en.wikipedia.org/wiki/File:Water-elpot-transparent-3D-balls.png)

If a dipole is subjected to an electric field, a torque is generated. This torque will try to orient the dipole in the direction of the electric field. This is how mechanical displacement is generated by a piezoelectric. The converse is also true. When the piezoelectric is displaced mechanically, the field shown in Figure 4 will change direction and change the charge in the electrodes.

The most common piezoelectric materials are Lead-Zirconium-Titinate, known as PZT; Barium Titinate; and Sodium-Potassium Niobate. These are also sometimes referred to as Piezoceramics (Inman & Cudney, 2000). When piezoelectric materials are first made, they are considered "raw," meaning the material is isotropic and the dipoles are typically not oriented very well, as shown in part a of Figure 5. If there is a high amount of disorder of the dipoles, there is not enough net dipole movement in a single direction to cause bulk deformation of the structure or net change in electric field. The piezoelectric material must be poled to orient the dipoles uniformly.

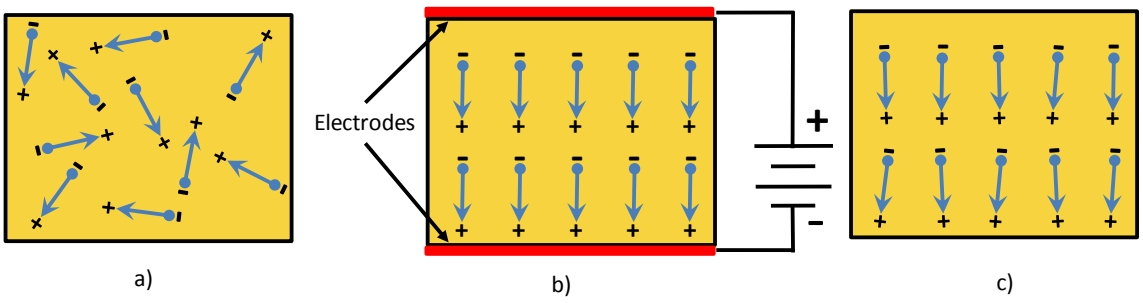

Figure 5: a) Non-uniform orientation of raw material. b) Electric field is applied. c) Residual alignment of dipoles after the electric field is removed (Henslee, 2010).

Poling is the process by which piezoelectric materials are given a poling direction. In general, the term poling direction refers to a local orthogonal coordinate system. During poling, the material is heated above the Curie temperature and then placed in a strong electric field, typically 2000 Volts per millimeter of separation between the plates generating the field. Part b of Figure 5 shows the field being generated and aligning the dipoles. The Curie temperature is the temperature at which the material loses its spontaneous polarization. In piezoelectrics, the material is tetragonal in structure below T_C. Above T_C the material is cubic and the central cation is displaced from the center of the unit cell, thus no net dipole movement. Above T_C the dipoles can move freely in the applied field direction. Smart-Material's MFC's are primarily made of PZT-5A, which has a Curie temperature of 360°C (Smart-Material, 2011). Part c of Figure 5 shows the residual orientation of the dipoles after the electric field is removed. The material retains a portion of the polarization directionality after the field is removed, and thus the material becomes piezoelectric. During polarization, the dimensions of the ceramic typically change due to changes in the crystalline structure (Inman & Cudney, 2000). This poling method is used for monolithic piezoelectrics. The poling method of MFC's will be discussed in the appropriate section.

Exceeding a threshold voltage during operation of a piezoelectric can result in degradation or elimination of the dielectric and piezoelectric properties of the material, especially in the depoling direction. The depoling direction is simply the negative 3 direction. If the field is strong enough, the piezoelectric can be repoled in the depoling

direction. The maximum depoling field a piezoceramic can withstand without sustaining permanent degradation is called the coercive field (Inman & Cudney, 2000). The coercive field is dependent on material and poling processes.

Directionality and Boundary Conditions in Piezoelectric Materials

Piezoelectric material directions are the same as would be found in any other arbitrary cube of material. Figure 6 shows a typical orthogonal rectangular Cartesian coordinate system for a piezoelectric cube. It is convenient to use compact notation for normal and shear stresses. In compact notation 1, 2, and 3 indicate the principal axes and 4, 5, and 6 indicate the shear around 1, 2, and 3 respectively.

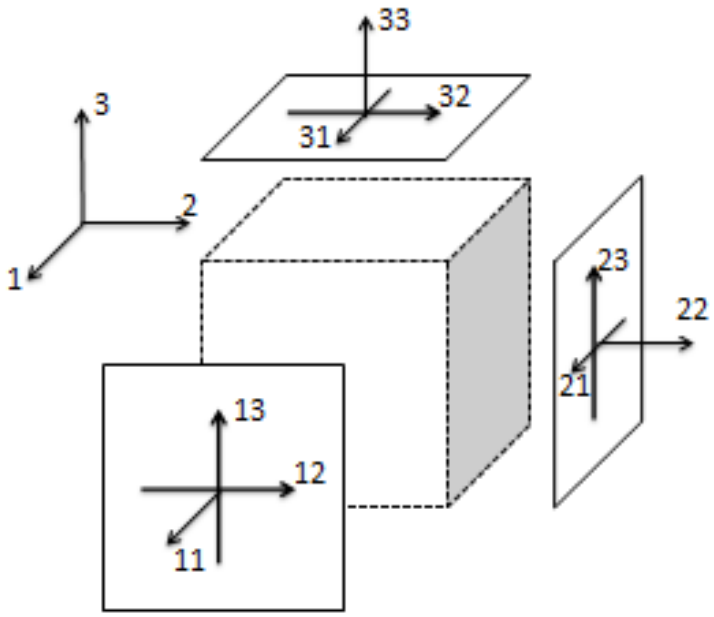

Figure 6: Piezoelectric cube indicating coordinate axes in indicial notation.

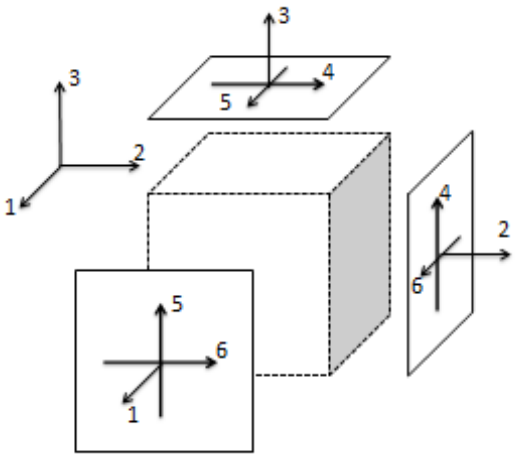

Figure 7: Piezoelectric cube indicating coordinate axes in compact notation.

Typical notation sets the 3 axis as the poling vector, which is sometimes referred to as the polar axis. The 1 and 2 axes are mutually orthogonal to the polling direction and the material overall become transversely isotropic. Because polar symmetry exists about the 3 axis, it is standard to omit reference to the 2 direction. It is assumed that the 1 direction implies the same relationship for the 2 direction (Inman & Cudney, 2000).

Directionality and boundary conditions are critical in defining material properties in piezoelectric devices. A combination of subscripts and superscripts are used to indicate directionality and boundary conditions, relatively. Figure 8 and Figure 9 describe the general configuration of what superscripts subscripts mean. The electromechanical boundary conditions indicated by superscripts are indicated in Table 1. The implications of these boundary conditions will be addressed where relevant to material properties below.

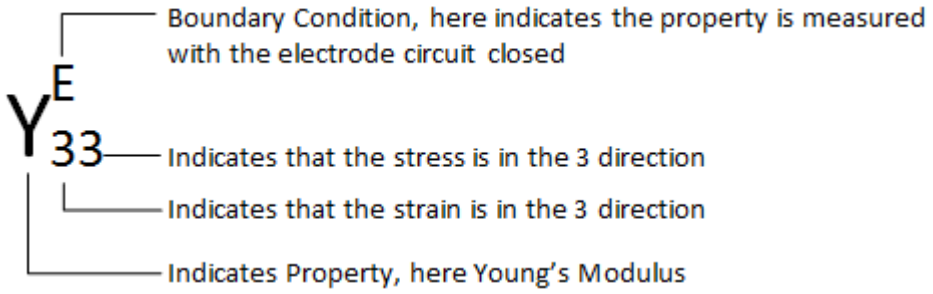

Figure 8: Example of a property with a boundary condition. (Inman & Cudney, 2000)

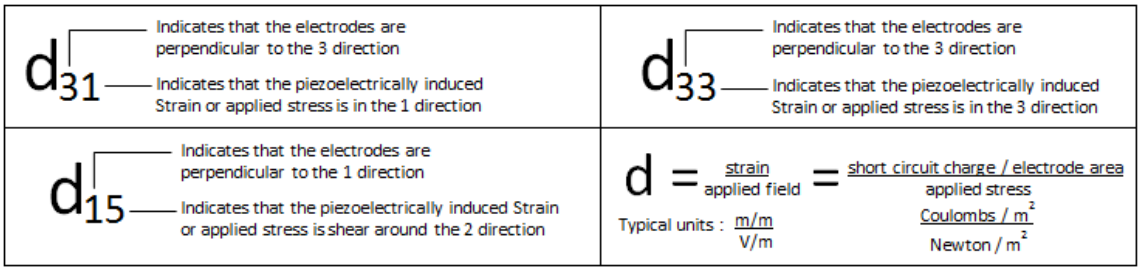

Figure 9: Recreated example from Inman illustrating subscript notation.

Table 1: Electromechanical Boundary Conditions

Electrical Boundary Conditions	Mechanical Boundary Conditions
D = constant electrical displacement (open circuit)	**T** = constant stress (mechanically free)
E = constant field (short circuit)	**S** = constant strain (mechanically constrained)

Governing Equations for the Direct Effect

The relation between stress, defined as σ_{mech}, and strain, defined as ε_{strain}, is well established, shown by Equation [1] and Figure 10. Stress and strain are proportional with respect to material's elastic modulus, defined as "Y," or its reciprocal, mechanical compliance, defined as "s."

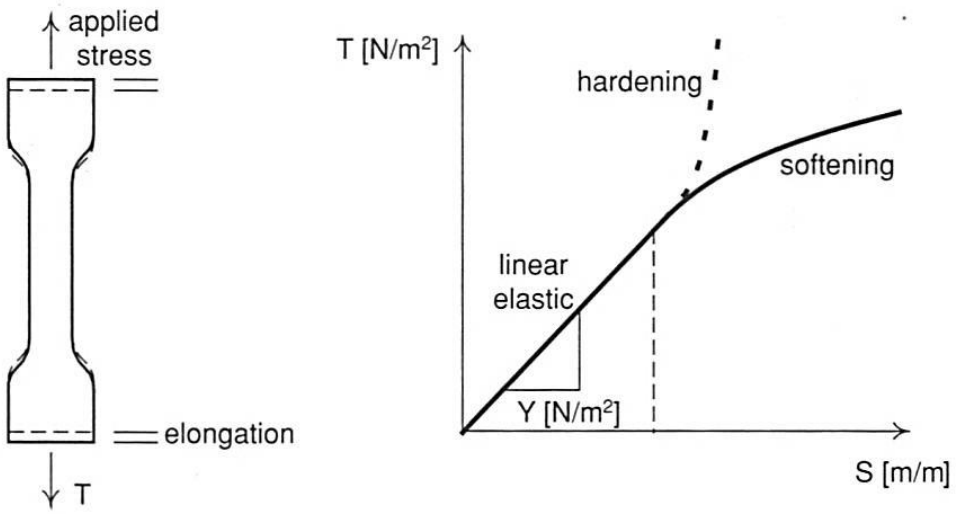

Figure 10: A graphical representation of the relation between stress and strain. (Leo)

In the study of piezoelectricity, the Direct Effect refers to an applied mechanical load producing a change electrical field, caused by the motion of electric dipoles in the material altering the electric field and inducing a charge flow. The charge flow divided by the area of the electrodes is the electric displacement, assigned the symbol "D" and has units of Coulomb per square meter. Figure 11 shows that a higher applied mechanical stress, results in a positive the movement of the dipoles, and subsequently a higher electric displacement produced. Similar to elastic modulus, there is a piezoelectric strain coefficient, assigned the symbol "d" and is commonly reported as meters per volt or Coulomb per Newton. This set of coefficients defines a linear region of the electric displacement to mechanical strain.

$$\varepsilon_{\text{strain}} = Y^{-1} * \sigma_{mech} = s * \sigma_{mech} \quad [1]$$

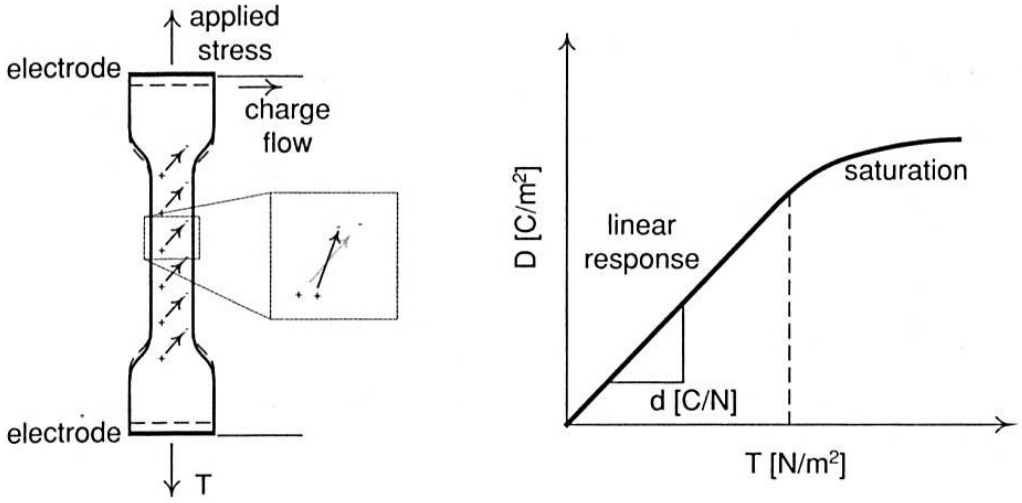

Figure 11: A graphical representation of the relation between stress and electric displacement. (Leo, 2007)

The nonlinear region of the plot in Figure 11 occurs due to the saturation of dipole movement. In the linear region, the equation for the relationship between "D" and "σ_{mech}" is defined as,

$$D\left(\frac{C}{m^2}\right) = d\left(\frac{C}{N}\right) * \sigma_{mech}\left(\frac{N}{m^2}\right) \quad [2]$$

Governing Equations for the Converse Effect

The Converse Effect is then the mechanical strain that results from an applied electric field. Assuming the material to be a perfect insulator, an applied voltage, defined as "V," produces Electric Field, defined as "E," which is equal to the voltage divided by the distance between the electrodes. Electric field has units of Volts per meter. Figure 12 shows that a higher applied electric field, results in a positive the movement of the dipoles, and subsequently a higher electric displacement produced.

The dielectric permittivity, $\varepsilon_{dielectric}$, has units of Ferad per meter and defines the linear region between electric field and electric displacement. This set of coefficients defines a linear region of the electric displacement to mechanical strain.

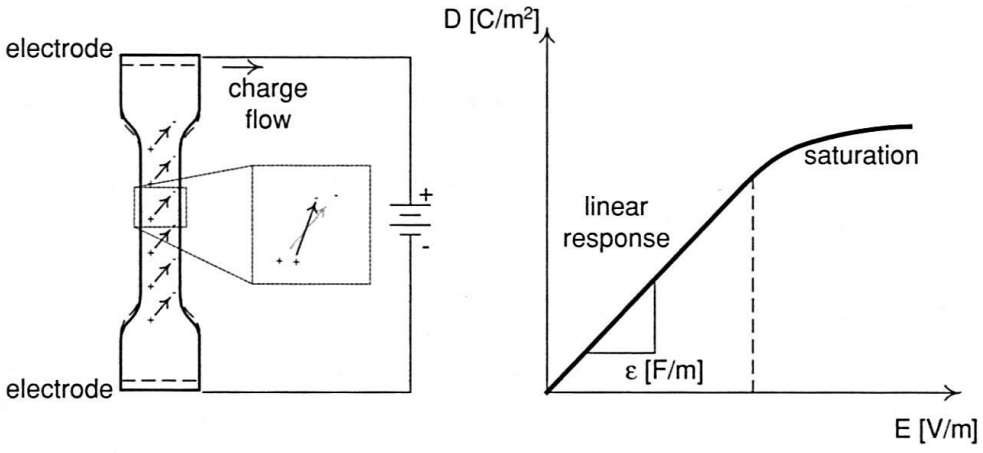

Figure 12: A graphical representation of the relationship between electric field and electric displacement (Leo, 2007).

As with the Direct Effect, the nonlinear region of the plot in Figure 12 occurs due to the saturation of dipole movement. In the linear region the relationship between "E" and "D" is defined as,

$$D\left(\frac{C}{m^2}\right) = \varepsilon_{dielectric}\left(\frac{F}{m}\right) * E\left(\frac{V}{m}\right) \quad [3]$$

A relationship also exists between strain and electric field. Here, as shown in Figure 13, the piezoelectric strain coefficient linearly relates the applied electric field and the resulting mechanical strain. As above, the nonlinear region is due to saturation limit of dipole movement.

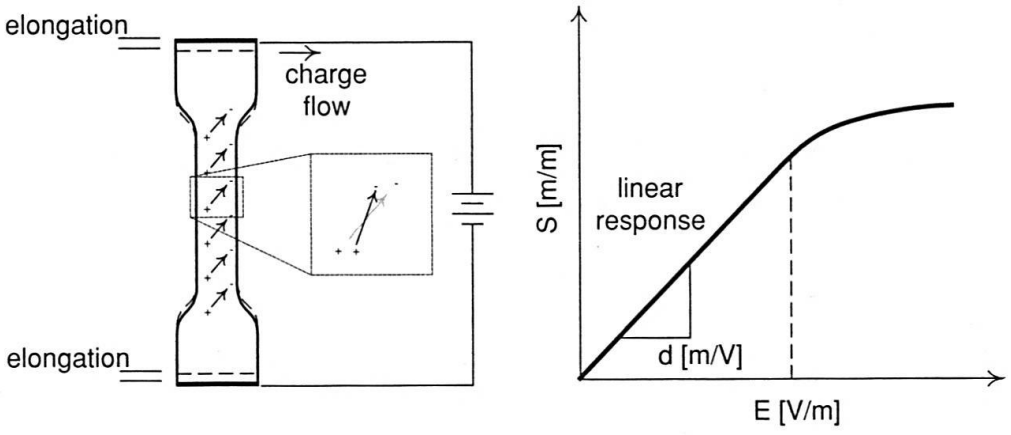

Figure 13: A graphical representation of the relationship between electric field and strain. (Leo, 2007)

$$\varepsilon_{strain}\left(\frac{m}{m}\right) = d\left(\frac{C}{N}\right) * E\left(\frac{V}{m}\right) \quad [4]$$

General Governing Equation

These four equations make up the four corners of the governing equation for piezoelectric devices. As such, the direct and converse piezoelectric effects as a set of linear equations is given by,

$$\begin{Bmatrix} \varepsilon_{strain} \\ D \end{Bmatrix} = \begin{bmatrix} s & d \\ d & \varepsilon_{dielectric} \end{bmatrix} \begin{Bmatrix} \sigma_{mech} \\ E \end{Bmatrix} \quad [5]$$

The top and bottom equations represent the converse effect and the bottom equation, respectively. The on-diagonal terms, compliance and dielectric permittivity, describe the constitutive relationships of a purely mechanical and purely dielectric material, relatively. The electro-mechanical coupling is handled in the off-diagonal by piezoelectric strain constant d. The larger d is, the more strain produced for an applied

electrical field, or more electrical displacement for an applied stress (Leo, 2007). It is important to note that in the most general form, each variable in equation [5] is a tensor representing multiple directions. Furthermore, equation [5] can also be expressed at Equation with stress and electric field as the dependent variables,

$$\begin{Bmatrix} \sigma_{mech} \\ E \end{Bmatrix} = \frac{1}{s * \varepsilon_{dielectric} - d^2} \begin{bmatrix} \varepsilon_{dielectric} & -d \\ -d & s \end{bmatrix} \begin{Bmatrix} \varepsilon_{strain} \\ D \end{Bmatrix} \quad [6]$$

There are numerous other constants that describe the effectiveness of piezoelectric devices. A derived unit that is often useful for piezoelectric modeling is the piezoelectric coupling coefficient, k, which is unitless. Furthermore, k^2 ranges between 0 to 1. This coupling factor describes the fraction of energy that is converted between mechanical and electrical energies (Leo, 2007). Since a piezoelectric is an electromechanical device, this factor can be described by the example of the energy of an applied pressure on the piezoelectric element. Assuming an ideal system, when the pressure is applied a fraction of the energy will be seen in the electrodes as an electrical charge, while the rest of the energy is stored in the material as mechanical energy. In this example, k^2 describes the fraction of the applied pressure that is seen in the electrodes as electric charge. When the applied pressure is released, the system returns to its original state (Inman & Cudney, 2000). A higher k^2 is more desirable. The equation that defines k is

$$k = \frac{d}{\sqrt{s * \varepsilon_{dielectric}}} \quad [7]$$

There are also terms that describe the dynamic efficiency of a piezoelectric system. The primary components of dynamic efficiency are the Mechanical Quality Factor and the Dissipation Factor. Typically, losses due to the Dissipation Factor are more severe. The Mechanical Quality Factor, Q_m, describes the ratio of energy supplied to the energy dissipated per cycle. This is related to the bandwidth of the amplitude of the frequency response. Q_m can be approximated using Figure 14, where Amax is the amplitude at the resonance frequency, f_r. Frequencies f_1 and f_2 are the frequencies that describe the bandwidth, or when the amplitude of the piezoelectric is $Amax/\sqrt{2}$.

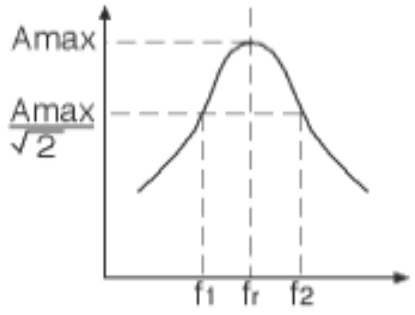

Figure 14: A typical frequency response when the frequency is increased to and past resonance. Image: morganelectroceramics.com

The mechanical quality factor is then approximated as,

$$Q_m = \frac{f_r}{f_2 - f_1} \quad [8]$$

The dissipation factor of a piezoelectric, typically given as $\tan\delta$ or $1/Q_E$, describes the dielectric losses of the system. In an actively cycled piezoelectric subject to harmonic electrical excitation, the electrical charge is complex and thus has both

imaginary and real components. The dissipation factor describes the ratio of resistance to the reactance. Graphically this is shown in Figure 15. A low dissipation factor is more desirable because there is less dielectric loss to the imaginary part (Inman & Cudney, 2000).

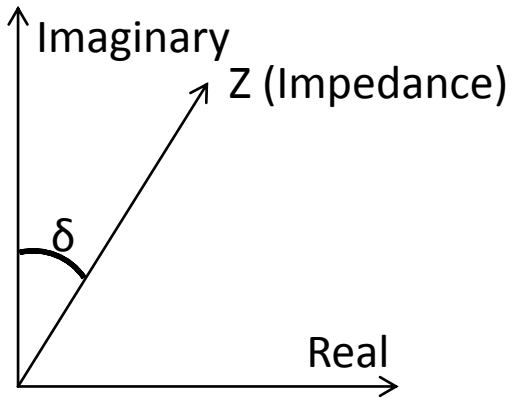

Figure 15: Graphical description of the dissipation factor.

Application of Boundary Conditions

The application of boundary conditions to the governing equation demonstrates how some material properties are affected by boundary conditions. Starting with the electrical boundary conditions, when the circuit is closed there is zero field across the electrodes and thus the electric field E = 0. In this scenario, equation [5] reduces to equations [1] and [2]. Using equation [6], let the electrical boundary be an open circuit. At this boundary condition no charge can flow from the electrodes, so electric displacement D = 0. Equation [6] becomes,

$$\sigma_{mech} = \frac{1}{s * (1 - k^2)} * \varepsilon_{\text{strain}} \quad [9]$$

$$E = \frac{k^2}{d * (1 - k^2)} * \varepsilon_{\text{strain}} \quad [10]$$

To compare equation [9] with equation [1], solve for strain,

$$\varepsilon_{\text{strain}} = s * (1 - k^2) * \sigma_{\text{mech}} \quad [11]$$

Consider that if both boundary conditions had an equal amount of strain, then they could be written as the combination of both boundary conditions,

$$\varepsilon_{\text{strain}} = \begin{cases} s^E * \sigma_{\text{mech}} & short\ circuit \\ s^E * (1 - k^2) * \sigma_{\text{mech}} & open\ circuit \end{cases} \quad [12]$$

With equation [12] written as such, the relationship between the open and short circuit conditions can be written,

$$s^D = s^E * (1 - k^2) \quad [13]$$

Shown graphically,

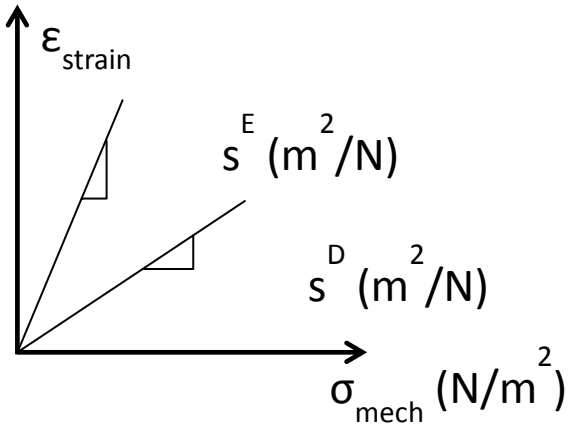

Figure 16: The effect of boundary conditions on mechanical compliance.

A similar relationship with a similar derivation exists between the dielectric permittivity and the mechanical boundary conditions, zero strain and zero stress, and is defined as,

$$\varepsilon^{S}_{dielectric} = \varepsilon^{T}_{dielectric} * (1 - k^2) \quad [14]$$

Three-Dimensional Constitutive Model

Using the index notation as show in Figure 6, the most general tensor notation for a piezoelectric material requires 81 mechanical compliance terms to fully describe the relationship between stress and strain, 27 piezoelectric strain coefficient terms to describe the relationship between strain and electric field or stress and electric displacement, and 9 dielectric permittivity terms to fully describe the relationship between electric field and electric displacement (Leo). The use of compact notation, mentioned above and shown in Figure 7, is based on the polar symmetry of the material. The switch to compact notation affects the mechanical compliance and the piezoelectric strain coefficient tensors, reducing them to 36 and 18 terms respectively. The expanded form of the constitutive equations, in compact notation is described as,

$$\begin{pmatrix} \varepsilon_1 \\ \varepsilon_2 \\ \varepsilon_3 \\ \varepsilon_4 \\ \varepsilon_5 \\ \varepsilon_6 \end{pmatrix} = \begin{pmatrix} s_{11} & s_{12} & s_{13} & s_{14} & s_{15} & s_{16} \\ s_{21} & s_{22} & s_{23} & s_{24} & s_{25} & s_{26} \\ s_{31} & s_{32} & s_{33} & s_{34} & s_{35} & s_{36} \\ s_{41} & s_{42} & s_{43} & s_{44} & s_{45} & s_{46} \\ s_{51} & s_{52} & s_{53} & s_{54} & s_{55} & s_{56} \\ s_{61} & s_{62} & s_{63} & s_{64} & s_{65} & s_{66} \end{pmatrix} \cdot \begin{pmatrix} \sigma_1 \\ \sigma_2 \\ \sigma_3 \\ \sigma_4 \\ \sigma_5 \\ \sigma_6 \end{pmatrix} + \begin{pmatrix} d_{11} & d_{12} & d_{13} \\ d_{21} & d_{22} & d_{23} \\ d_{31} & d_{32} & d_{33} \\ d_{41} & d_{42} & d_{43} \\ d_{51} & d_{52} & d_{53} \\ d_{61} & d_{62} & d_{63} \end{pmatrix} \cdot \begin{pmatrix} E_1 \\ E_2 \\ E_3 \end{pmatrix} \quad [15]$$

$$\begin{pmatrix} D_1 \\ D_2 \\ D_3 \end{pmatrix} = \begin{pmatrix} d_{11} & d_{12} & d_{13} & d_{14} & d_{15} & d_{16} \\ d_{21} & d_{22} & d_{23} & d_{24} & d_{25} & d_{26} \\ d_{31} & d_{32} & d_{33} & d_{34} & d_{35} & d_{36} \end{pmatrix} \cdot \begin{pmatrix} \sigma_1 \\ \sigma_2 \\ \sigma_3 \\ \sigma_4 \\ \sigma_5 \\ \sigma_6 \end{pmatrix} + \begin{pmatrix} \varepsilon_di_{11} & \varepsilon_di_{12} & \varepsilon_di_{13} \\ \varepsilon_di_{21} & \varepsilon_di_{22} & \varepsilon_di_{23} \\ \varepsilon_di_{31} & \varepsilon_di_{32} & \varepsilon_di_{33} \end{pmatrix} \cdot \begin{pmatrix} E_1 \\ E_2 \\ E_3 \end{pmatrix} \quad [16]$$

The reduction of terms does not end at compact notation. As described above, most piezoelectric materials are transversely isotropic. This reduces the mechanical compliance matrix to a variation of a well-known result,

$$s^E = \begin{bmatrix} \frac{1}{(Y^E)_1} & \frac{-\upsilon_{12}}{(Y^E)_1} & \frac{-\upsilon_{13}}{(Y^E)_1} & 0 & 0 & 0 \\ \frac{-\upsilon_{12}}{(Y^E)_1} & \frac{1}{(Y^E)_1} & \frac{-\upsilon_{23}}{(Y^E)_1} & 0 & 0 & 0 \\ \frac{-\upsilon_{31}}{(Y^E)_3} & \frac{-\upsilon_{32}}{(Y^E)_3} & \frac{1}{(Y^E)_3} & 0 & 0 & 0 \\ 0 & 0 & 0 & \frac{1}{(G^E)_{23}} & 0 & 0 \\ 0 & 0 & 0 & 0 & \frac{1}{(G^E)_{13}} & 0 \\ 0 & 0 & 0 & 0 & 0 & \frac{1}{(G^E)_{12}} \end{bmatrix} \quad [17]$$

The variation comes from the symmetry between the 1 and 2 directions, which in this case makes $Y^E_1 = Y^E_2$. Similarly the piezoelectric strain coefficient matrix and the dielectric permittivity matrix reduce to become (Leo, 2007),

$$\varepsilon = \begin{pmatrix} \varepsilon_di_{11} & 0 & 0 \\ 0 & \varepsilon_di_{22} & 0 \\ 0 & 0 & \varepsilon_di_{33} \end{pmatrix} \quad [18]$$

$$d = \begin{pmatrix} 0 & 0 & 0 & 0 & d_{15} & 0 \\ 0 & 0 & 0 & d_{15} & 0 & 0 \\ d_{31} & d_{31} & d_{33} & 0 & 0 & 0 \end{pmatrix} \quad [19]$$

After all of the reduction, the three dimensional governing equation becomes much more manageable with only three dielectric permittivities, three piezoelectric strain coefficients, and six independent mechanical compliance terms. The remaining terms are those commonly reported on manufacturer data sheets.

Blocked Stress and Free Strain Boundary Conditions

In the scope of this thesis work, the focus is on the converse effect, a resultant mechanical strain from an applied electrical field. The two mechanical boundary conditions are referred to as blocked stress and free strain. Some manufacturers, such as the manufacturer of the piezoelectric used in this thesis, use blocked force and free displacement, or a combination of the two. In piezoelectric devices, directionality is generated by the placement of electrodes in various configurations to utilize certain material or piezoelectric effects, these configurations are termed operating modes. The primary two operating modes for piezoelectric actuation are 3-3 and 1-3. As indicated above, directionality is a driving factor to the material properties used in the governing equation set.

Consider a piezoelectric with a 3-3 operating mode. The first number indicates that the electrodes are perpendicular to the 3 direction and the second number indicates that the induced strain or applied stress is in the 3 direction. For a device acting as an actuator in a 3-3 operating mode, the equation of interest is,

$$\varepsilon_{\text{strain},3} = \frac{1}{Y_3^E} * \sigma_{\text{mech},3} + d_{33} * E_3 \qquad [20]$$

The mechanical boundary conditions, as shown in

Figure 17, are then capable of defining the range between which the piezoelectric actuator will operate.

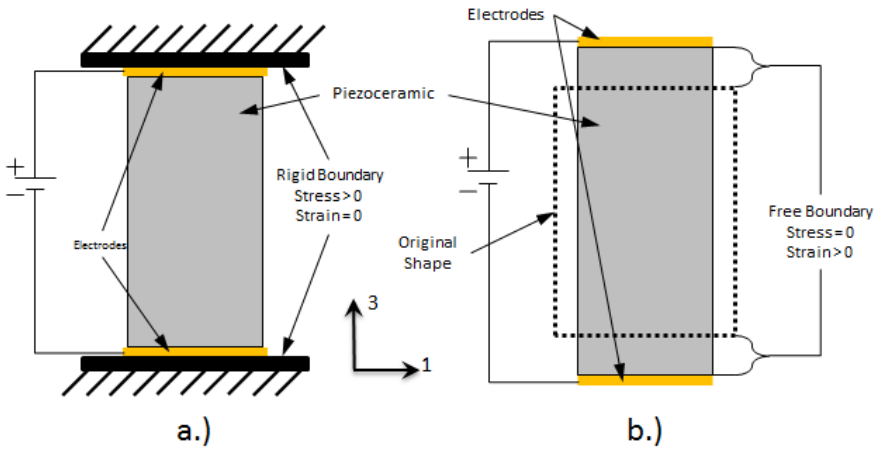

Figure 17: Boundary conditions representing a.) Blocked Stress and b.) Free Strain

Figure 17, set $\varepsilon_{\text{strain},3} = 0$. Applying this condition to equation [20] yields,

$$\sigma_{\text{mech},3} = -Y_3^E * d_{33} * E_3 \qquad [21]$$

Then Analyze the free strain condition shown in part b of Figure 17, where $\sigma_{\text{mech},3} = 0$. Applying this condition to equation [20] results in,

$$\varepsilon_{\text{strain},3} = d_{33} * E_3 \quad [22]$$

Both equations are functions of the piezoelectric strain coefficient, which is essentially a constant, and electric field, which is easily varied. If equation [21] and [22] are plotted on a stress strain curve for a single value of electric field, they will describe the y-intercept and the x-intercept, respectively. This plot is shown in Figure 18. The equation, formatted as a slope-intercept equation, that describes this relationship is,

$$\sigma_{\text{mech},3} = Y_3^E * \varepsilon_{\text{strain},3} - Y_3^E * d_{33} * E_3 \quad [23]$$

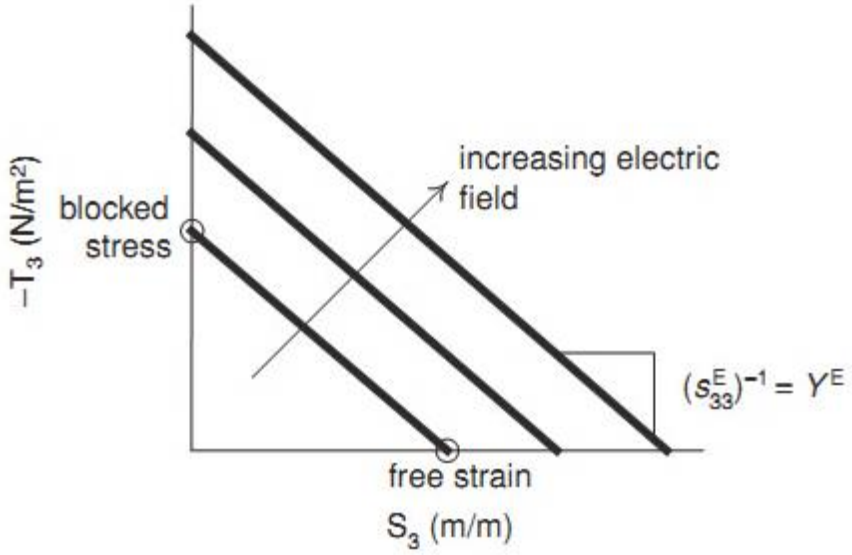

Figure 18: A graph of the Stress vs. Strain for a 3-3 actuator (Leo, 2007).

In Figure 18, note that the three diagonal lines represent the stress-strain relationship for three discrete electric fields. Also, note that the practical use of a piezoelectric actuator exists between the two boundary conditions, and that this relationship exists for the piezoelectric device alone. Further analysis is needed for a

laminate involving a piezoelectric. It is also critical to note that the 3 direction was simply highlighted by equation [20], and that the 1 and 2 directions will still experience strain (Leo, 2007). The equations that govern those directions are given in equations [26] and [27], and with the blocked stress boundary condition applied in [26] and [27],

$$\varepsilon_{\text{strain},1} = -\frac{\upsilon_{13}}{Y_1^E} * \sigma_{\text{mech},3} + d_{13} * E_3 \quad [24]$$

$$\varepsilon_{\text{strain},2} = -\frac{\upsilon_{23}}{Y_1^E} * \sigma_{\text{mech},3} + d_{23} * E_3 \quad [25]$$

$$\varepsilon_{\text{strain},1} = \left(\upsilon_{13}\frac{Y_1^E}{Y_1^E} * \mathrm{d}_{33} + d_{13}\right) * E_3 \quad [26]$$

$$\varepsilon_{\text{strain},2} = \left(\upsilon_{23}\frac{Y_1^E}{Y_1^E} * d_{\mathrm{e}3} + d_{23}\right) * E_3 \quad [27]$$

The last relevant property is the volumetric energy density. In Figure 18, the area beneath any curve generated is equal to the energy density of the material, or

$$\mathbf{E}_V = \frac{1}{2} * Y_3^E * {d_{33}}^2 * {E_3}^2 \quad [28]$$

This factor is useful for comparing materials on the basis of electromechanical performance, but does not consider any other material properties or design parameters and should therefore only be used as one factor of merit in cross-comparison of various piezoelectric materials (Leo, 2007).

Types of Piezoelectric Actuators

Monolithic

Thus far, only the monolithic type of actuator has been addressed. These elements typically consist of a single body of piezoelectric material laminated or directly

affixed to a conductive substrate. The example shown in Figure 19 is a piezoelectric buzzer with a brass substrate. Typically, there is a conductive paint applied to the top of the piezoelectric disk. These types of devices are also capable of producing small and precise displacements.

Figure 19: A monolithic piezoelectric actuator commonly used as a buzzer or speaker element. (digikey.com part number 102-1127-ND)

With monolithic devices, a critical design problem is the placement of electrodes in such a manner that the area of the electrode is high and the thickness between electrodes is low. Assume that the desired operation mode is 3-3 with practical limitations on the physical dimensions; equations [29] and [30] illustrate the benefit of configuration a. in Figure 20 is more desirable than b. (Leo, 2007).

$$E_3 = \frac{V}{t_P} \quad [29]$$

$$force_{block} = d_{33} * Y_3^E * V * E_3 \quad [30]$$

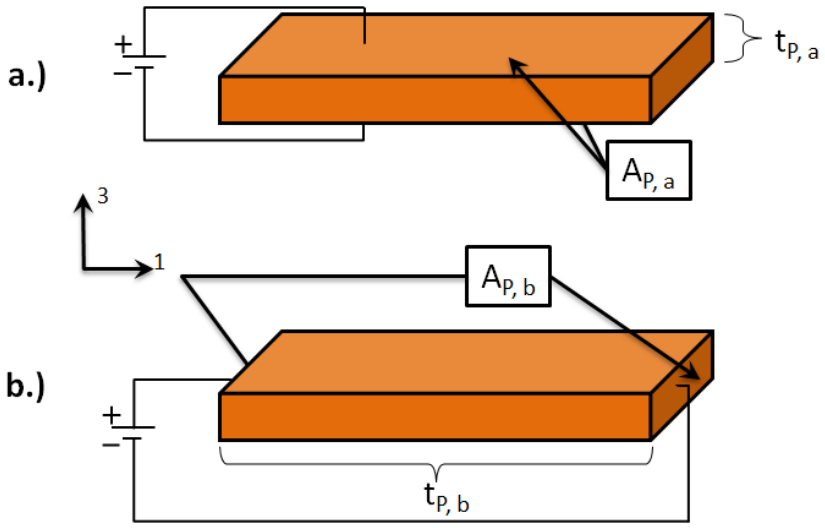

Figure 20: a.) and b.) show an ideal and not ideal placement of electrodes on a monolithic element.
Assume $A_{P,a} > A_{P,b}$ and $t_{P,a} < t_{P,b}$.

As discussed in the previous section, strain occurs in all directions in monolithic piezoelectrics regardless of electrode configuration. Thus, when using monolithic piezoelectric devices as actuators, the difference between the use of the 3-3 operating mode and the 3-1 operating mode is primarily a function of the direction motion that is to be utilized. Typically, the 3-3 mode, as shown in Figure 21, is useful for applications where small displacements in the 3 direction are desired. Using the same device in a 3-1 mode utilizes the lateral motion. The device shown in Figure 22 is an example of an extensional device utilizing the 3-1 effect. Depending on poling and wiring, the directions of the displacements in Figure 21 and Figure 22 can be reversed to make the piezoelectric an extending or contracting device. Figure 22 shows how simply changing

the poling direction of one of the piezoelectric elements changes the device from an extensional device to a bending device, called a bimorph.

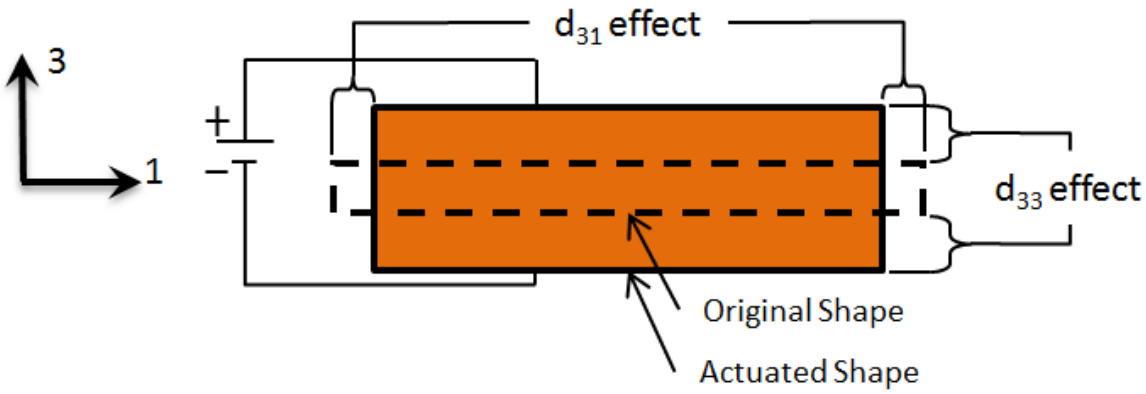

Figure 21: A 3-3 monolithic actuator showing d33 and d31 effects.

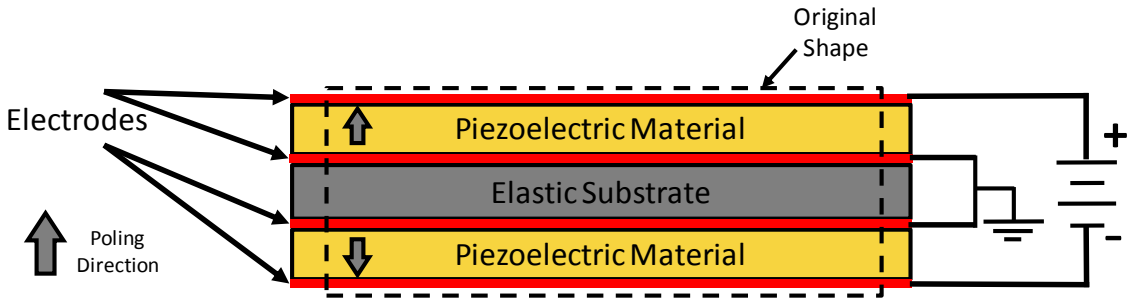

Figure 22: An example of the 3-1 operating mode being utilized to create an extensional device. (Henslee 2009)

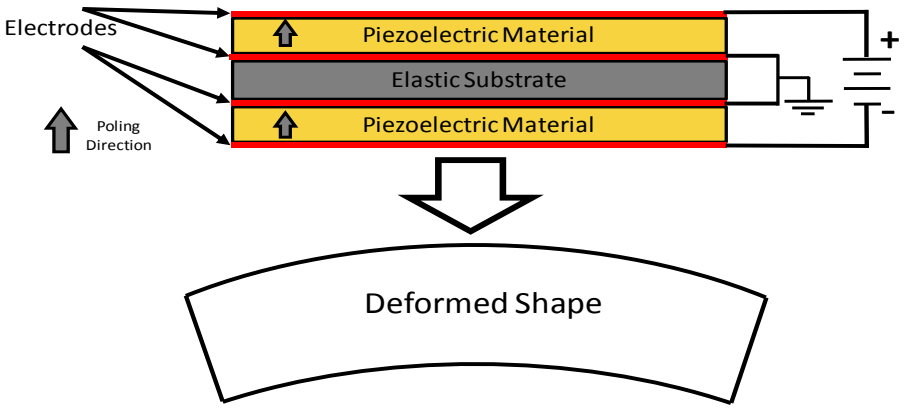

Figure 23: An example of the 3-1 operating mode being utilized to create a bending device, called a bimorph. (Henslee, 2010)

Stack Actuators

An evolution of the monolithic 3-3 mode actuator is the stack piezoelectric actuator. The stack actuator an array of monolithic 3-3 mode actuators arranged and wired as shown in Figure 24. As wired and poled, the device will extend in the 3 direction. A stack actuator is capable of producing much larger displacements at the opportunity cost of the device itself being significantly larger.

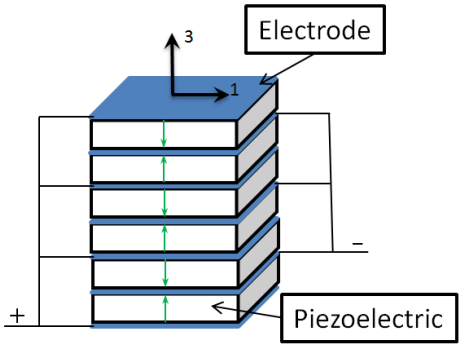

Figure 24: An example of a piezoelectric stack actuator. The green arrows indicate poling direction.

Developments Leading to Piezocomposites

Interdigitated Electrodes

The progression from the stack actuator to the type piezoelectric device analyzed in this study is a logical refinement of geometry and electrode placement. As shown above, a logical area of improvement is the exploitation of the piezoelectric strain coefficient. Ongoing development of piezoelectric devices generally falls under three main categories, design of new materials; geometry of the ceramic or the device; or the placement of electrodes. Developing new materials is a costly process, which doesn't always guarantee success (Bryant, 2008). So a principal focus has been to create new methods of using the d_{33} term of the piezoelectric strain coefficient more effectively.

Currently, the most effect method is manipulation of how the electric field is applied to the piezoceramic. Interdigitated electrodes (IDE) use the principle of electrostatics to move the dipoles. As shown in Figure 25, the electrode patterns on the faces of piezoceramic produce electrical fields that act in-plane with the ceramic. Figure 25 also illustrates how the alternating electrode configuration will make a monolithic piezoelectric act like a 3-3 stack. A drawback to use of IDE configurations are the dead zones that exist as a result of the electrode spacing and ceramic thickness. In these dead zones, the electric field is relatively weak and thus very little dipole movement exists in that area. However, the overall increase in performance by use of IDE's negates concerns about dead zones.

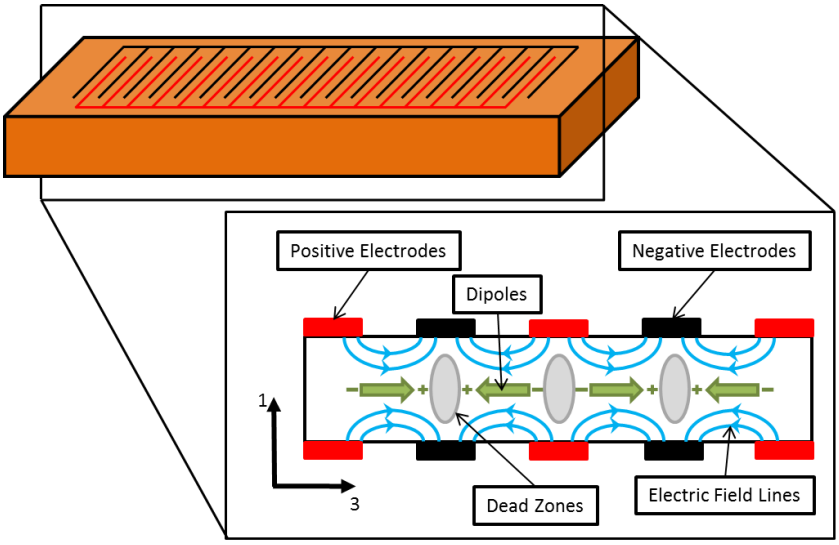

Figure 25: A monolithic piezoelectric device with IDE's. The cross section shows how the IDE's generate flux lines affect the dipole orientation.

Piezoceramic Fiber Composites

Monolithic piezoceramic structures are fundamentally brittle; this means that their application has been somewhat limited due to their poor conformity to non-planar surfaces (W. Wilkie, High, & Bockman, 2002) and lack of durability in high strain applications. The physical form factor of a monolithic stack was often impractical in many cases. A device that also had a high degree of in-plane unidirectionality was desired. It has proved useful to treat piezoelectric systems in a similar manner as fiber-reinforced polymer composite systems. In piezocomposites, shear is the dominant force transmitted from the ceramic to the substrate by the bond of the matrix epoxy that holds the device together and provides the desirable performance as actuators (Bryant Overview). Encasing the brittle ceramic fibers in a polymer matrix makes the system more flexible and more damage tolerant compared to monolithic piezoceramic.

The first piezoelectric fiber composite device, called Active Fiber Composites (AFC), was made using extruded round fibers, as shown in Figure 26. These were developed at the Massachusetts Institute of Technology in the early 1990's, and utilized interdigitated electrodes. The AFC phased out due to the difficulty associated with the manufacturing. These early fiber composites were typically assembled by hand, handling and laying fibers individually (Low Cost). A secondary factor in the phase out of the AFC was the high attenuation of the driving electric field by the large amount of low dielectric matrix material between IDE and fiber. Applying electrodes directly on the fiber was shown to be difficult to achieve with round fibers (Low-Cost). Similar to the dead zones associated with the IDE's, the high attenuation lowered the maximum possible performance of the piezocomposite. A key benefit to AFC's was the improvement in unidirectional strain performance over monolithic piezoelectrics.

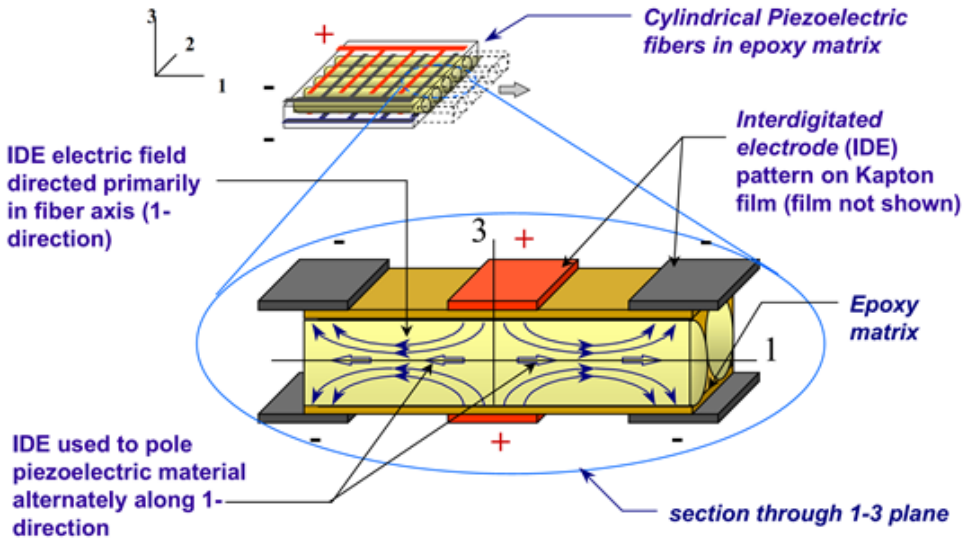

Figure 26: A cross section of the Active Fiber Composite (W. K. Wilkie et al., 2000).

Langley Research Center Macro-Fiber Composite

The AFC was primarily replaced by another piezocomposite called the Macro-Fiber Composite (MFC), which was originally called the LaRC-MFC because it was developed at the NASA Langley Research Center (LaRC). LaRC developed the MFC, shown in Figure 27, to have increased durability, and allow for proper mechanical and electrical contact. LaRC also developed a scalable fabrication methodology that could translate to any active material of the same physical class to make ready-to-use mechanisms. The end result of the process was a lower cost device that was repeatable in its manufacturability (Bryant, 2008).

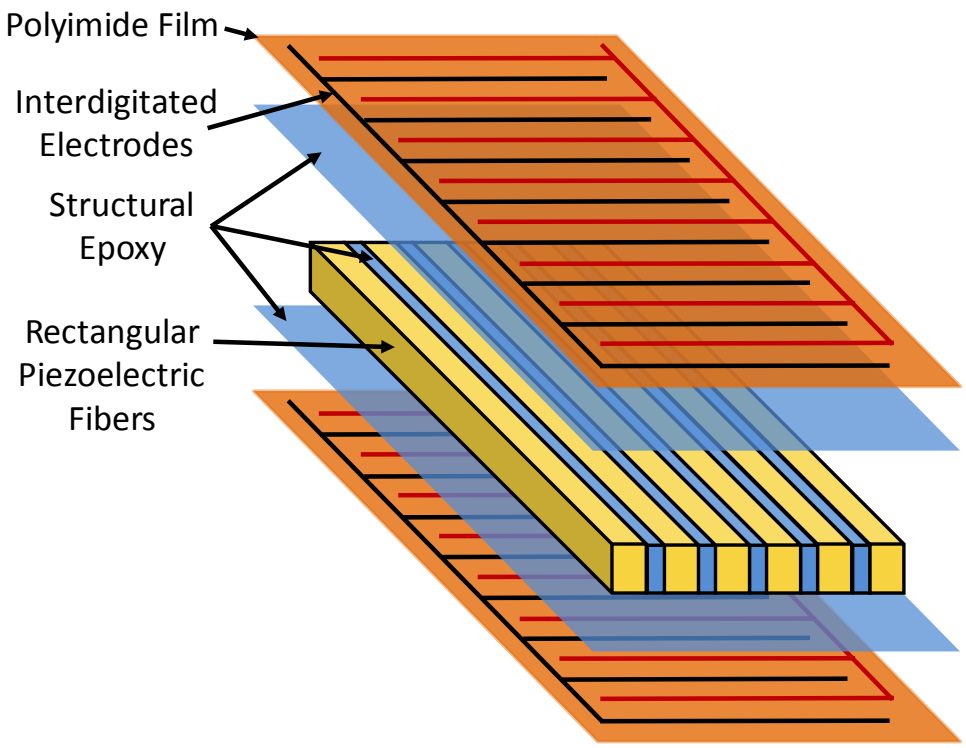

Figure 27: An exploded view of the constituent components that make up the MFC (Henslee, 2010).

The MFC retains most of the beneficial improvements the AFC had, such as high strain energy density, directional actuation, conformability, impact resistance, durability with efficient load transfer, and cyclic fatigue resistance (Bryant, 2008; W. K. Wilkie et al., 2000). The MFC is the piezocomposite of interest to this thesis work; as such, it will be examined in depth.

MFC Manufacturing Process

The manufacturing process is what sets the MFC apart from the AFC. The primary difference between the two is the fibers used. In the MFC, the fibers are made using a computer-controlled dicing saw, shown in part b and c of Figure 28, that cuts rectangular fibers from a single, relatively cheap PZT-5A type piezoceramic wafer, shown in part a of Figure 28. Processing wafers into fibers greatly reduces the cost per unit compared to the round extruded fibers. The piezoceramic wafer is cast on a thin polymer film that acts as a backing to keep the fibers in place during the dicing process. The polymer backing also keeps all of the fibers together in one group, shown in part d of Figure 28, allowing all of the fibers to be handled at once. The backing also keeps the fibers in uniform alignment during assembly. Allowing all of the fibers to be handled at once during assembly reduces the cost per unit and improves directional performance. The individual fiber cross section, shown in Figure 29, is 250 microns wide and 175 microns high. The flat faces of the rectangular fibers allows for intimate contact between the electrodes and fibers, improving performance of the system by minimizing the attenuation seen in the AFC.

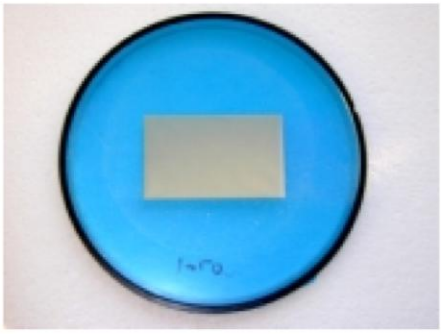

a) 3.375 x 2.25 x 0.007 inch piezoceramic wafer on polymer film.

b) Computer-controlled dicing saw used for cutting wafers.

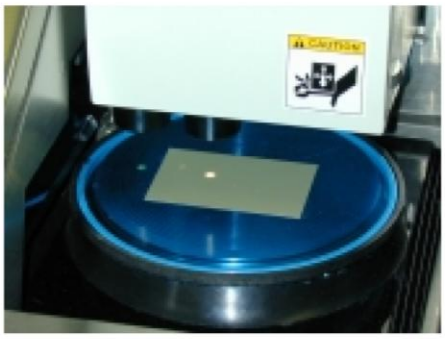

c) Piezoceramic wafer and polymer film frame positioning for cutting.

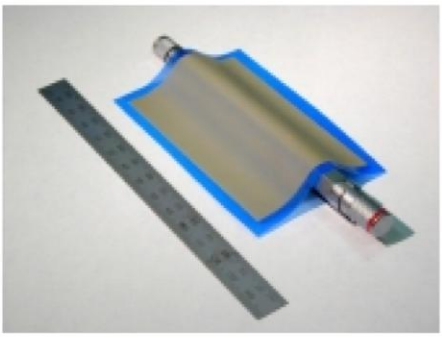

d) Sheet of piezoceramic fibers, after cropping from excess polymer film.

Figure 28: Computer-controlled dicing saw and piezoceramic wafer assembly (W. K. Wilkie et al., 2000).

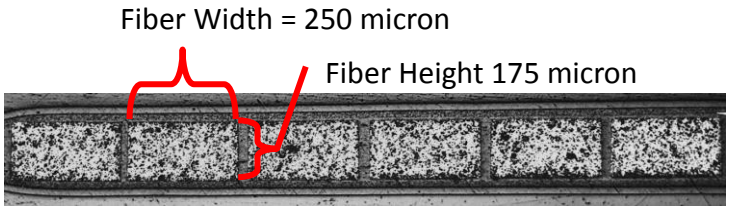

Figure 29: Transverse cross section of MFC fibers.

The electrode layer is made using copper-clad polyimide film. The electrode patterns are generated on the film by a photoresist-and-etch process. A finished MFC is shown in Figure 30, showing the electrode layer. The electrode legs are 175 microns wide at a pitch of 875 microns (W. K. Wilkie et al., 2000). In addition to carrying the interdigitated electrodes, the polyimide film acts as the outside insulating layer of the overall composite structure.

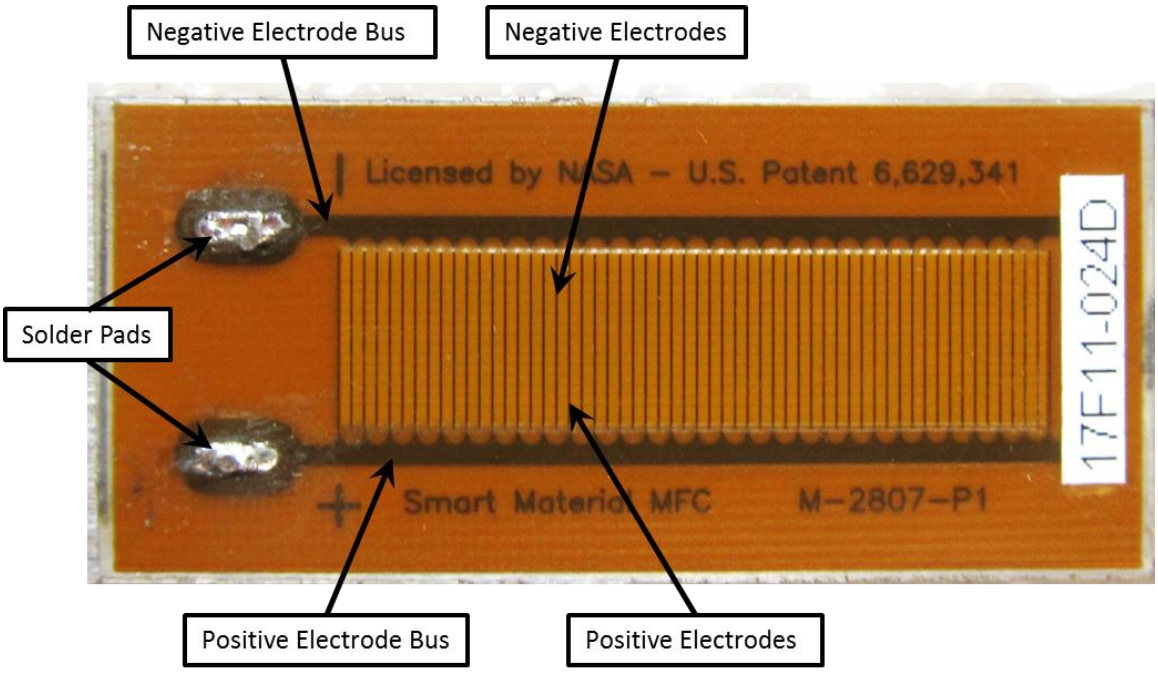

Figure 30: A top view of an MFC manufactured by Smart Material, Model M-2807-P1.

The assembly process, partially shown in Figure 31, is relatively simple in contrast to the manufacturing of the constituent components shown in the exploded view in Figure 27. An electrode layer is placed on a platen with the electrodes exposed, as shown. Loctite DURABOND E-120H thermoset epoxy is spread over the electrodes,

and then the fiber sheet placed on the epoxy (Henslee, 2010). Once the fiber layer is satisfactorily aligned with the bottom electrode layer, the assembly is heat tacked, meaning the epoxy is partially cured such that the epoxy is bonded more strongly to the fibers than the polymer carrier film is. At that point the carrier layer is peeled off and discarded. More epoxy is spread over the fibers, and then the top electrode layer is placed, with electrodes facing down, over the epoxy. The whole assembly is placed in a heated vacuum press to cure. This process allows the excess epoxy to flow into all of the spaces between the fibers and electrodes. The resulting epoxy left between surfaces, called the bond line, is very thin, further improving performance by minimizing the attenuation of the electrical field.

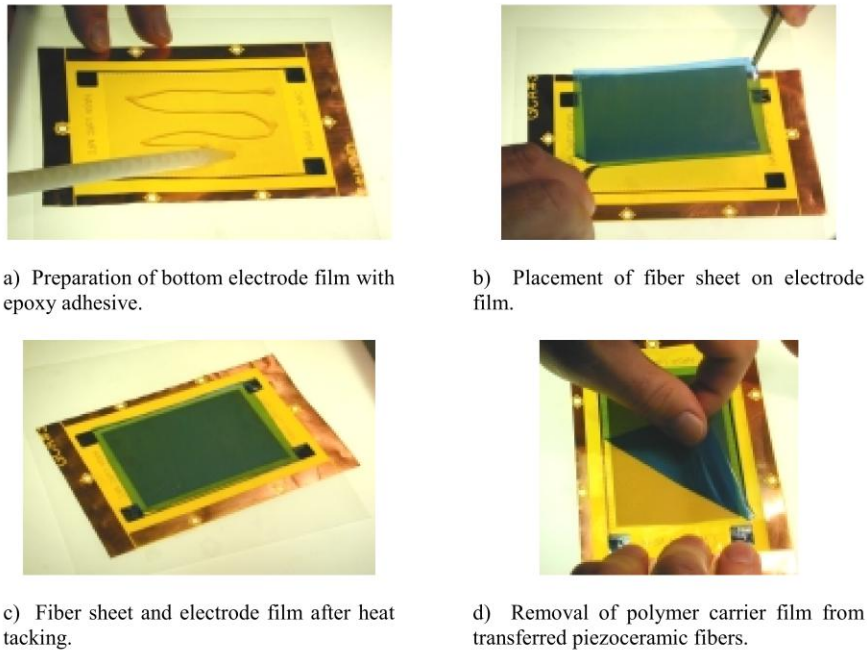

a) Preparation of bottom electrode film with epoxy adhesive.

b) Placement of fiber sheet on electrode film.

c) Fiber sheet and electrode film after heat tacking.

d) Removal of polymer carrier film from transferred piezoceramic fibers.

Figure 31: Part of the assembly process (W. K. Wilkie et al., 2000).

MFC Poling

In addition to being used for actuation, and sensing if applicable, the interdigitated electrodes of the MFC are used for poling the piezoceramic. Note that the components shown in Figure 32, Figure 33, Figure 35 are exaggerated and simplified to aid in visualizing the processes. Figure 32 shows the polarity of the interdigitated electrodes during the poling process. The electric field flows from the positive electrodes to the negative electrodes. During poling, the dipoles orient to be in line with the poling field. The dead zones, as discussed above, still exist in the MFC. In these areas the dipoles are not uniformly aligned, and thus less effective when actuated. However, the overall increase in performance by use of IDE's negates concerns about dead zones.

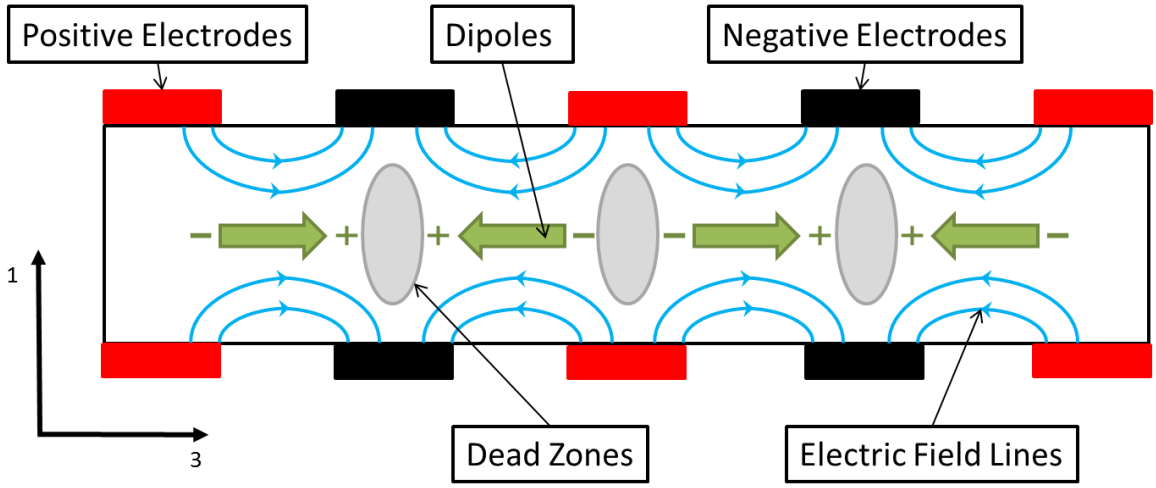

Figure 32: In the poling process, the opposite poles of the dipoles and electrodes are attracted to each other.

The electrode polarity is reversed after poling, as shown in Figure 33. The residual orientations of the dipoles remain. The 3 direction is still referred to as a single

overall poling direction for the bulk material. As in a piezoelectric stack, each segment of material that is divided by the electrodes has a local poling direction that alternates with respect to the bulk poling direction.

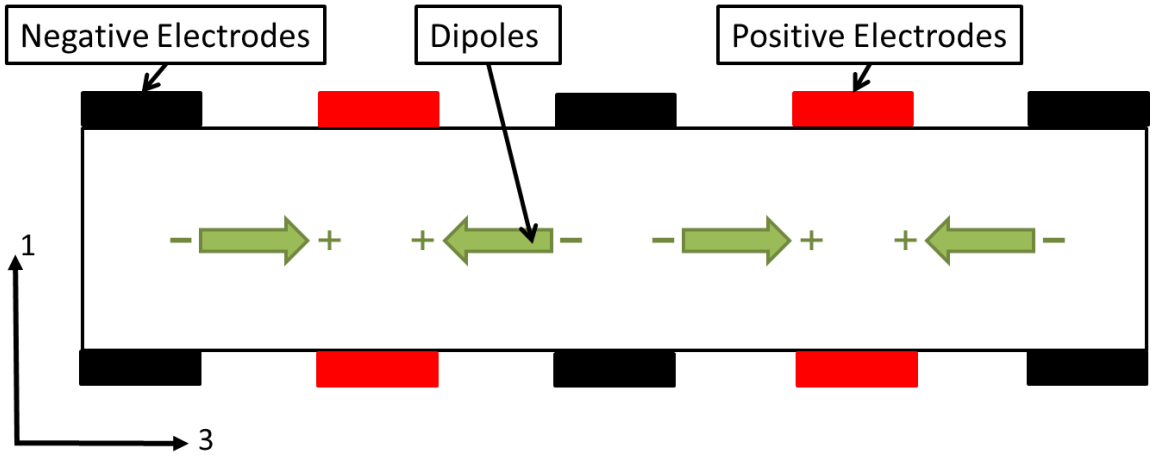

Figure 33: Post poling, the electrode polarity is reversed.

During actuation via a positive voltage, the switched polarity of the electrodes will pull the dipoles farther than a negative voltage. The stress regimes and dipole movement shown in Figure 35 are for a positive applied voltage only. This thesis work operated only in the positive regime. The safe operating range from the MFC manufacturer is -500 Volts to 1500 Volts. Figure 34 shows an example of an MFC strain vs. applied electric field plot for strain in both the longitudinal and transverse directions (W. K. Wilkie et al., 2000). The figure also shows the dipole saturation and a large amount of hysteresis when loading and unloading the MFC. The manufacturer's listed depoling direction applied voltage of negative 500 volts is indicative of protection from depoling via the coercive field.

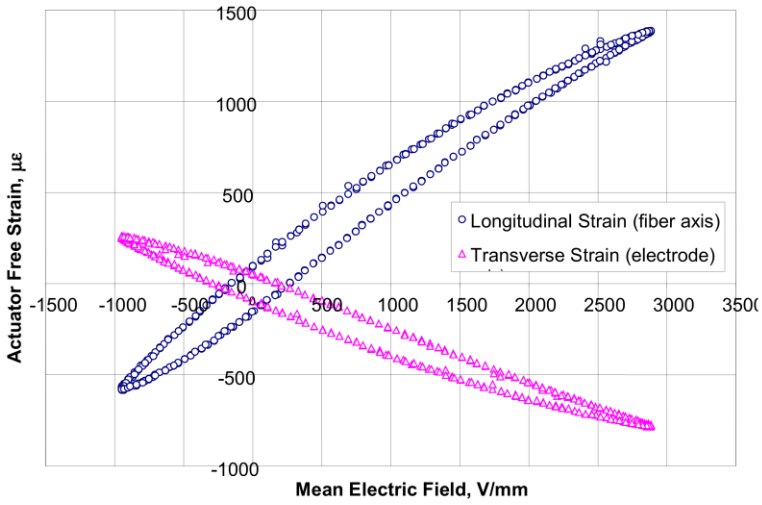

Figure 34: Example of longitudinal and transverse strains in an MFC (W. Wilkie et al., 2002).

Figure 35 illustrates a simplified version of how the dipole movement generates a bulk material deformation. As the dipoles move to align with the applied electric field, there are alternating tension and compression regions.

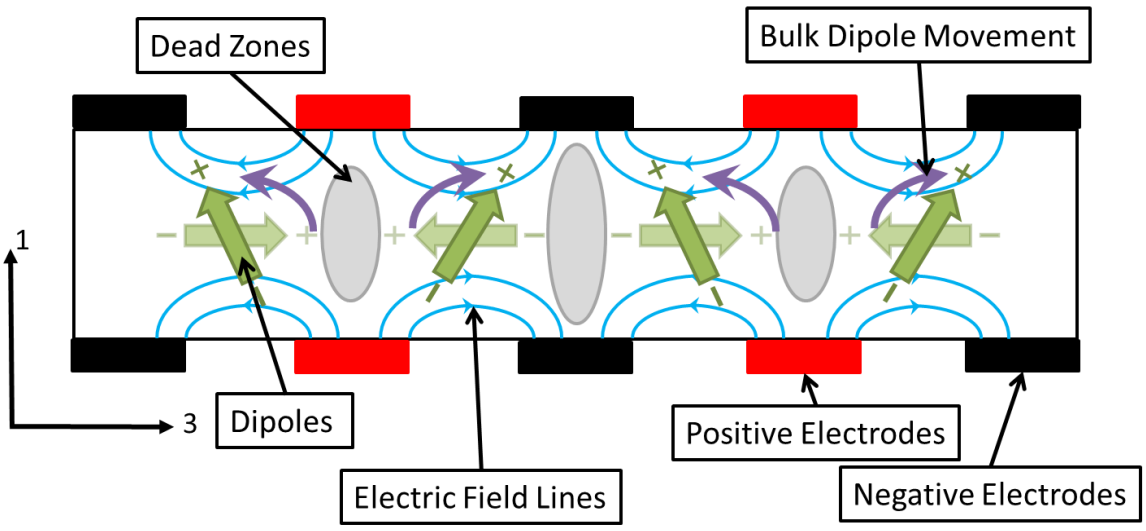

Figure 35: Diagram of the bulk dipole movement during actuation.

MFC Actuation Modeling

Due to the similarities between MFC's and stacks, the equations chosen to describe the behavior of the MFC are the equations specific to the monolithic stack actuating an elastic load. The primary equation set used to estimate the loading conditions with respect to beam geometry comes from Smart Materials by (Leo, 2007). This method of modeling piezoelectric devices compares the ratio of stiffnesses. The beam stiffness is

$$k_{beam} = \frac{3 * Y_{beam} * I_{beam}{}^{3}}{L_{beam}{}^{3}} \quad [31]$$

where

$$I_{xx,beam} = \frac{w_{beam} h_{beam}{}^{3}}{12} \quad [32]$$

and the stiffness of the MFC is most directly found by,

$$k_{MFC} = \frac{F_{block}}{\delta_o} \quad [33]$$

where F_{block} and δ_o are the blocking force and free displacement of the MFC, respectively. Two normalized plots can be generated based on the ratio of displacement of the laminate and free displacement, and the ratio of force of the laminate and the blocked force of the piezoelectric, both are plotted with respect to the ratio of stiffnesses,

$$k_{ratio} = \frac{k_{beam}}{k_{MFC}} \quad [34]$$

$$\frac{u}{\delta_o} = \frac{1}{1 + k_{ratio}} \quad [35]$$

$$\frac{F}{F_{block}} = \frac{k_{ratio}}{1 + k_{ratio}} \quad [36]$$

Furthermore, work output ratio of the system can be defined as,

$$Work = \frac{u}{\delta_o} * \frac{F}{F_{block}} = \frac{k_{ratio}}{(1 + k_{ratio})^2} \quad [37]$$

The resulting plots from the [34] through [37] show the sensitivity of the displacement and force generated by the piezoelectric device with respect to the substrate.

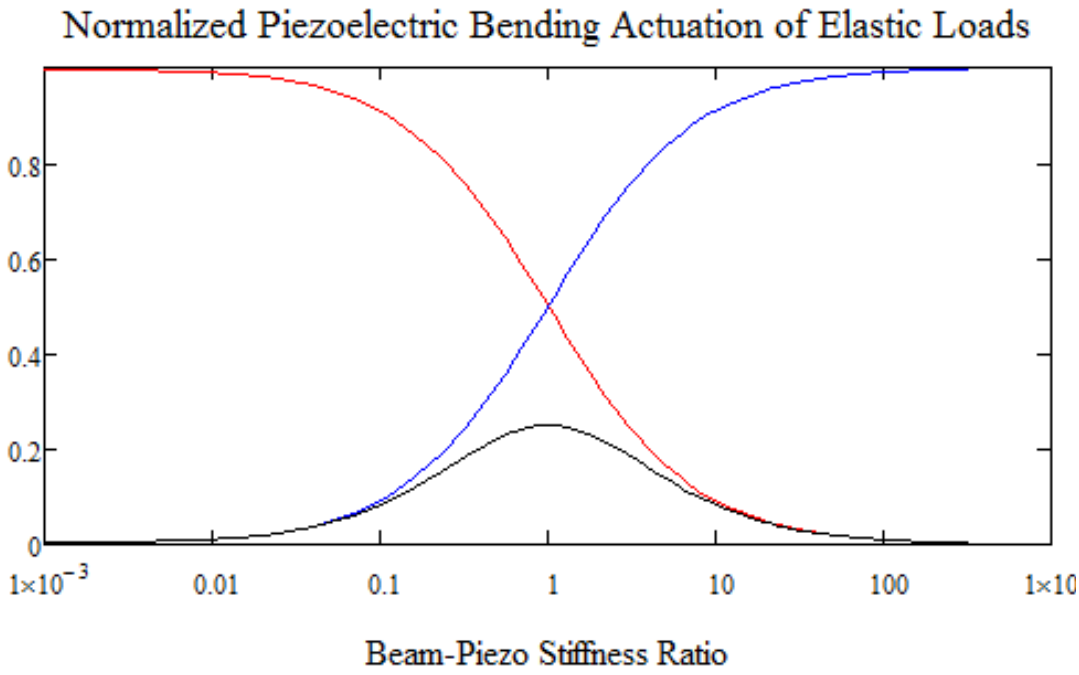

Figure 36: Normalized plots of displacement, force, and work output versus beam-piezoelectric stiffness ratio.

The point where the stiffness ratio is equal to one is called the stiffness match point. At this point, the stiffness of the substrate and the piezoelectric are equal. For design, this plot and equation set is critical for understanding how to size the

piezoelectric for the application. For the purposes of this thesis, these equations and plot are the basis of understanding how beam geometry affects the piezoelectric.

EXPERIMENTAL PROCEDURE

Experiment Overview

Understanding the reliability of a mechanical system is a critical design element. In a dynamic system, such as a piezoelectric actuator, it is important to know how the lifespan of an MFC system will respond to various loading conditions. The goal of this experiment is to simulate a range of loading conditions for the MFC and observe the operational lifespan and actuation performance as a function of actuation cycles. This experiment was designed to build on Henslee's findings and identify what roles geometrical factors play on the expected lifespan of the MFC patches. Where Henslee's testing used temperature as the independent variable, this thesis work used a constant temperature and used geometry as the independent variable. The basis of the experiment is that the response of the MFC patch is dependent on the substrate it is laminated, as demonstrated in the plot in Figure 36 and the equations that developed it. As an electric field is applied, the MFC will experience internal stresses and strains as it transfers energy to the substrate. As shown in above, this is a direct function of the stiffness of the substrate the MFC is mounted to. On a less stiff substrate, the MFC will experience more strain and less stress, whereas on a very stiff the MFC will experience more stress and less strain. At the optimal geometry, the stiffness match point, both stress and strain are balanced, causing the largest amount of work. This work tests

across a six discrete beam stiffness domains to determine if a relationship exists between stress and life, strain and life, or work and life.

To vary the loading conditions, beams with fixed width and length, but varying height were used as substrates. As shown in equations [31] and [32], the height of the beam affects the bending moment area of inertia and thus the beam stiffness is also a function of beam height. The beam heights were selected based on a range between free strain and blocked stress for a single electric field, as well as what was commercially available. The six beam heights used, shown as millimeters (inches), were 0.794 (1/32), 1.191 (3/64), 1.587 (1/16), 3.175 (1/8), 6.35 (1/4), and 12.7 (1/2). The six beam geometries used can be reflected on a plot like Figure 36, shown in Figure 37.

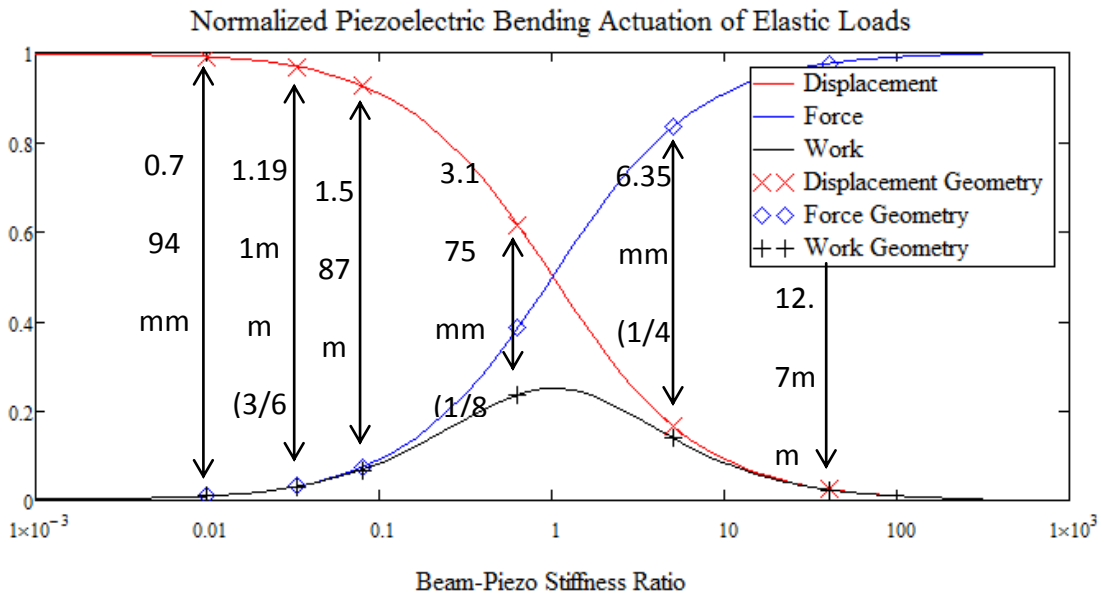

Figure 37: A similar plot as shown in Figure 36, with points marking the six beam geometries of the thesis experiment.

The predominantly seen failure of the macro fiber composite is from an electrical short between a pair of positive and negative interdigitated electrodes. Electrical failure of the piezocomposite is a secondary effect of a material system failure. The previous study, Henslee 2010, showed one possible failure mechanism of the MFC. He showed that within the recommended operating envelope, the MFC actuator would operate orders of magnitude longer than those tested above and below the recommended temperature would. Figure 38 shows how operational lifetime was strongly linked to temperature. The study also showed failure to be caused by a breakdown in the structural epoxy to the point where the dielectric between the interdigitated electrodes becomes low enough to cause arcing at the high voltage potentials, as much as 1.5kV, used to drive the piezoelectric. The high level of heat generated when the electrical arcing occurs is substantial enough to damage the electrodes, epoxy, and Kapton tape. This catastrophic damage is enough to cease all function as an actuator. It is not known how close to the Curie temperature the samples were during actuation. The MFC depends on the electrostatic field generated by the interdigitated electrodes, thus once the system is effectively an electrical short the MFC completely ceases all actuation function.

Based on micrographs of both uncycled and failed specimens shown in Figure 39—from the previous study, it has been shown that significant cracking occurs in the piezoelectric fibers during actuation. As the piezoelectric fibers fracture, they are still held together by the structural epoxy and the MFC tends to maintain an acceptably

consistent level of performance up to time of failure. The overall goal of the experiment is to find the mechanism by which damage accumulates in the MFC constituents.

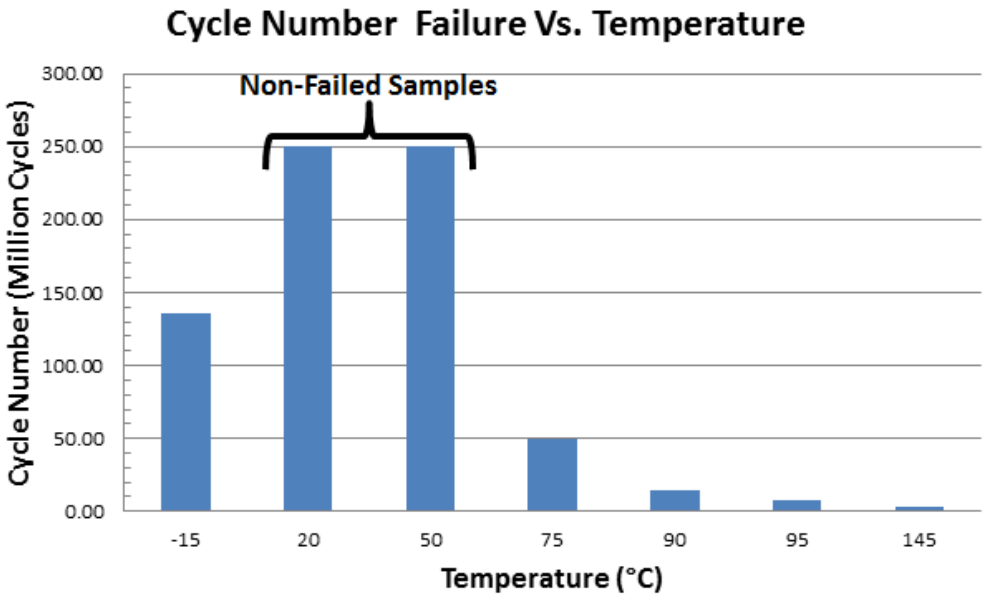

Figure 38: Plot of operational lifetime of an MFC at seven different temperatures (Henslee, 2010).

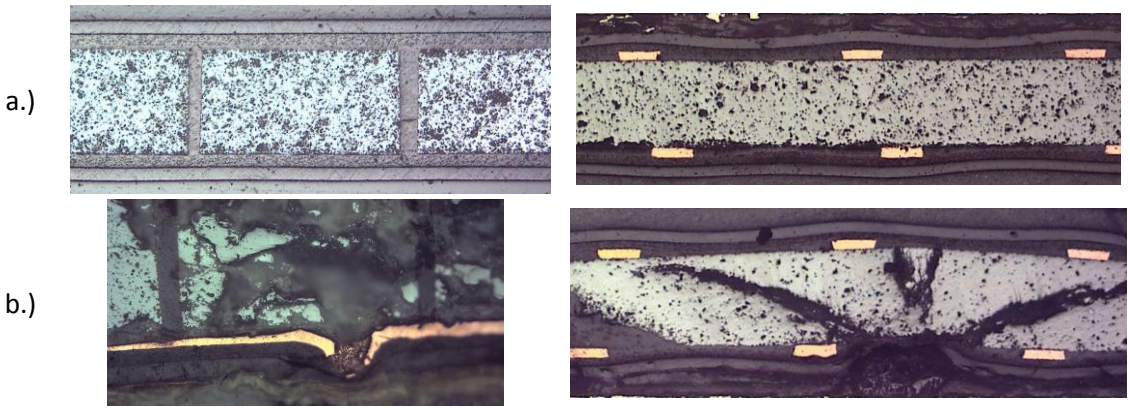

Figure 39: Images from Henslee's study:
a.) Uncycled transverse and longitudinal cross sections.
b.) Failed transverse and longitudinal cross sections.

The primary test fixture consists of a MFC patch laminated to a steel beam substrate, where the MFC is excited by a Trek high-voltage amplifier. The system acts as a unimorph, which in the field of piezoelectric devices is defined as a single piezoelectric mounted to a cantilevered beam. A laser displacement sensor was used to measure the tip displacement. This setup will test the actuation characteristics of the MFC patch over time. All data acquisition was accomplished via a National Instruments USB-6221, and National Instruments LabVIEW.

Experimental Specimen

The beam lamination process mostly used procedures from the previous piezoelectric project with a few key differences. For consistency, care was taken in the material selection process to find a single distributor for the steel beams. All beams are A2 tool steel, three-quarter inch in width, and have a ground finish, with an elastic modulus of The ground finish was desirable to promote proper bonding of the epoxy. Six beam heights were selected based on their correlation to stress and strain for a single electric field. The steel came as eighteen-inch stock and was cut into six-inch pieces using a horizontal bandsaw. Since the MFC patches were to be mounted in the center of each beam, the beams were measured to account for slight variation in beam length; each sample was measured with calipers for total length. The desired measurement for the mounting location was calculated as half the beam length minus half the MFC length. This yielded a distance from one edge of the beam to place one

edge of the MFC. The beams were then marked with their height and sample number. The mounting location was then measured with a caliper and marked with a faint pencil mark.

The mounting procedure utilized 1'x1', 3/8 inch thick, aluminum plates, shown in Figure 40, and clamps to mount multiple samples at once, however to maintain an even distribution of forces, only beams of a single height were mounted at one time. Powder-free Latex gloves were used throughout the mounting process to limit any build-up of oils on the MFC patches, Kapton tape, or steel beams, as well as protect the experimenter from solvents or epoxy. The beams were cleaned using an alcohol-based solvent to remove any excess grease or oils left behind by cutting processes or handling.

Overhead transparency sheets, made from polyethylene terephthalate—a type of polyester, were used as a peel layer because they very smooth and the epoxy bonded poorly to it. The transparency sheets aided the lamination process in two important ways. These transparencies made removal of the cured specimen easy because they shielded the aluminum plates, closed cell foam, and certain areas of the beam from epoxy overflow. Furthermore, an additional sheet was placed over the laminate assembly and fixed with more Kapton to the bottom plate. This effectively eliminated any transverse forces and therefore limited the forces applied to the laminate to the normal direction. Any transverse forces during the clamping process might have shifted the position of the MFC patch on the beam, which would have been highly undesirable.

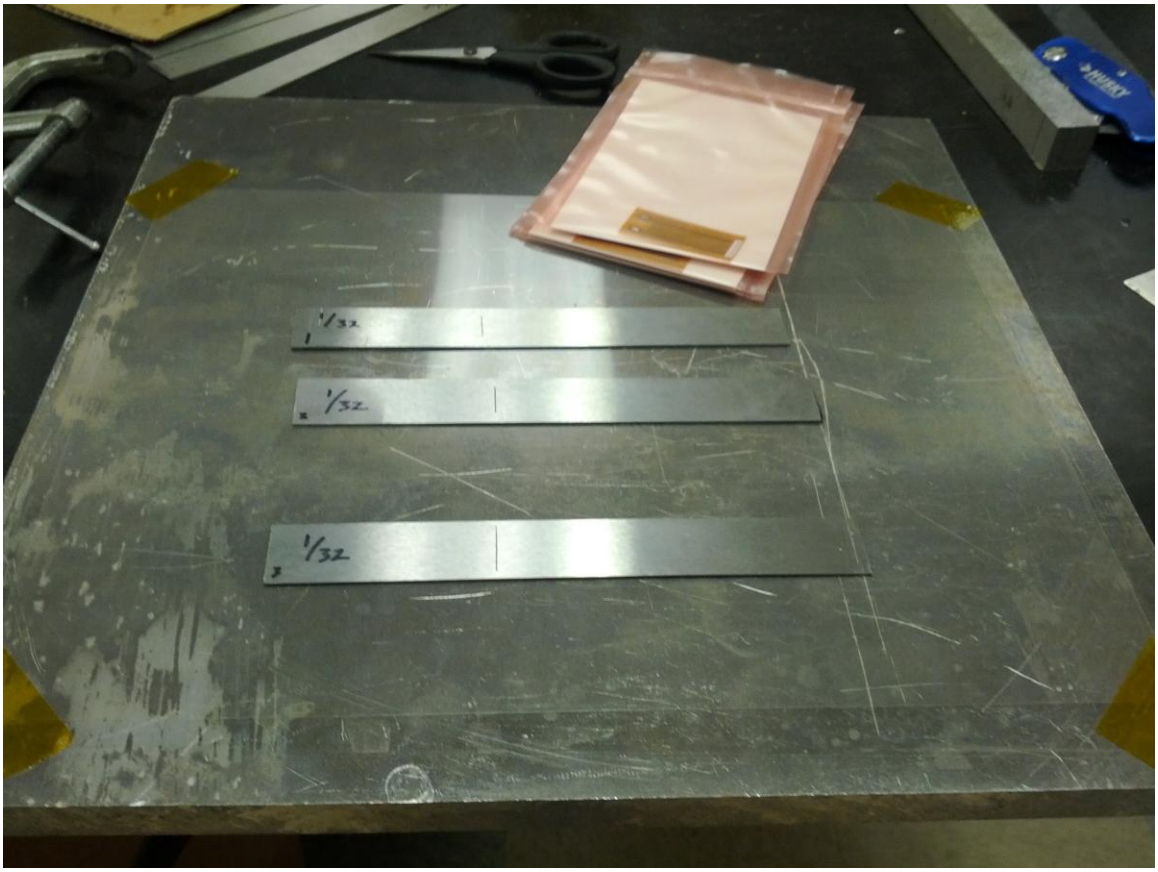

Figure 40: Aluminum plates used as specimen mounting presses.

The lamination began with a transparency sheet taped down to one aluminum plate as a base layer, shown in Figure 40. The cleaned beams were then spaced evenly and taped down to the base transparency using Kapton tape. Since the MFC patch was to be centered on the length of each beam, the beams were taped down on both ends. Cut strips of transparency and Kapton were used as masking to isolate the sections of beam surface that the MFC patch was to be mounted to and to minimize the epoxy build up on undesired sections of the beam. A strip of Kapton tape was then squarely placed over the entire top surface of an MFC patch as both masking and as a hinge. This

subassembly was then placed such that the edge of the MFC patch was squarely affixed on the marked location of the beam. The tape hinge allows the MFC to remain in the desired location while being free to be folded over and allow the application of the epoxy to the beam surface. Figure 41 shows the tape hinge on a sample being used to expose the beam surface.

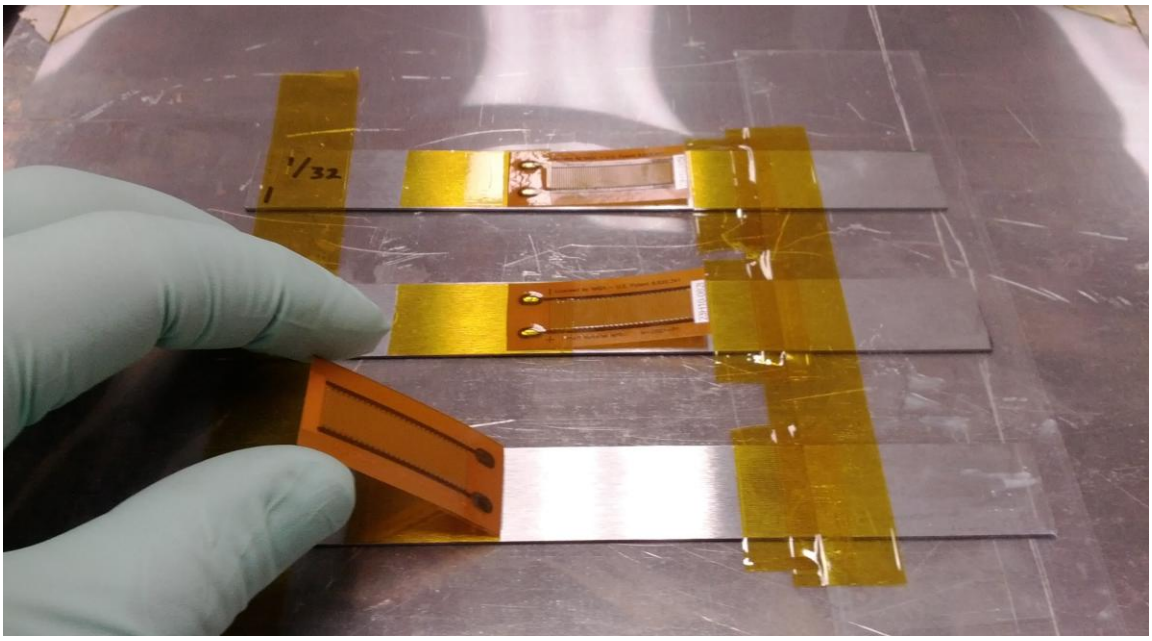

Figure 41: Kapton tape used for thin hinges, masking, and holding the samples in place.

The epoxy used was 3M Scotch Weld Epoxy Adhesive DP 460, a two part thermosetting epoxy system, to bond both the MFC to the beam. This epoxy system has properties mechanical properties that are desirable for this testing. The 3M epoxy applicator uses proportioned tubes to assure the epoxy base and amine accelerator are ideally dispensed and uses a mixing nozzle to assure a proper mixture of the

constituents. The epoxy was dispensed onto a transparency sheet and then transferred to the beam using a small slice of transparency as an applicator. The epoxy was spread over the exposed section of beam and then starting at the tape hinge, the MFC was pressed gently in the epoxy. Then starting at the hinge end again, the MFC was pushed with light finger pressure in rubbing motion to push the excess epoxy out from between the MFC and the beam. This also helped to remove air bubbles trapped in the epoxy.

After the MFC was satisfactorily seated in the epoxy, the last transparency sheet was placed over the beams and taped down to the bottom aluminum plate. A one-inch thick sheet of closed cell foam was cut to one by one foot and placed on top. The foam conforms to any irregularities, such as the electrodes, to allow for a uniform distribution of force over the area of the MFC patch. The matching aluminum top plate was then placed on top of the foam. The whole assembly was then compressed using seven C-clamps. Three clamps were arranged in a triangular pattern with each clamp 3 inches from the center of the plate and four more clamps placed two inches in from each outside corner. The clamps were all hand tightened to approximately the same pressure.

According to 3M's data sheet, the Scotchweld epoxy required 24 hours to fully cure at room temperature, so the clamped assembly was left for at least 24 hours and then the clamps were loosened starting from the three inner clamps and then the four outer clamps. The top plate and foam were removed, and then the transparency and

Kapton layers were carefully deconstructed peeled off, as shown in Figure 42, making sure not to put any excess force on the beam.

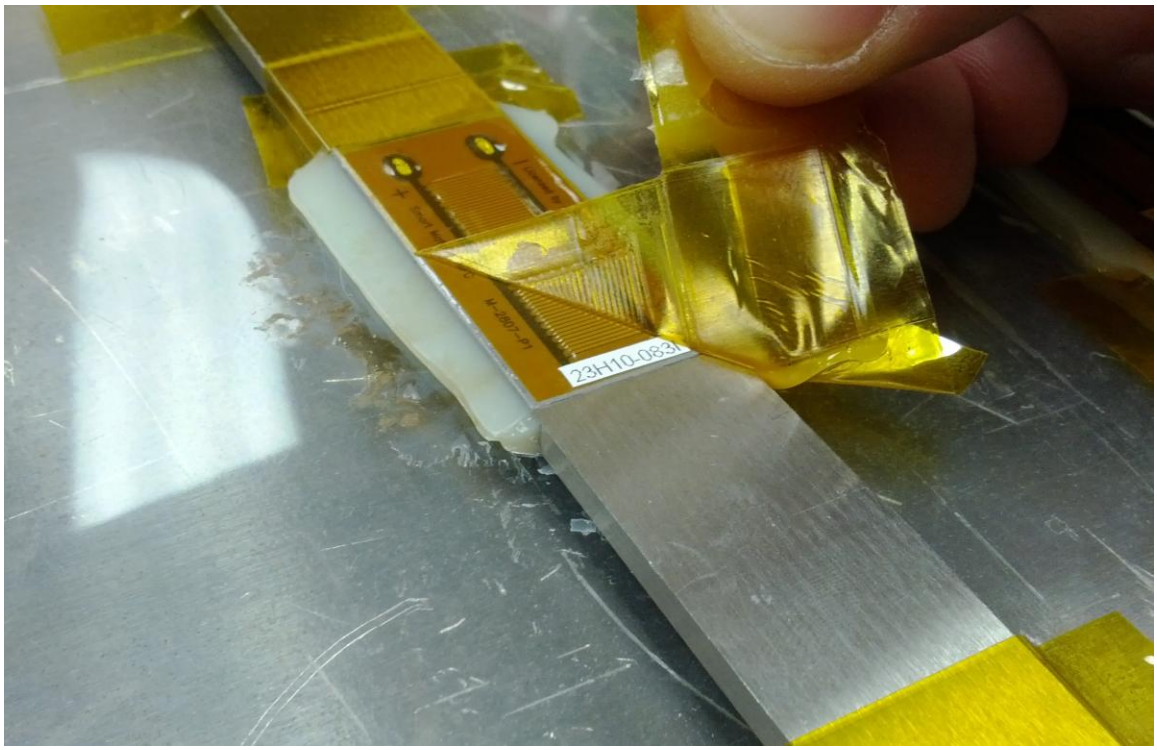

Figure 42: Removing the Kapton masking from the MFC.

The epoxy overflow, which can be seen attached to the side of the beam in Figure 42, had a similar appearance to flashing, such as in plastics forming, and was very easy to break off from the thinner samples, while a razor, shown in Figure 43, was used to separate the epoxy from the thicker samples. The final laminate is shown in Figure 44. The final preparation step was to attach the wire leads to the two solder pads on the MFC patch; these leads are used both for sensing via the DAQ and actuation via the amplifier, depending on the phase of the testing.

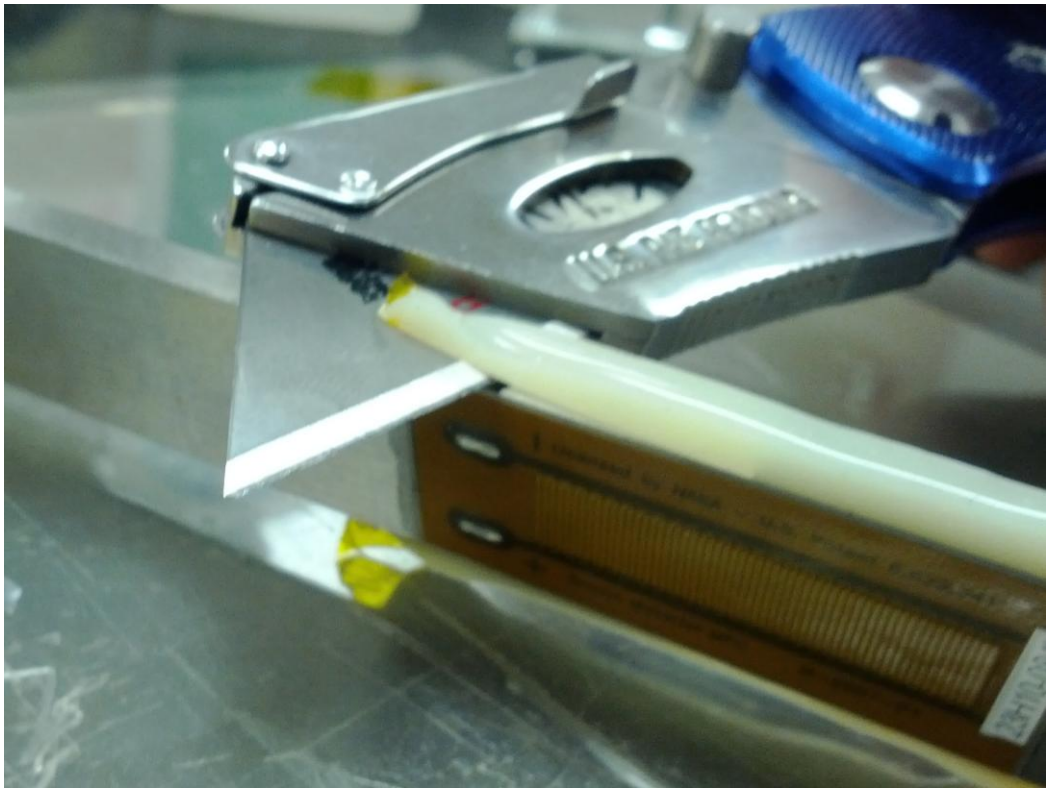

Figure 43: Using a razor blade to separate the epoxy from the steel substrate.

Figure 44: Final unimorph composite.

Instrumentation and Test Fixture

Data Acquisition

LabVIEW is a graphical programming interface developed by National Instruments (NI) that is commonly used for data acquisition. It is especially useful when coupled with NI's line of data acquisition systems. For this experiment a NI USB-6221, shown in Figure XX, was utilized to gather test data. The USB-6221 is capable of logging a cumulative 250 kilosamples per second, divided among all analog channels. The data collection rate was set at 45000 Hz per channel while logging 180 samples.

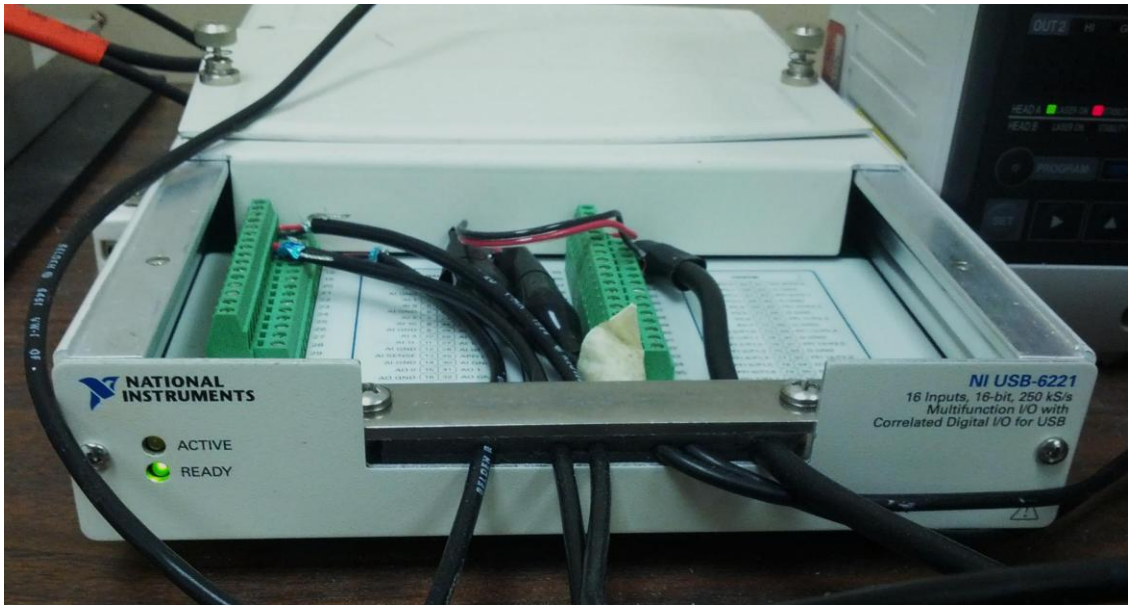

Figure 45: A National Instruments USB-6221 data acquisition box.

Keyence Laser Displacement Sensor

In order to track a performance variable of the composite beam, a Keyence LK-G 30 laser displacement sensor was used to measure tip displacement. The LK-G 30 has a

measurement range of ±5mm at a reference distance of 30mm and is capable of performing at rates up to 50000 Hz. The laser was targeted at the reference distance, at a beam length of 111.5 mm for all samples, and centered on the width. The Keyence controller has several output methods, including USB, Ethernet, analog and serial. For ease of programming in LabVIEW, the analog voltage output was utilized. The analog output of the displacement is scaled as 2 volts per millimeter of displacement.

Figure 46: Keyence LK-G30. The laser head unit (left) connects to the Controller (right).

High Voltage Amplification

A Trek Inc. PZD700D, shown in Figure 48 was chosen as the driving amplifier for this experiment. The PZD 700D can be purchased as bipolar with a range from ±700V, or

unipolar with a range from 0 to 1400 V or 0 to -1400 V. The recommended power range for the amplifier is shown in Figure 47. The PDZ700D is factory set as a 1-to-200 amplifier, meaning that for a one Volt input there are 200 Volts output. The amplifier was overdriven for this experiment to output 1500 Volts, which is the maximum recommended applied voltage the MFC manufacture suggests. This amplifier was primarily chosen because it could accommodate the voltage requirements at a reasonably fast actuation rate. For the specifications of the MFC used, it was determined that approximately 4000 Hz was the fastest rate that the amplifier could be run before the voltage would begin to drop off. The experiment was run at 3750 Hz. One of the other key features that makes this amplifier so well suited to piezoelectric testing is the capability of handling reactive voltage loads generated by direct piezoelectric effect caused by the spring back in the unimorph when the driving voltage is cycled off (Trek, 2011).

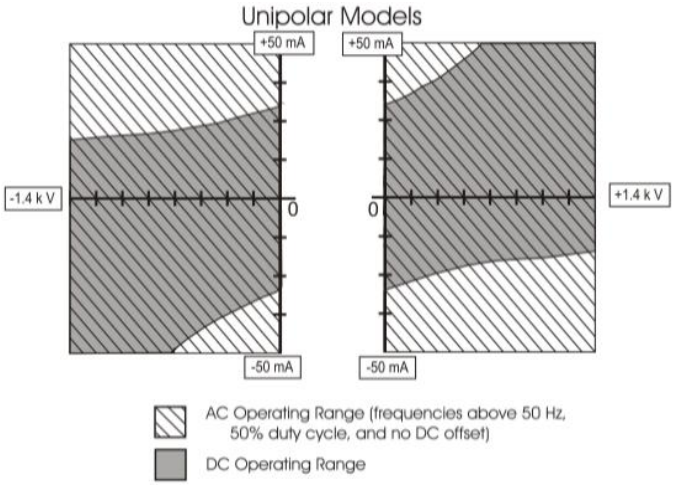

Figure 47: Operating range for the Trek PZD700D (Trek, 2011).

Conveniently, the PZD 700D also has buffered voltage and current monitors that both output in voltage, shown on in Figure 48. The voltage monitor is scaled at 1/200 of the high-voltage output, and has a DC Accuracy of better than 0.1% of full scale. The current monitor is scaled as 0.1 V / mA, and has an accuracy of better than 1% of full scale. These buffered outputs are easily read into LabVIEW as analog voltages. The PZD 700D also features a remote enable function, which enables and disables the high-voltage output with a TTL low and TTL high respectively. This function was controlled as a digital output from the LabVIEW VI (Trek, 2011).

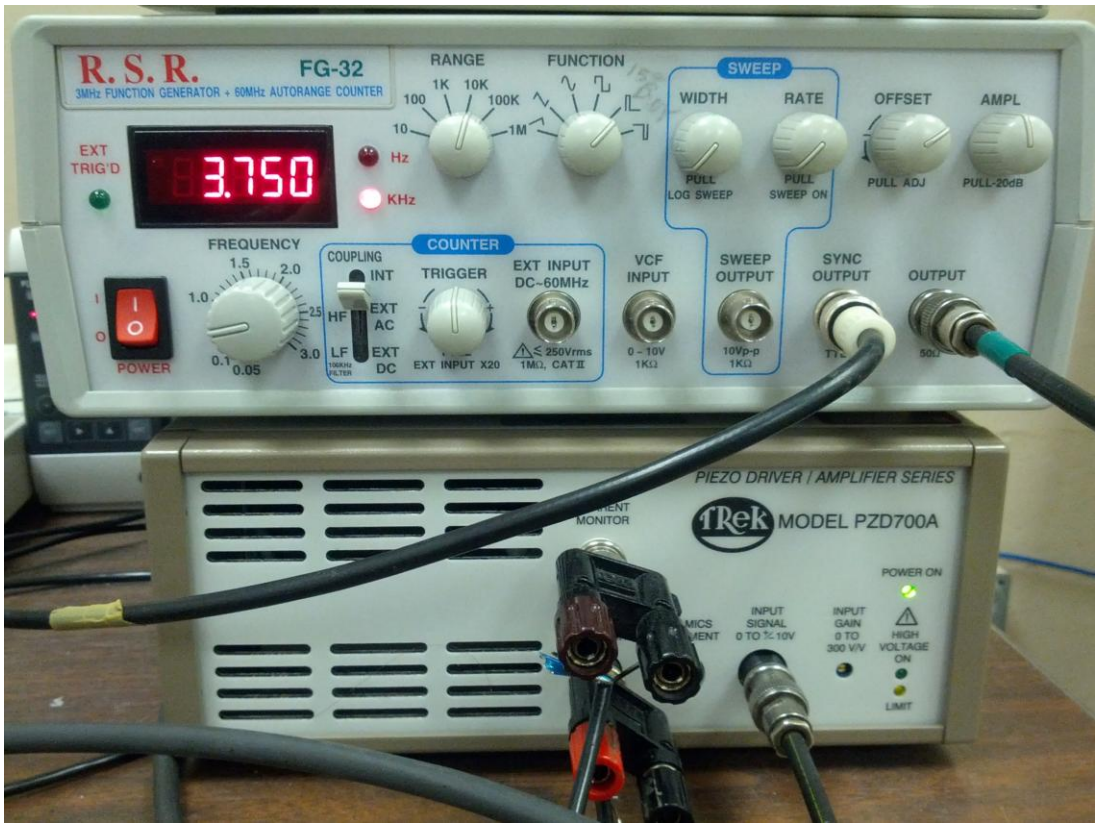

Figure 48: Frequency generator and Trek PZD700D voltage amplifier used to drive the MFC.

Figure 49: Rear view of the Trek PZD700D.

Also shown in Figure 48 is the RSR FG-32, the function generator used as the input voltage for the amplifier. The FG-32 was configured to output a positive rectangular pulse, with a voltage amplitude of 0 to 7.5 Volts, a 15% duty cycle, and a frequency of 3750 Hz. The TTL level sync output of the FG-32 was connected to the USB-6221 to be used as a cycle counter.

Setup of Equipment

A schematic of the power and data electrical connections is shown in Figure 50. The trek amplifier outputs are well buffered and isolated from the power circuit, and very little noise was shown in the signal. The wires for the data and the wires for the high voltage output were also kept physically separated, despite being shielded, to reduce electromagnetic interference.

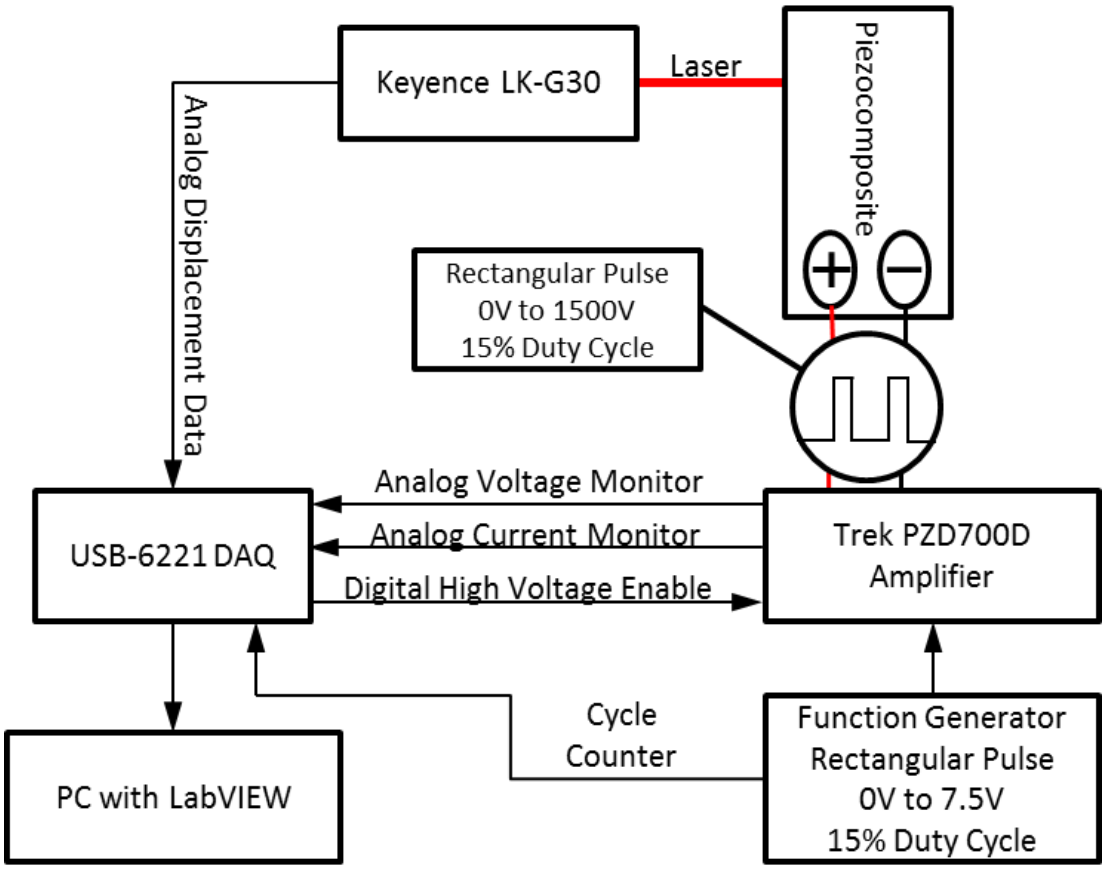

Figure 50: An overview of the driving circuit and data logging.

The test fixture shown in Figure 51 shows the ceramic terminal blocks used for strain relief and the quick disconnect in the middle of the wires between the solder point on the piezoelectric patch and the last ceramic block that eased the changing of samples. The wires that connected to the piezoelectric could easily be removed from a failed specimen and soldered to another specimen without having to unscrew the wire from the ceramic terminal block.

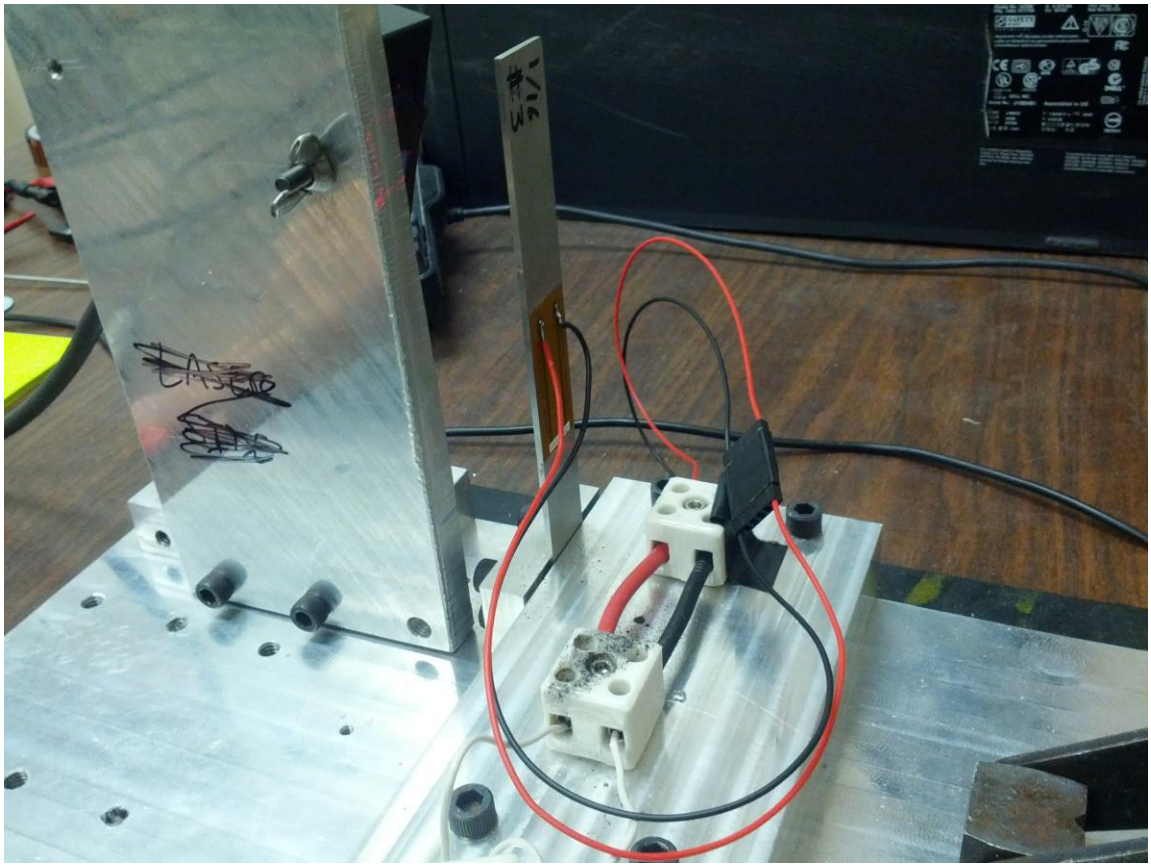

Figure 51: The experimental test fixture.

Figure 51 shows the slot cut in the laser support block to facilitate quick access to the sample clamping block. A machinist square was used to make sure the sample was square with the fixture, and then the laser was placed at the correct zero point for the beam height being tested. The laser block assembly was adjusted until the laser controller shown in Figure 46 read zero. Error caused here by the placement of the laser was handled later in post-processing of the data.

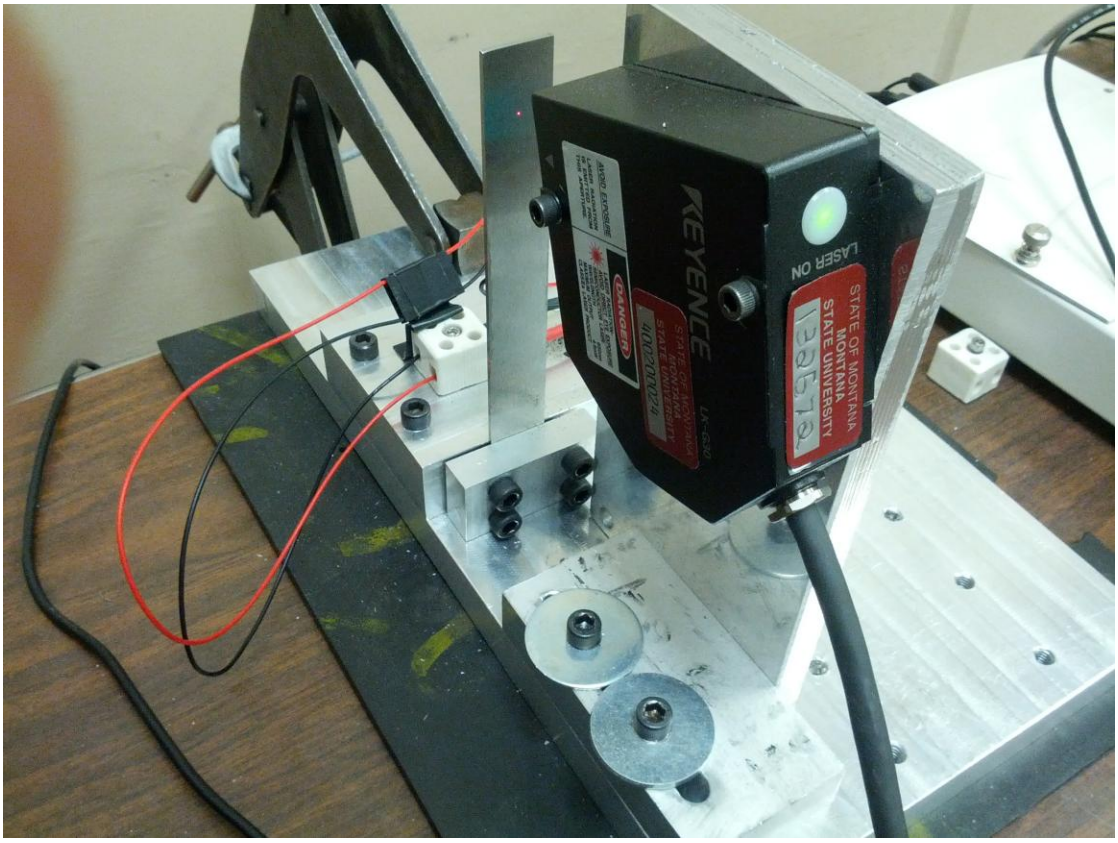

Figure 52: The aluminum support block holds the unimorph and the laser rigidly.

Microstructure Imaging

Optical Microscopy was conducted on all unimorph samples using the Nikon SMZ-1500, shown in Figure 53, located in the ICAL Laboratory at Montana State University. The Nikon SMZ-1500 is Nikon's top-of-the-line stereoscopic zooming microscope with a zoom that ranges from 0.75x to 11.0x magnification. The microscope is equipped with a digital camera for saving images to be viewed later or used in a thesis such as this.

Figure 53: Nikon SMZ-1500, used to examine the microstructure of the samples.

Vibration Analysis and Verification

Since this experiment was to be operated at one frequency across all beam heights, but not to be operated at resonance, foundation work needed to find the resonance frequencies of each beam. The primary reason resonance was avoided is the differences in amplitude and mode shapes, as each beam will be operating between

various modes, as shown in Table 3. These factors might have influenced the electromechanical response of the piezoelectric non-uniformly across the height spectrum. Based on the Trek amplifier's operating conditions for the specific piezoelectric used, the target testing frequency was 3750 Hz to avoid voltage drop-off. Analytical and numerical beam vibration analyses were conducted to find the natural frequencies and mode shapes.

The analytical analysis method used to calculate natural frequency was the boundary value solution for a fixed-free cantilever beam as described in the textbook Mechanical Vibrations by S. Rao. The natural frequency can be found by

$$\omega_n = (\beta_n)^2 * \sqrt{\frac{E * I_{xx}}{\rho * A * L^4}}$$

Where E is the elastic modulus of the beam, I_{xx} is the moment area of inertia of the beam about the bending axis, ρ is the density of the beam, A is the cross-sectional area of the beam, and L is the length of the beam. A direct value of $(\beta_n * L)^2$ is given by the solutions to the equation

$$\cos(\beta_n * L)^2 * cosh(\beta_n * L)^2 = -1$$

The natural frequency given above is in radians per second, and thus to compare to the empirical and numerical data, must be divided by 2*π to return a value in cycles per second. The results of the analytical calculation method are given in Table 2. For consistency for the following comparisons, the beam length used in the analytical calculation for the 1.587mm (1/16") beam was the length of specimen number three.

All other beam lengths used in this calculation were averages of the lengths of beams for that height (Rao, 2011).

Table 2: Results of the analytical solutions to natural frequencies in the transverse direction. The shaded rows are the frequencies that bracket the driving frequency of 3750 Hz.

Beam Height mm (in)					
0.794 mm (1/32”)	1.191 mm (3/64”)	1.587 mm (1/16”)	3.175 mm (1/8”)	6.35 mm (1/4”)	12.7 mm (1/2”)
Beam Length mm(in) Note: Except for 1.587mm (1/16”), all lengths are averages					
128.024 (5.0403)	129.525 (5.0994)	128.9 (5.0748)	129.07 (5.0815)	128.384 (5.0545)	128.509 (5.0594)
Frequency (Hz)					
40.08	58.73	79.07	157.72	318.82	636.4
251.16	368.05	495.51	988.4	1997.98	3988.23
703.25	1030.56	1387.43	2767.56	5594.41	11167.15
1378.08	2019.49	2718.82	5423.31	10962.81	21883.17
2278.08	3338.37	4494.42	8965.16	18122.38	36174.6
3403.06	4986.95	6713.89	13392.4	27071.71	54038.6
4753.03	6965.25	9377.25	18705.08	37810.91	75475.4

The discrete numerical analyses of the beam natural frequencies were carried out using ANSYS, the results of which are shown in Table 3. The principle commands used were ANTYPE, MODOPT and MXPAND. The ANTYPE command sets the analysis type, which in this case is set to modal. MODOPT specifies modal analysis options, such as the number of mode types to extract, the frequency range to examine, and what method to use. It is important to note that the ANSYS model used included all mode shapes, not simply the transverse modes as the analytical model does.

Table 3: Results from ANSYS finite element solutions to the natural frequency of the beams. The shaded rows are the frequencies that bracket the driving frequency of 3750 Hz. The green shaded rows are transverse mode shapes and the yellow shaded rows are torsional modes. Credit: Tyler Tempero

Width mm(in)													
0.794 mm (1/32")			1.191 mm (3/64")		1.587 mm (1/16")			3.175 mm (1/8")		6.35 mm (1/4")		12.7 mm (1/2")	
Specimen Number													
1	2	3	1	2	1	2	3	1	2	1	2	1	2
Length (inches)													
5.024	5.0374	5.0594	5.1012	5.0976	5.0445	5.0654	5.0748	5.072	5.0909	5.0453	5.0638	5.0488	5.0701
40.844	40.627	40.272	59.405	59.488	80.928	80.26	79.96	159.92	158.73	322.33	319.97	639.63	634.3
255.82	254.46	252.24	372	372.52	506.62	502.45	500.57	937	930.16	947.73	940.92	948.07	940.25
534.76	533.28	530.86	782.91	783.48	946.6	938.94	935.5	999.2	991.8	1997.6	1983.2	3841.8	3811.1
717.58	713.75	707.52	925.84	927.1	1046.2	1041.7	1039.7	1996.5	1988.8	3596.7	3583.2	5347.3	5324.7
953.87	948.88	940.76	1043	1044.4	1419.6	1407.9	1402.7	2790.1	2769.5	5430.8	5394.9	5431.4	5390.2
1412.2	1404.7	1392.4	2051.1	2054	2789.5	2766.5	2756.2	5374.7	5338.6	5505.2	5466		9981.4
1622.6	1618.1	1610.6	2374.7	2376.4	3173.3	3159.5	3153.2	5454.1	5414.1		9985.1		
2351.6	2339.1	2318.7	3412.6	3417.3	4635.9	4597.8	4580.7	6047.4	6023.7				
2765	2756.9	2743.7	4043.3	4046.4	5403.7	5379.2	5367	9004.2	8938.5				
3553.4	3534.4	3503.6	5151	5158.2	5425.7	5385.2	5368.2	9963.7	9926.6				
3997.3	3985	3965	5316	5322.7	6987.7	6930.4	6904.7						
5048.3	5021.4	4977.7	5839.1	5843.7	7803.8	7767	7750.4						

ANSYS is also capable of providing three-dimensional renders of each mode shape. Focusing on the 1/16 inch beam again, the bracketed mode shapes for specimen three are shown in Figure 54 and Figure 55. Figure 54 shows that at approximately 3.15 kHz, the shape of the resonance is a twist about the length axis, while Figure 55 shows that at approximately 4.58 kHz the mode shape in the transverse direction. This correlates well with the fact that in analytical data a transverse natural frequency was found at 4.55 kHz.

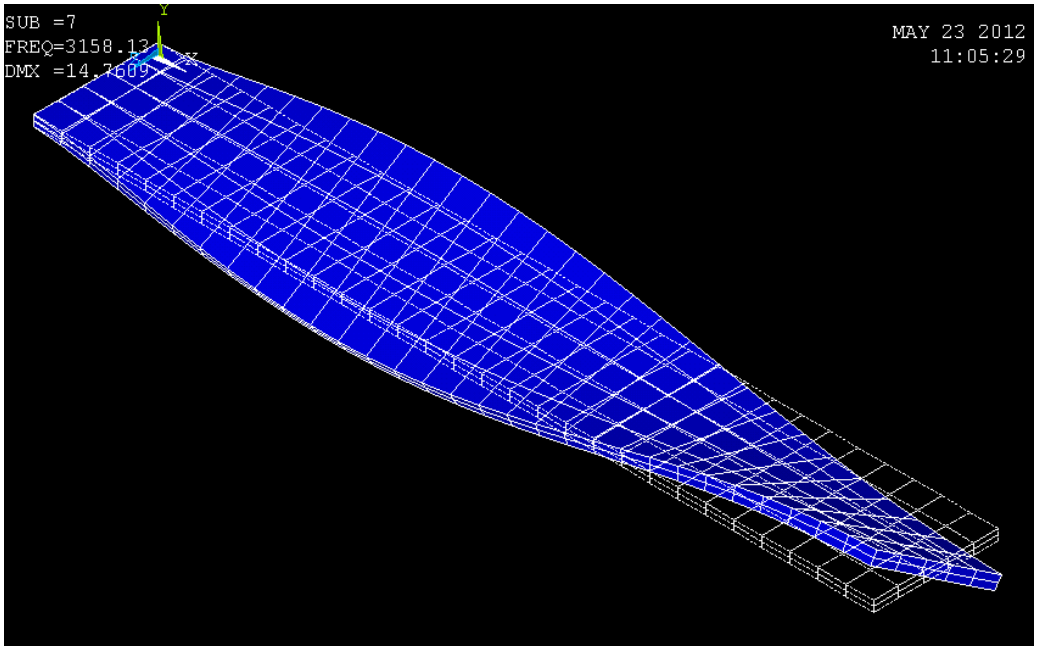

Figure 54: 1.587mm (1/16”) Beam, Torsional resonant mode shape at 3.158 kHz.

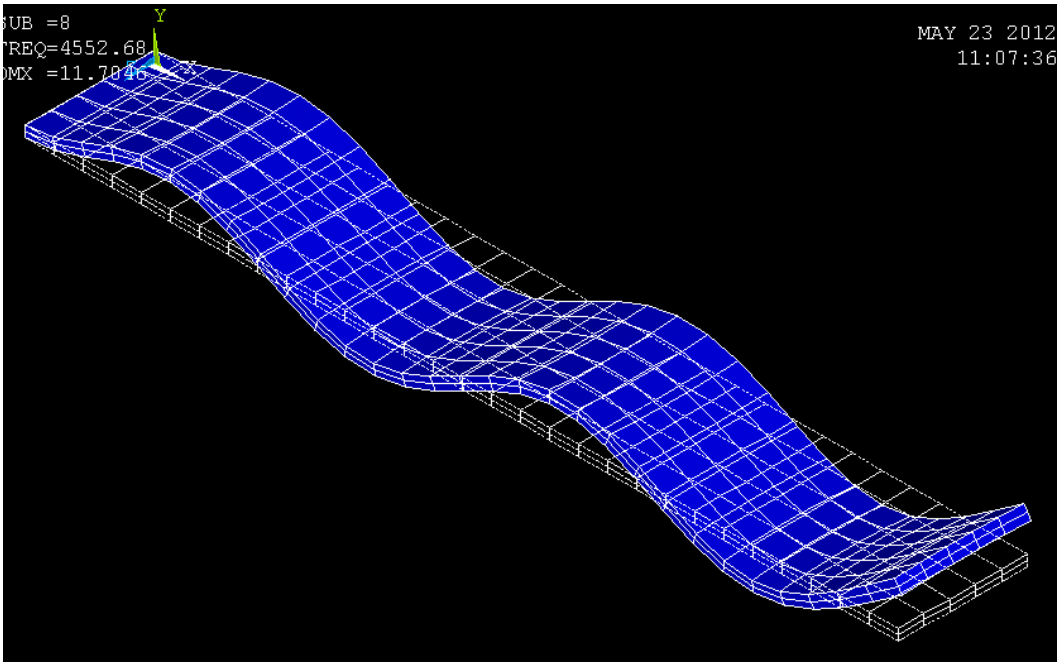

Figure 55: 1.587mm (1/16”), Transverse resonant mode shape at 4.552 kHz.

An empirical set of data was also generated for natural frequencies using one of the virgin 1.587mm (1/16”) beams. The results of the observations are tabulated and displayed with the ANSYS model results in Table 4, along with the percent error between the two.

Table 4: Observed, ANSYS, and analytical resonant frequencies for 1.587mm (1/16”) beam #3.

Measured (Hz)	ANSYS (Hz)	Analytical (Hz)	Measured-ANSYS Percent Error	Measured-Analytical Percent Error	Analytical-ANSYS Percent Difference
77.7	79.96	79.07	2.83	-1.73	1.13
508	500.57	495.51	-1.48	2.52	1.02
709	935.5		24.21		
1060	1039.7		-1.95		
1318	1402.7	1387.43	6.04	-5.00	1.10
2628	2756.2	2718.82	4.65	-3.34	1.37
3227	3153.2		-2.34		
4870	4580.7	4494.42	-6.32	8.36	1.92
5271	5367		1.79		
	5368.2				
6809	6904.7	6713.89	1.39	1.42	2.84
7738	7750.4		0.16		
9715	9781.8	9377.25	0.68	3.60	4.31

The beam was set up in the test fixture as per test procedure, and then the driving frequency was manually swept from zero to 5000 Hz. Identifying modal frequencies of the beam was obvious by observation, but also through the output of the laser. When visually observed at resonance, the beam would have deflection capable of leaving a persistent image. For reasons unknown, the laser was unable to track the

beam displacement at resonance. The laser controller would simply show "-FFFFFF," which normally indicates that the displacement is out of range, but in this case it is more likely that at resonance not enough light was reflected back into the sensor. At "-FFFFFF" the controller outputs -10.5 Volts, which is out of range for the USB-6221 and in LabVIEW looks like signal "clipping." Using these two techniques to identify resonance, the frequency was manually swept and modal frequencies were recorded. The bandwidth of the resonance frequency, by observation is less than 10 Hz. Table 4 shows the observed resonant frequencies identified by this method as well as the resonant frequencies found via the ANSYS and analytical methods.

The high level of correlation between the three sets of data indicates that the data in Table 3 is a good approximation for the composite beams' natural frequencies. This leads to the conclusion that the driving frequency of 3750 Hz is not a modal frequency for any beam geometry. However, the data indicates that the beams do appear to be affected by the deformation modes, possibly reducing the reliability of deflection that the Keyence LK-G30 could detect at a single point on the beam. Ideally, a two dimensional surface with displacement as a third dimension would have been a better tool than the single point of displacement data gathered. This would allow for a more accurate picture of the deflection of the beam and yield better back-calculations of the performance of the piezoelectric. A device such as a Polytec PSV-400-3D-M high frequency scanning vibrometer would be an ideal device to use for future experiments.

Data Aliasing Verification

Aliasing, in the context of this experiment, pertains to using a sufficient number of samples to record a signal in a given time frame. If the rate of samples collected is too slow, there is not enough information to accurately describe the deflection. This can generate the appearance of a lower frequency or lower amplitude signal in the resulting dataset. Figure 56 shows a potential result of undersampled data. Theoretically, a signal cannot be oversampled, but practical limitations exist in the data acquisition hardware and computing hardware that limit how fast a signal can be sampled and recorded. For example, the USB-6221 DAQ used for this experiment has a maximum analog data collection rate of 250,000 samples per second, to be divided among each analog channel used. The other primary limitation is the amount of data that can be physically stored on a computer's hard disk drive to be post-processed.

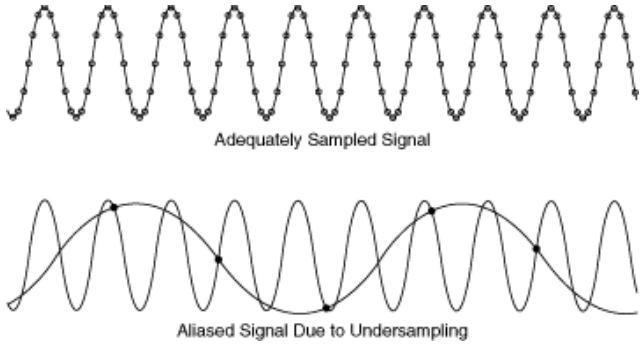

Figure 56: Examples contrasting appropriately sampled and under sampled signals (Instruments, 2004).

The Nyquist theorem describes the minimum sampling frequency required to accurately represent a signal. To satisfy the Nyquist theorem, the sampling signal,

termed the Nyquist frequency, f_N, must be two times greater or equal to the highest frequency component of the signal. Thus, in theory, the driving frequency of the piezoelectric being 3750 Hz requires a minimum sampling rate of 7500 samples per second.

The base data collection rate of the experiment was 45000 samples per second. At the driving frequency of 3750 cycles per second, there were 12 samples recorded per cycle. To confirm this data collection rate was sufficient to avoid aliasing of the data, a sample was run at the same test parameters with the exception of the data collection rate. The data collection rate was raised to 82500 samples per second in each channel and the experiment was run again on a 1/16 inch beam. At 82500 samples per second, there were 22 samples per cycle recorded. Figure 57 and Figure 58 show the difference in a typical cycle. The number of data points in each graph matched the calculated above, 12 and 22 samples respectively. Additionally, the shapes of the cycle are approximately equal despite not being the same data set.

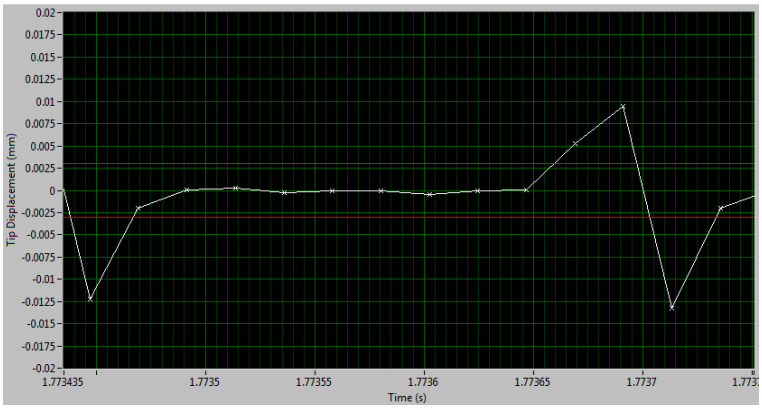

Figure 57: A typical graph of tip displacement of a single cycle at a data collection rate of 45000 Hz.

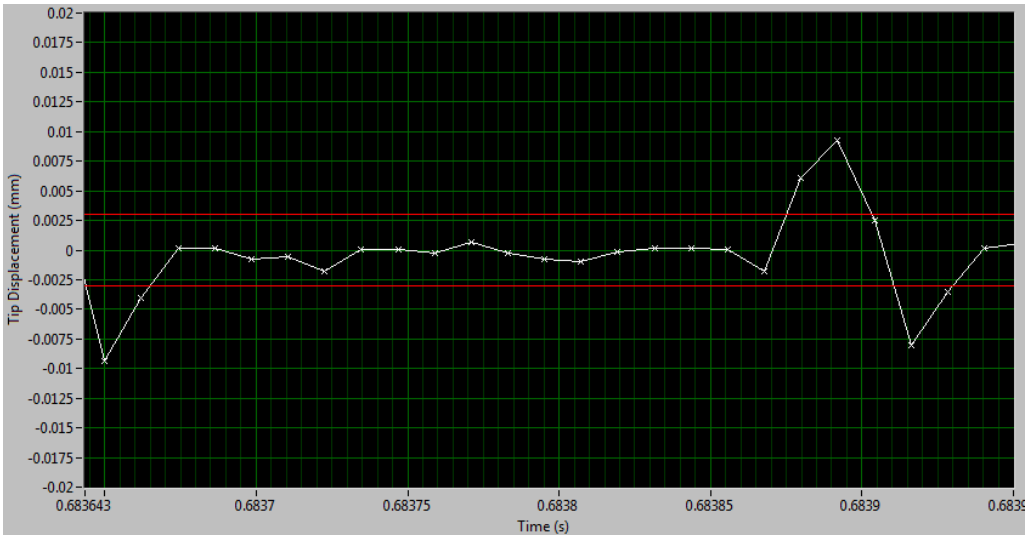

Figure 58: A typical graph of tip displacement of a single cycle at a data collection rate of 82500 Hz.

The representative data sets show that the profile and amplitude of the tip displacement are not greatly affected, despite capturing 10 data points per cycle. This indicates that the data collected throughout the experiment is not aliased.

EXPERIMENTAL RESULTS AND DISCUSSION

Cyclical Actuation Testing

The cyclical nature of the experiment perform is susceptible to random failures. The failure of material systems such as the MFC is often described by mapping the rate of failures into three regions. This mapping is called the bathtub curve due the shape the three regions form; this is shown in Figure 59. The dashed lines in Figure 59 represent the contribution of each region. The flat dashed line represents the baseline failure rate. The dark line is the superposition of the contributions from each section. The first region is often called infant mortality because it is comprised of early failures. This region is strongly driven by material defects or poor quality of manufacturing. The second region consists of random failures, sometimes caused by environmental effects. This failure rate is typically consistent with the baseline failure rate. The third section failures are referred to as wear-out failures caused by degradation factors. This region is usually comprised of failures caused by material break-down or crack propagation (Nuffer et al., 2007). The dependent axis indicates the rate of samples expected to fall in each of these regions. However, with the population size of this study being relatively small, it is difficult to get a clear picture of this effect based on statistics alone. Thus, performance of the unimorph was also tracked over time to understand the system better.

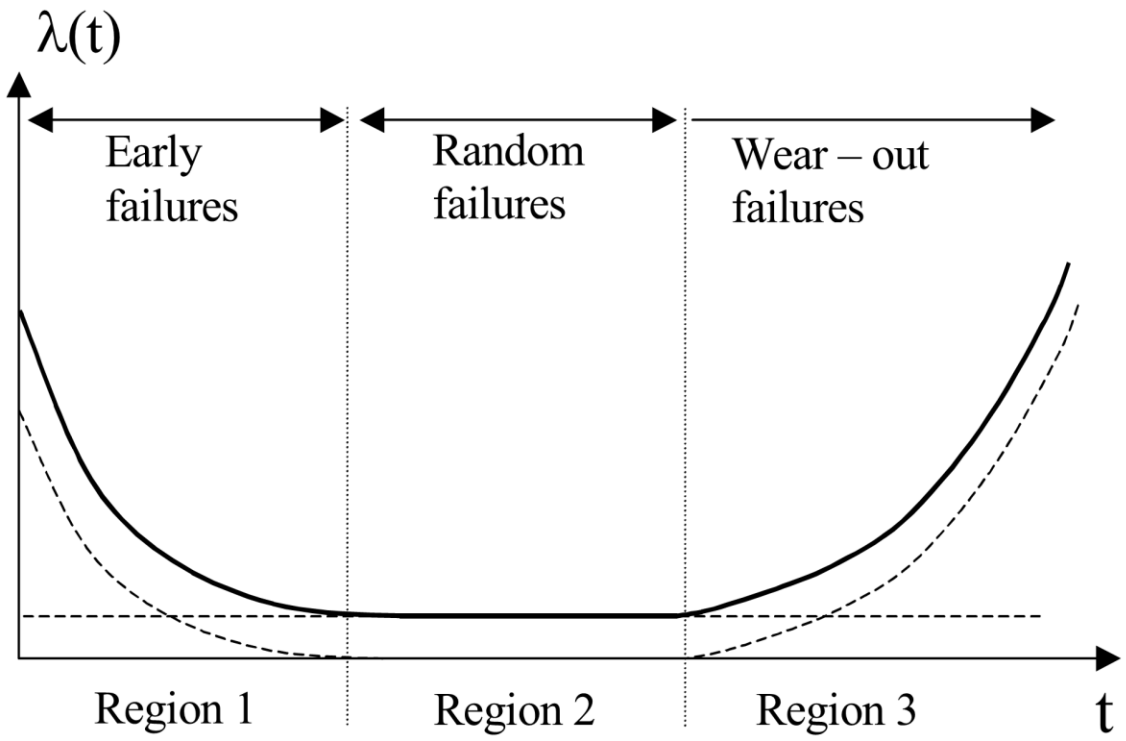

Figure 59: A typical bathtub curve represents failure rates over time. Failure rate, λ(t), is the dependent axis. (Nuffer et al., 2007)

After cycling the unimorph specimens, a correlation was noted between the beam geometry and usable life. Figure 60 shows the life of all unimorph samples tested. Tests in which samples surpassed 10^9 cycles were stopped, and are indicated in Figure 60 as non-failed specimens. The exception here is the 0.794mm (1/32”) #1, that sample failed before the test could be stopped.

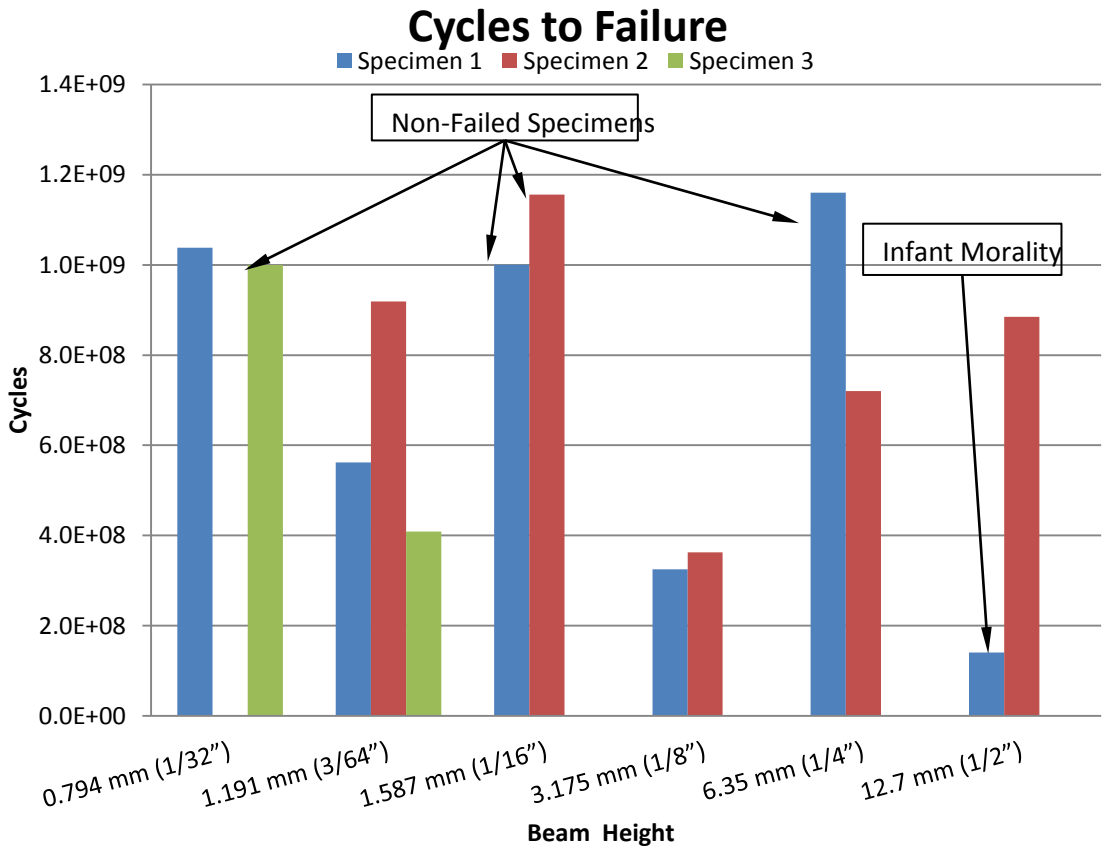

Figure 60: Cycles to failure for all tested beams.

Sample 1 of the 12.7mm (1/2") beam height series, indicated in Figure 60, showed a strong probability of infant mortality based on the micrograph shown in Figure 61. This micrograph was taken before the unimorph was cycled. Figure 62 shows the resulting failure that occurred after less than $2*10^8$ cycles. Defects of this nature were not commonly observed in this study; however, this type of flaw indicates that failure can be fiber driven.

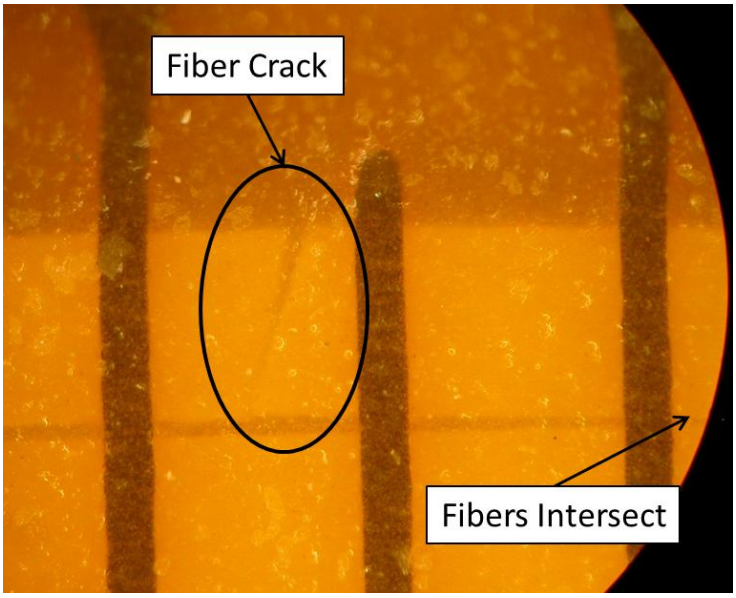

Figure 61: 12.7mm (1/2”) Sample #1. A micrograph of a crack on the fiber before cyclical testing took place.

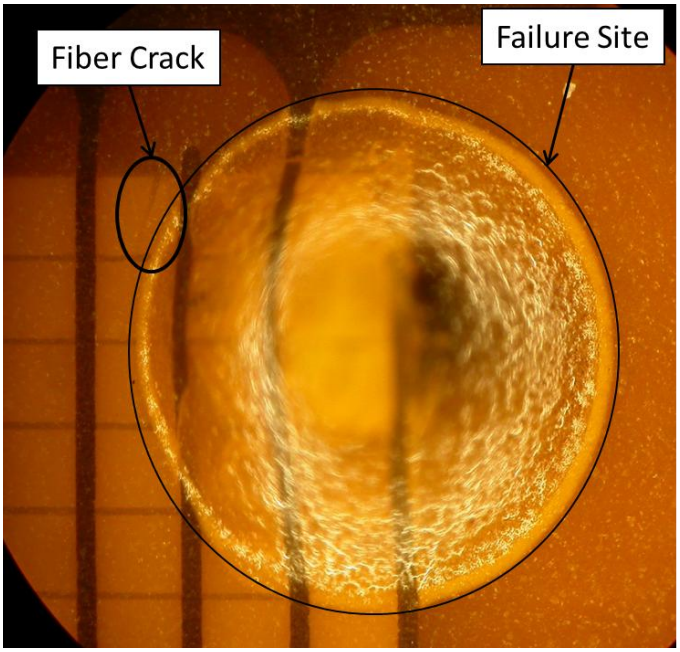

Figure 62: 12.7mm (1/2”) Sample #1. This is a micrograph of the failure site influenced by the fiber crack. This is a prime example of infant mortality.

The stand out information from Figure 60 is not the infant mortality, but rather the drop off in life in the 3.175mm (1/8”) samples. The life of the MFC unimorph was shown to be strongly linked to the increase in work energy of the MFC-beam as the beam and MFC approached similar stiffness, as shown in Figure 37 above.

To generate a baseline expectation of the unimorph performance, a static experiment was conducted on the four available samples. The four empirical displacements of the samples are shown in Figure 63 and Table 5. The analytical theory developed by Marc Weinberg (Weinberg, 1999) was programmed in MatLab using the MFC and substrate material properties and geometries. The Weinberg approximation results match up acceptably with the empirical test data.

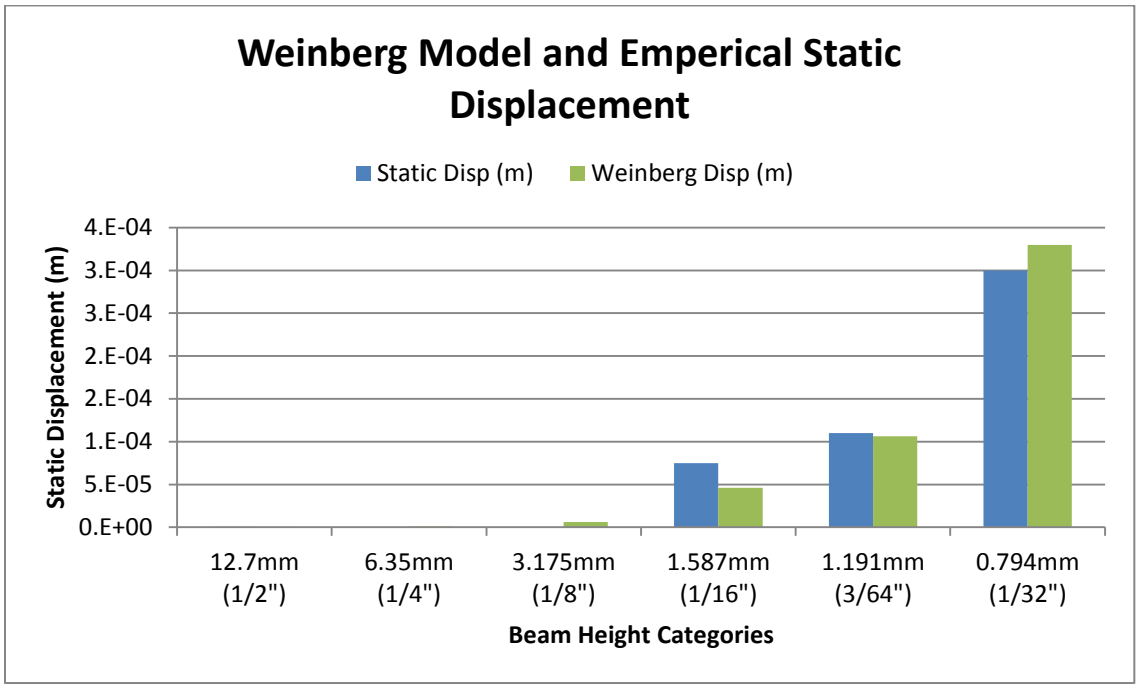

Figure 63: Comparison of empirical static displacement of the unimorph versus the Weinberg analytical unimorph model displacement.

Table 5: Table of Static Displacement, Weinberg Model Displacement, and percent error between the two.

Beam Height	12.7mm (1/2")	6.35mm (1/4")	3.175mm (1/8")	1.587mm (1/16")	1.191mm (3/64")	0.794mm (1/32")
Static δ (m)	1.00E-07	-	-	7.50E-05	1.10E-04	3.00E-04
Weinberg δ (m)	0.000000099	0.000000784	0.000006118	0.000046127	0.000106139	0.000329745
Percent Error	-0.78	100.00	100.00	-62.59	-3.64	9.02

The performance variable tracked in this experiment was deflection of the cantilevered beam. The beam, test fixture, and laser displacement sensor were configured such that the laser measured deflection at 111.5 mm from the clamped end of the beam. The LabVIEW VI collected windows of 180 data points every 60 seconds. The 180 data points were collected at a rate of 45000 samples per second, or 0.0000222 seconds per sample. For a driving frequency of 3750, this results in 12 samples collected per cycle. This sampling was held constant through the entire test. The first step of post processing the data was to take the raw displacement data and correct for zero-offset drift. This was necessary due to the sensitive nature of the laser and the inadequacy of the laser fixture. As shown in Figure 57, the beam returned to a stable condition between pulses. This was taken by LabVIEW as the zero point of each cycle. Then the VI would take the corrected displacement and find the peak value of each cycle. At this point, the data was still significantly large. The amplitude of the peaks were then averaged into half hours. Thus, peak data points were generated for every half hour of the test, and each point of data is described by the average of approximately 360 points. The peak displacement data is shown in Figure 64, along with the static displacements

as determined above by the Weinberg analytical method for unimorph beams. This process gave a cleaner picture of the peak values over time, but it is clear that there was still a lot of scatter in the peak displacement values over time. It is also evident from Figure 64 that there is a break in period that lasted less than 20 hours, or about 250 million cycles for the unimorph system, specifically, the damage to the piezoelectric fibers a result of crack propagation.

Unfortunately, Figure 64 also shows that dissipation factors are in effect in the MFC when cycled at the rate used during this experiment. This is primarily evidenced by the difference between the empirical results of static displacement and cyclical displacement at 3750 Hz. The Weinberg displacement, due to its static nature, neglects viscous damping effects, which would further compound the difference.

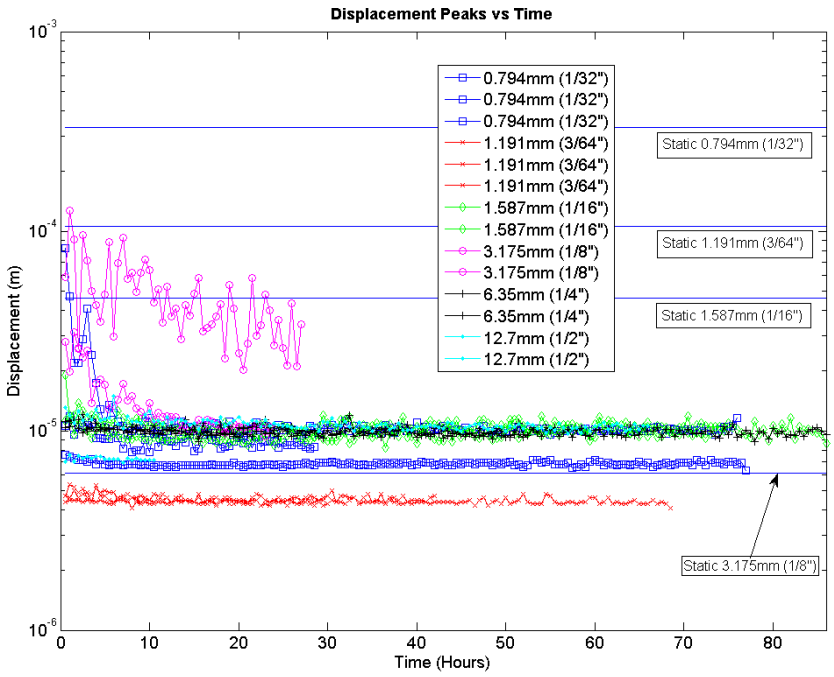

Figure 64: 30 Minute averages of peak displacement data.

It is interesting to note that the displacement recorded by the laser shows convergence of several of the beams to the same displacement. Near 10^{-5} m, there are deflections from several beam geometries that converge. To get a better understand of what the effect of the substrate has on the system, the area moment of inertia in the bending direction, $I_{beam,}$ and the elastic modulus, E_{beam}, were multiplied with the peak displacements shown in Figure 64. This dataset is shown in Figure 65. In this figure, the only variable that changes between the sample sets is beam height, the data trends predictably with change in height.

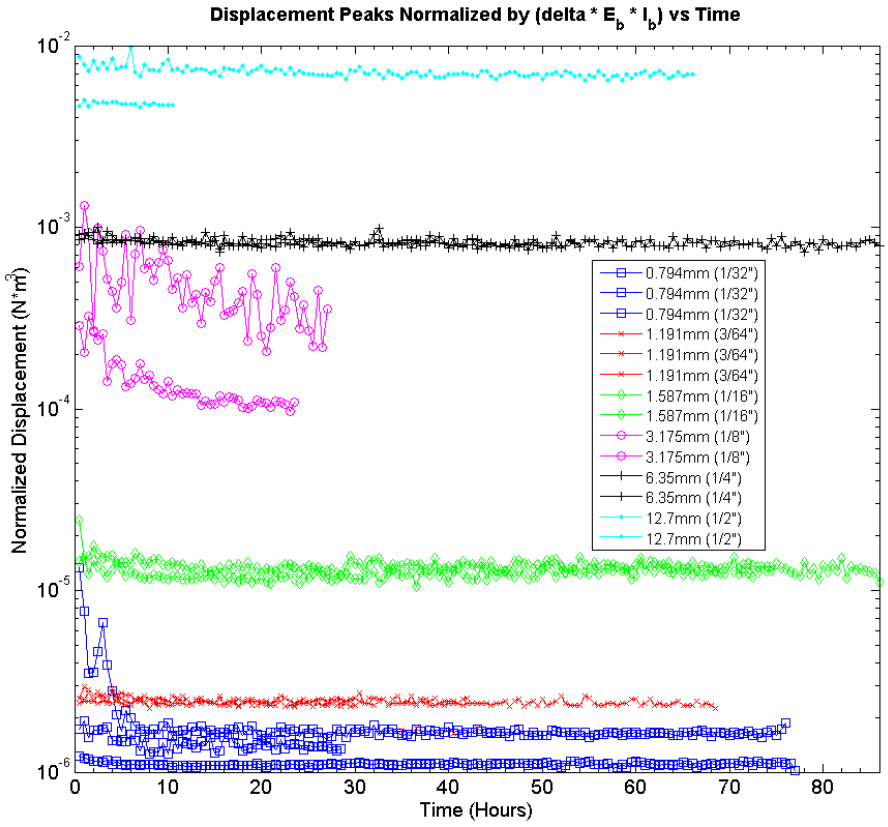

Figure 65: Peak Displacement normalized by Area Moment of Inertia and Elastic Modulus of the beam.

If the displacement data were more reliable, back calculation of the real performance of the MFC would be useful. If the first cycle displacement is considered the maximum expected deflection, decreases in the deflection over time could be back calculated as changes in the effective d_{33} or the effective stiffness of the piezocomposite, or some additional derived damage factor. What can be considered is the decrease in performance that was recorded, as shown in Figure 66, plotted on a linear scale. What can be said about the MFC is that the performance of under dynamic loading does not change substantially once the break-in occurs, despite an immense amount of crack propagation in the piezoceramic fibers.

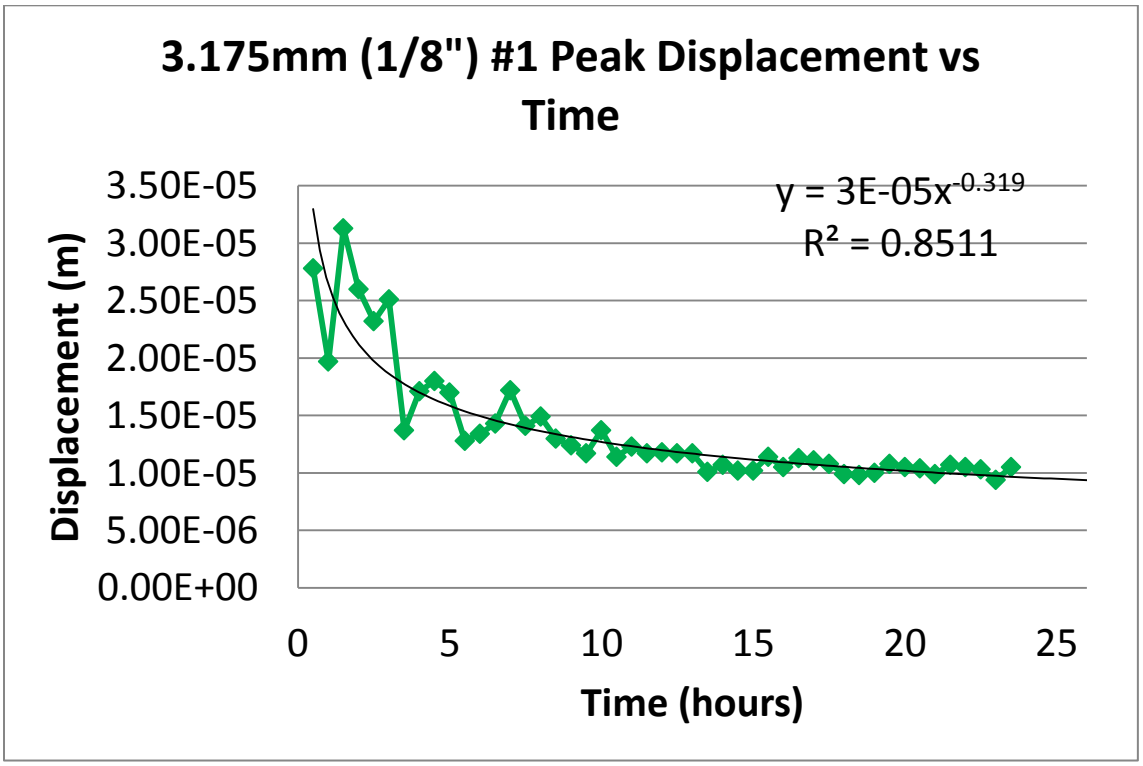

Figure 66: Beam 3.175mm plotted on a linear scale, with a power curve fit to the data.

It was also expected that an increase in cracks in the piezoceramic fibers would decrease the stiffness of the piezocomposite and therefore change performance based on the increase in the ratio of beam stiffness to piezo stiffness. This did not appear to alter the performance significantly past the break-in.

System Failure via Electrical Shorting

Both this study and Henslee's study have established that the primary method of failure in MFC systems is due to a decrease in the dielectric of the composite between the interdigitated electrodes such that the system no longer operates electrostatically, but as an electrical short. Figure 67 shows a longitudinal cross-section of an uncycled MFC, the intact epoxy can be seen between the electrodes.

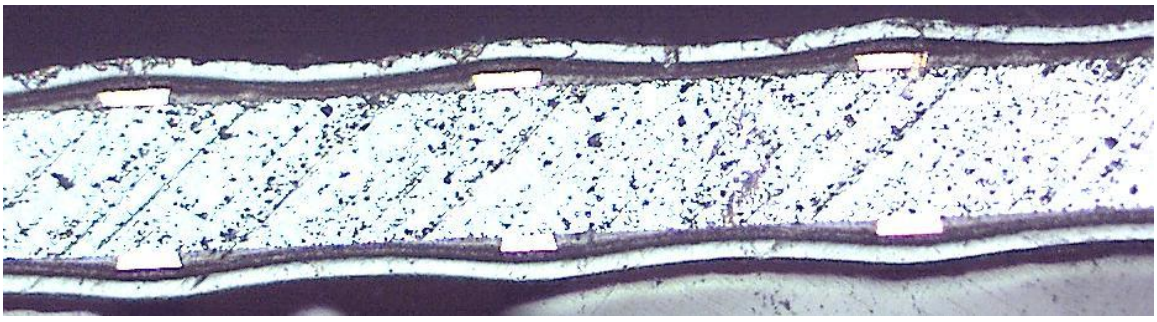

Figure 67: Longitudinal cross-section of an uncycled MFC.

Physically, the failure of the material system manifests itself as electrical arcing between an air gap. This is a result of cyclical actuation leading to the destruction of the epoxy as an insulator. As damage accumulates in the fibers, cracks grow, as shown in Figure 68. What is unknown is whether the arcing manifests through the crack paths or

if the layer of epoxy on top of the fiber and between the electrodes experiences a delamination, thus generating a direct line between the electrodes.

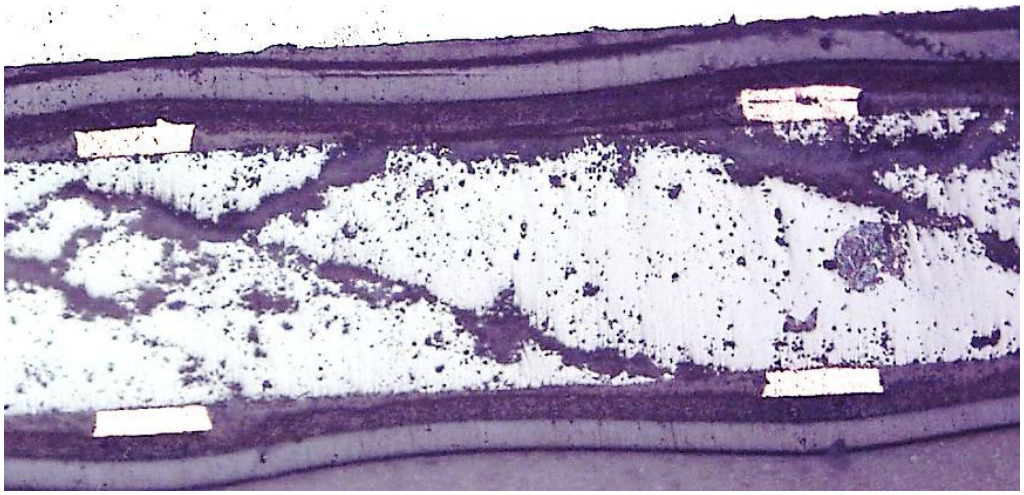

Figure 68: A heavily cycled MFC with crack propagation.

Using the breakdown field of standard air and the structural epoxy as 3E+6 V/m and 25E+6 V/m, respectively, and an airgap distance based on the pitch of the electrodes, the minimum voltage required to induce electrical arcing is given as,

$$V_{breakdown} = E_{breakdown} * \delta_{gap} \quad [38]$$

Resulting in a breakdown voltage through the epoxy of 12.5kV and 1.5kV through air. Assuming the direct pathway between the electrodes is the main pathway, this indicates that the epoxy must fail completely as an insulator to induce arcing.

Figure 69 shows a graph from the front panel of the LavVIEW data logging VI. In this VI, the graphs on the front panel are heavily aliased due to their low priority, which is why the current appears as it does, but at the point of failure the current spike is

clearly visible. The LabVIEW data logging VI was written to watch for this current spike and then initiate a shutdown sequence.

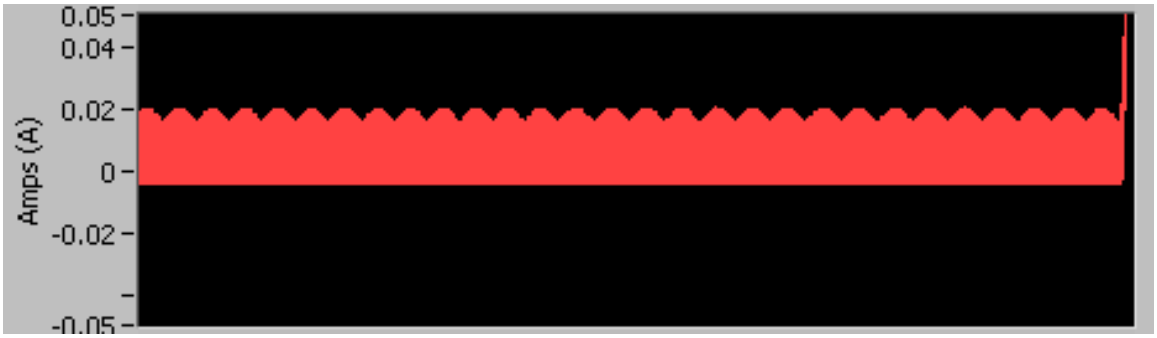

Figure 69: Amplitude chart taken directly from the front panel of LabVIEW at the point of failure.

Microscopic Imaging of Specimens

It was observed that the MFC's that were highly cycled were darker than they originally were. Upon closer visual inspection, it was evident that there were small cracks in the piezocomposite structure. The Nikon microscope system described above was used to examine the cracks. The images showed that on all of the MFC's there was some level of crack propagation present. By using the focal plane of the microscope, it was deduced that the cracks were occurring in the brittle ceramic fibers of the MFC. It was also noted that the size and number of cracks present in the MFC's trended positively with increased cycle count. Furthermore, the cracks are shown to emanate from the direction of the positive electrodes only, as shown in Figure 70. This

phenomenon was consistent in all samples, and is primarily linked to the number of cycles.

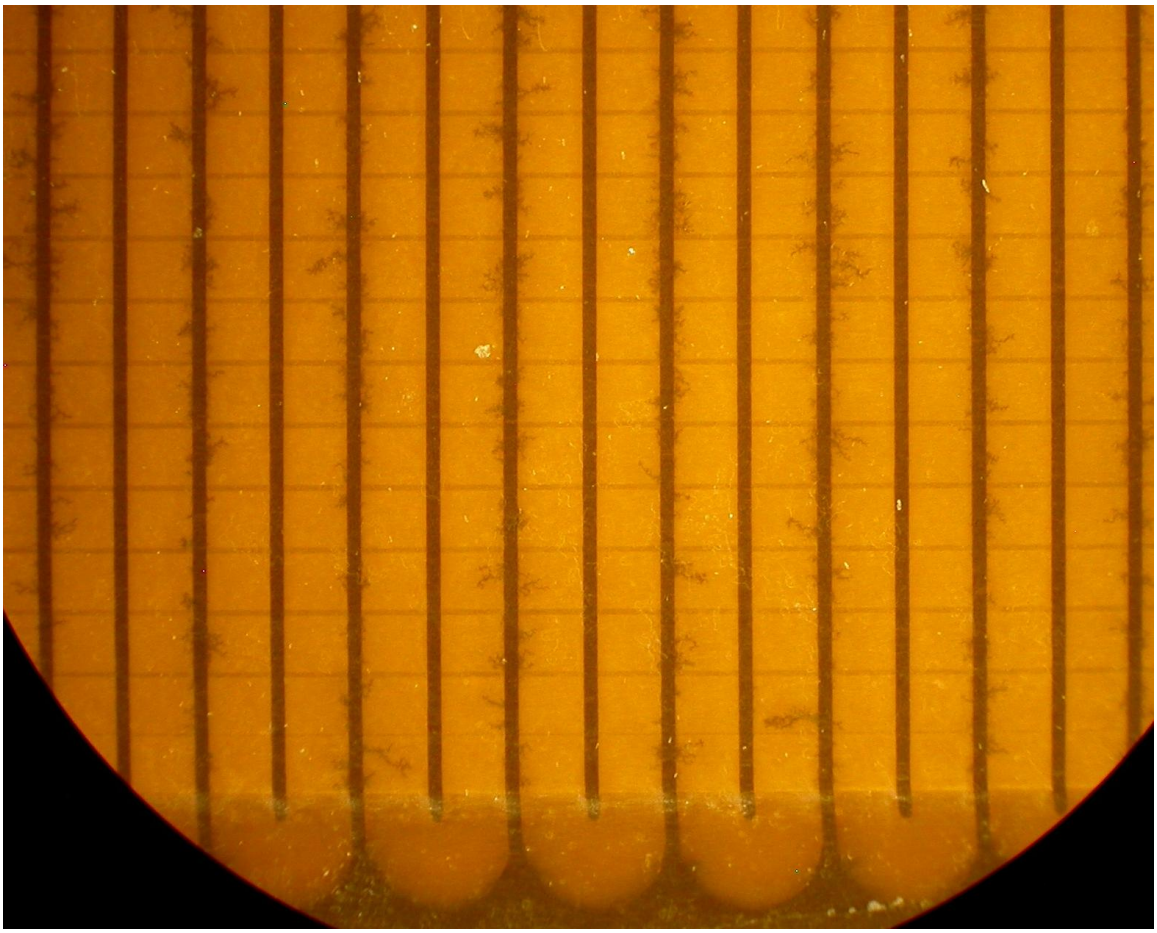

Figure 70: Unimorph 0.794 mm (1/32") #1 lasted more than 10^9 cycles. The cracking visible in the piezoceramic is significant.

A possible reason for this is based in the way that the MFC's are poled and operated, as demonstrated above in Figure 35. Consider again that when the structure actuates, there are both active and inactive areas, or dead zones. This will induce a strain gradient in the material. Empirically, it has been shown for an MFC operating in a

unipolar voltage range, the volumes of material near the positive and negative electrodes the fibers are in tension and compression a, respectively. Despite being encased in structural epoxy, the brittle ceramic is still subject to brittle fracture and crack propagation. Ceramic materials typically have a far superior compressive strength than tensile strength. PZT-5A, the type of piezoceramic used in this MFC is no different. As shown in Table 6, the compressive strength of the piezoceramic is more than an order of magnitude greater than the dynamic tensile strength. Considering the high degree on unidirectionality, it is safe to assume the 3 direction is the first principal axis and that any significant loads will be in this direction only. Since the only significant loads are in the 3 direction, the Maximum-Normal-Stress Theory reduces to one axis. Without reliable displacement data it is overly difficult to back-calculate the mechanical stress and strain in the piezocomposite, but it is safe to assume that if cracks were able to propagate in a tension region, that the dynamic tensile strength was exceeded.

Table 6: Ultimate strengths for PZT-5A from Morgan Electro Ceramics (Berlincourt & Krueger, 2003).

Compressive and Tensile Strengths of PZT-5A (Berlincourt & Krueger, 2003)		
Compressive Strength	>75000 PSI	>517 MPa
Tensile Strength (Static)	11000 PSI	75.8 MPa
Tensile Strength (Dynamic)	3500 PSI	24.1 MPa

The data logging program used to run the test equipment and record displacement used the jump in current to stop the piezo if a failure occurred. This method was effective at stopping the test. Figure 71 and Figure 72 show two examples

of failure sites. Figure 72 has the appearance of a layer delamination, while Figure 71 shows what happens to the copper-clad Kapton layer if electrical arcing occurred between two interdigitated electrodes. After additional examination of the micrographs, it can be concluded that the failures that appear to be delaminations from the visible surface, such as that in Figure 72, are likely caused by the same catastrophic arcing failures on the non-visible side of the fiber-electrode layer.

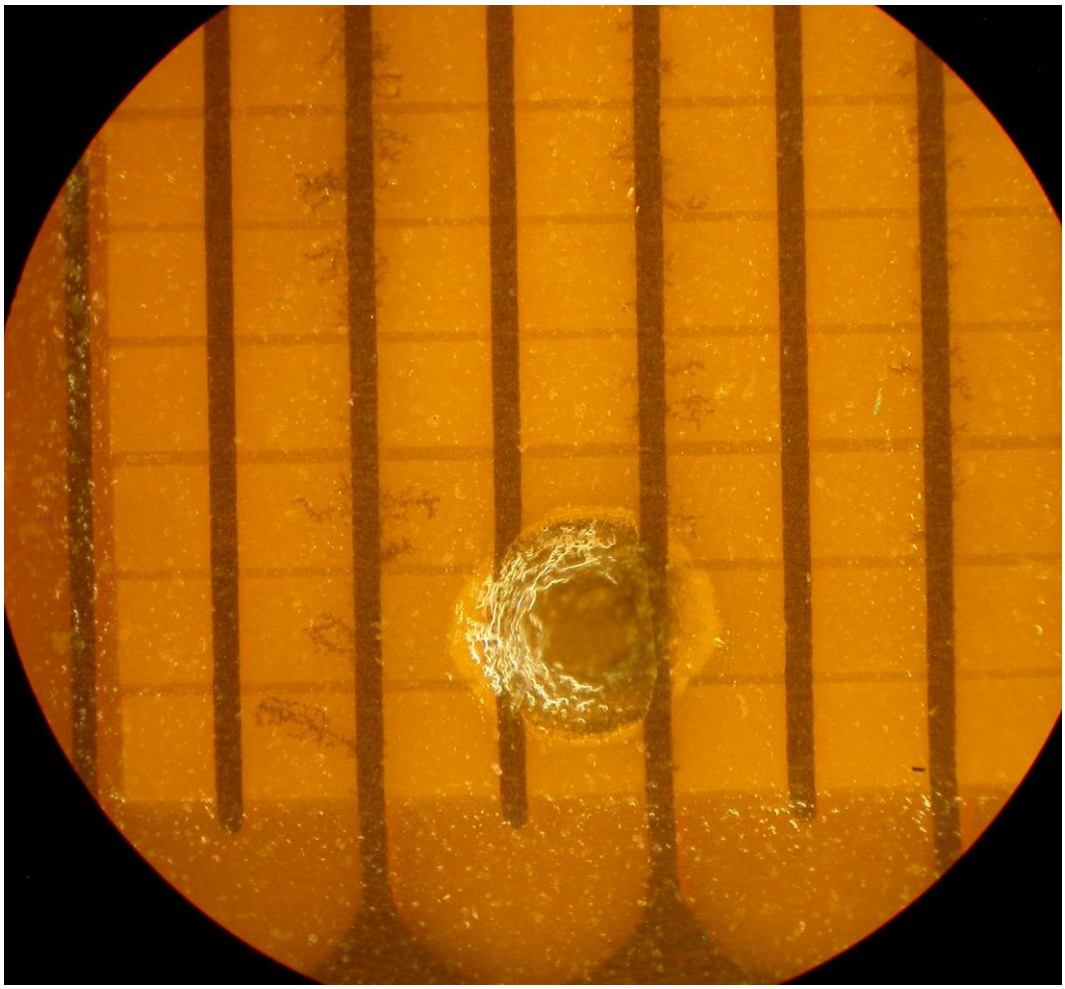

Figure 71: Failure site on unimorph 1.191mm (3/64") #1. This beam lasted more than 550E+6 cycles, and showed some evidence of crack propagation.

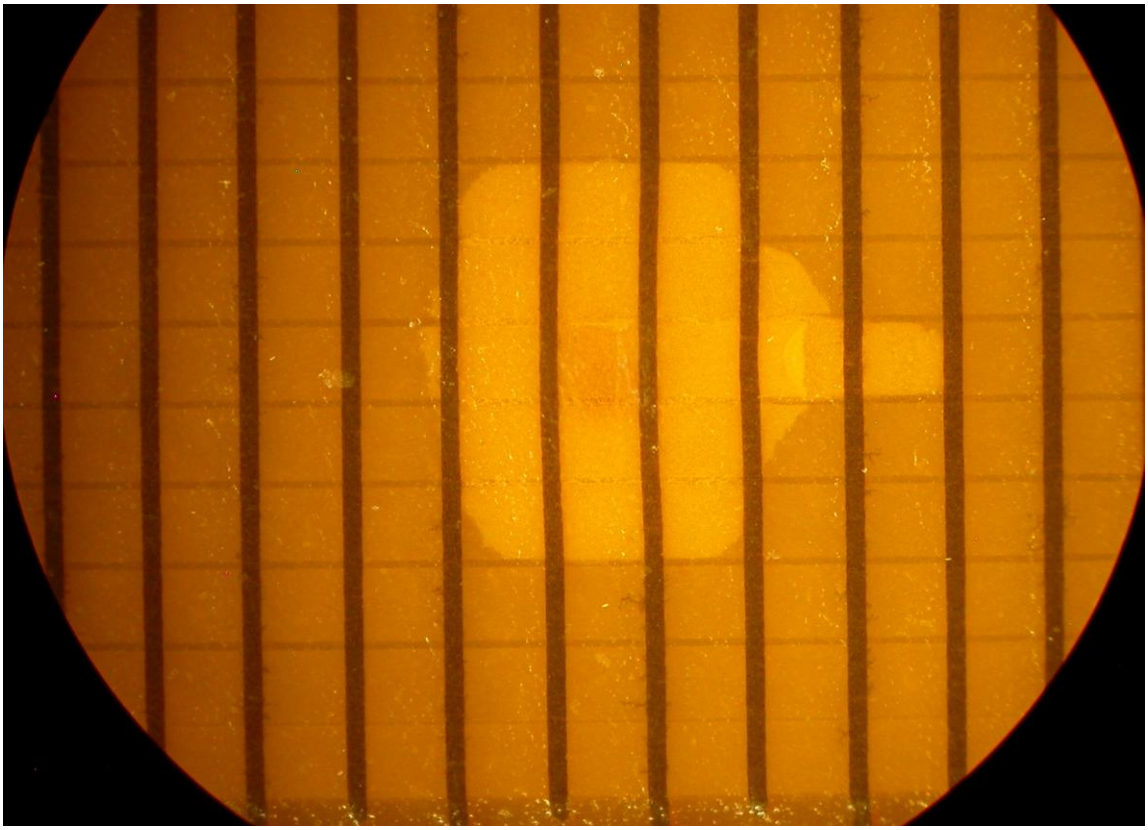

Figure 72: Failure site on beam 1.191mm (3/64") #3. There is less evidence of cracking in this beam, which had approximately 400E+6 cycles.

Damage Tolerant Design

There is significant evidence that the MFC is a very damage tolerant design. It is unknown exactly what factors lead the MFC designers to choose PZT-5A as piezoceramic fibers or Loctite DURABOND E-120H as the structural epoxy, but some of the factors that would have lead them to these primary components can be gleaned.

It is critical that the epoxy have the right stiffness such that it is capable of transferring the load from the piezoceramic fibers to the substrate. If the epoxy is too soft or too hard or it will absorb too much of the energy or constrain the piezoelectric

fibers too much, respectively. The epoxy also needs to support the fibers mechanically, as in a fiber reinforced composite system. In a typical fiber composite, the fibers are substantially smaller and there are more than in the MFC. This means that the failure of a single fiber is less critical, this idea does not carry over well to a composite structure with active fibers. It has been shown through this research that cracked piezoceramic fibers will still experience bulk deformation in the presence of an electrical field, and the structural epoxy is still capable of transferring the load in a way that does not lead to a significant decrease in performance. This is likely due to the virtual discretization of the piezoelectric fibers, by the interdigitated electrodes, into small regions with individual performance. Furthermore, it appears that as long as the structural epoxy is capable of maintaining the dielectric between the electrodes with significant cracks present, the MFC will continue to operate.

The piezoceramic used in the specific MFC's used in this research is PZT-5A is also known as Navy Type II and typically classified as a "soft" piezoceramic. This choice was likely made on the desire for the MFC package to be highly conformable, but also for better damage tolerance with respect to strain while generating loads.

Improving Design

The overall MFC packaging has many benefits as an actuator or sensor with respect to performance, very thin package envelope, and damage tolerance. However, the failure of the device is a direct result of using interdigitated electrodes. This would

be a dilemma, but without the IDE's, the MFC would lose many of its most important benefits, such as unidirectionality and utilization of the high d_{33} piezoelectric constant. Possible areas of improvement in the MFC system include changes in the electrode pitch and pattern, as well as changes to the dimensions of the piezoceramic fibers.

Future Work

This research indicates that gaps exist in the knowledge base about the operation of MFC's that need to be filled. A critical gap is the understanding of frequency response. The majority of piezoelectric theory is written for static systems. Theory exists for dynamic systems, but the material properties are not as well defined for MFC's. It would also be very beneficial to characterize life at and around resonance frequencies. Without knowing the impact of frequency response on the life and performance of MFC systems, choosing substrate geometry for the purposes of this study or for practical applications is made more difficult.

It would also be pertinent to evaluate and model the break-in phase of the MFC. A drop-off of more than 60% from peak performance to failure was noted for the 3.175 mm #1 sample. A rudimentary power curve was fit to the performance data of this sample, as shown in Figure 66. This work should lead to a numerical damage model, which would potentially be based on the crack growth with respect to cycles.

WORKS CITED

Berlincourt, D., & Krueger, H.H.A. (2003). Technical Publication TP-226: Properties of Morgan Electro Ceramic Ceramics.

Bryant, Robert G. (2008). *Overview OF NASA Langley'S Piezoelectric Ceramic Packaging Technology And Applications*. NASA Langley Research Center. Hampton, VA 23681. Retrieved from http://ntrs.nasa.gov/archive/nasa/casi.ntrs.nasa.gov/20080000875_2007039089.pdf

Henslee, Isaac Andrew. (2010). *Macrofiber piezoelectric composite for lunar exploration actuator* (pp. xv, 103 leaves). Retrieved from http://etd.lib.montana.edu/etd/2010/henslee/HensleeI0810.pdf

Inman, Daniel J., & Cudney, Harley H. (2000). *Structural and Machine Design Using Piezoceramic Mateials*. Center for Intelligent Materials Systems and Structures. Virginia Polytechnic Institute. Blacksburg, VA 24061.

Instruments, National. (2004). Aliasing - LabWindows/CVI 8.1 Help. from http://zone.ni.com/reference/en-XX/help/370051H-01/cvi/aliasing/

Leo, Donald J. (2007). *Engineering Analysis of Smart Material Systems*. Hoboken, New Jersey: John Wiley & Sons, Inc.

Nuffer, J., Schönecker, B, Kohlrautz, D., Michelis, P., Adaragga, O., & Wolf, K. (2007). *Reliability Investigation of piezoelectric Macro Fibre Composite (MFC) Actuators*. Paper presented at the Adaptronic Congress, Göttingen, Germany.

Rao, Singiresu. (2011). *Mechanical Vibrations* (5th ed.): Pearson Education, Inc., publishing as Prentice Hall.

Smart-Material, Corporation. (2011). Piezo Fibers & Tubes (pp. 1). Sarasota, FL: Smart Material Corporation.

Trek, Inc. (2011). Operator's Manual Model PZD700A. Medina, NY 14103: Trek, Inc.

Weinberg, Marc S. (1999). Working Equations for Piezoelectric Actuators and Sensors. *Journal of Microelectromechanical Systems, 8*(4), 5.

Wilkie, W., High, J., & Bockman, J. (2002). *Reliability Testing of NASA Piezocomposite Actuators*. Paper presented at the 8th International Conference on New Actuators, Bremen, Germany. http://ntrs.larc.nasa.gov/search.jsp?R=20030014135&qs=Ns%3DLoaded-Date%7C0%26N%3D4294650593%26Nn%3D4294929456%257CSubject%2BTerms%257CCOAL

Wilkie, W. Keats, Bryant, Robert G., High, James W., Fox, Robert L., Hellbaum, Richard F., Jalink, Antony, . . . Mirick, Paul H. (2000). *Low-Cost Piezocomposite Actuator for Structural Control Applications*. Paper presented at the International Symposium on Smart Structures and Materials, Newport Beach, CA.